# Controlling Excitable Media With Noise

DISSERTATION

zur Erlangung des akademischen Grades
doctor rerum naturalium
(Dr. rer. nat.)
im Fach Physik

eingereicht an der
Mathematisch-Naturwissenschaftlichen Fakultät I
Humboldt-Universität zu Berlin

von
Herrn Franz-Xaver Sailer, M.A.
geboren am 09.09.1976 in Lich

Präsident der Humboldt-Universität zu Berlin:
Prof. Dr. Chritoph Markschies

Dekan der Mathematisch-Naturwissenschaftlichen Fakultät I:
Prof. Thomas Buckhout, PhD

Gutachter:

1. Prof. Dr. Lutz Schimansky-Geier
2. Prof. Dr. Harald Engel
3. Prof. Ryoichi Kawai, PhD

| | |
|---|---|
| eingereicht am: | 10. Januar 2006 |
| Tag der mündlichen Prüfung: | 31. März 2006 |

**Abstract**

The focus of this study is on the influence of fluctuations on coupled excitable systems.

For that purpose we first examine numerically the stationary probability distribution as well as the probability flux for an individual FitzHugh–Nagumo system with additive noise. Depending on noise intensity and separation of the timescales different combinations of extrema are found which can be used to classify parameter sets. In one of these sets we find reminiscences of coherence resonance in the distribution.

For the investigation of coupled ensembles of excitable systems we use a method based on the central moment dynamics of the corresponding probability distribution. We derive a general expression for a system with $N$ variables per ensemble unit and discuss the quality of different approximation techniques.

Noise can not only influence existing excitable dynamics but it can also alter dynamics that are formerly not excitable in such a way that they become excitable. We demonstrate this using a generalization of a well known model for noise-induced phase transitions under the influence of multiplicative noise. With the help of the moment dynamics we obtain the system's phase diagram that shows regions of noise induced oscillations of the ensemble mean and noise-induced excitability of the mean. Between these two regimes there exists a complicated transition regime.

When applying uncorrelated additive noise to each unit of a globally coupled ensemble with FitzHugh–Nagumo kinetics a strikingly similar transition of the mean is observed. We study this transition in detail using the moment dynamics method. Besides period-two oscillations, chaos, intermittent spiking and other regimes we find in the course of the transition a quick increase of a chaotic attractor. This phenomenon is known from non-chaotic oscillations as Canard explosion.

We then apply additional global fluctuations to the system but leave the sum of the global and local noise intensities constant. With increasing correlations of the fluctuations the mean of the ensemble exhibits a phenomenon resembling coherence resonance. The coefficient of variation shows a minimum not for a finite nonzero value of the overall noise intensity but of the noise intensity of the global component.

We demonstrate the possibility of pattern formation with the help of dichotomous fluctuations using an array of excitable units with nearest neighbor coupling locally obeying FitzHugh–Nagumo kinetics. Depending on the spatial and temporal correlation of the dichotomous fluctuations we find different mechanisms and different parameter ranges for the creation of structure patterns.

**Keywords:**
Excitability, Noise, Moment Dynamics, Pattern Formation

**Zusammenfassung**

Im Fokus dieser Untersuchung steht der Einfluß von Fluktuationen auf gekoppelte erregbare Systeme.

Dazu betrachten wir zunächst numerisch die stationäre Wahrscheinlichkeitsverteilung und den Wahrscheinlichkeitsfluß für ein einzelnes FitzHugh–Nagumo System mit additivem Rauschen. Abhängig von der Rauschintensität und der Separation der Zeitskalen treten unterschiedliche Kombinationen von Extrema in der Wahrscheinlichkeitsverteilung auf. Diese Kombinationen können zur Klassifizierung unterschiedlicher Parametersätze verwand werden. In einem dieser Sätze finden wir in der Verteilung Reminiszenzen an Kohärente Resonanz.

Zur Untersuchung von gekoppelten Ensembles erregbarer Systeme nutzen wir eine Methode die auf der Dynamik der zentralen Momente der zugehörigen Verteilungen basiert. Wir leiten einen allgemeinen Ausdruck für ein System mit $N$ Variablen her und diskutieren die Qualität verschiedener Näherungsmethoden.

Rauschen kann nicht nur bestehende erregbare Dynamiken beeinflussen, es kann auch die Dynamik eines ursprünglich nicht erregbaren Systems derart verändern, daß dieses Erregbarkeit zeigt. Dies demonstrieren wir durch Verallgemeinerung eines bekannten Modells für rauschinduzierte Phasenübergänge, das multiplikativem Rauschen unterworfen ist. Mit Hilfe der Momentenmethode erhalten wir das Bifurkationsdiagramm. Es zeigt Regionen rauschinduzierter Oszillationen und auch rauschinduzierter Erregbarkeit des Mittelwerts des Ensembles. Zwischen diesen beiden Regionen liegt ein kompliziertes Übergangsregime.

Wenn wir unkorreliertes additives Rauschen auf jede Einheit eines global gekoppelten Ensembles mit FitzHugh–Nagumo Kinetik anwenden, beobachten wir einen auffallend ähnliches Übergangsregime hin zu Oszillationen des Mittelwerts. Wir untersuchen diesen Übergang im Detail mit Hilfe der Momentenmethode. Neben Periodenverdopplung, Chaos, unterbrochenem Spiking und anderen Dynamiken finden wir im Rahmen dieses Übergangs ein plötzliches starkes Ansteigen der Ausdehnung eines chaotischen Attraktors. Dieses Phenomän ist bei nichtchaotischen Oscillationen als Canard Explosion bekannt.

Zur Untersuchung des Einflusses von Korrelationen auf das System führen wir zusätzlich einen globalen Rauschterm ein. Dabei wird die Summe der globalen und der lokalen Rauschintensität konstant gehalten. Mit steigenden Korrelationen beobachten wir ein Verhalten ähnlich der Kohärenten Resonanz. Der Variationskoeffizient zeigt ein Minimum für eine endliche Intensität der globalen Komponente des Rauschens.

Wir demonstrieren die Möglichkeit von Musterformation mit Hilfe von dichotomen Fluktuationen an Hand eines Feldes von erregbaren Einheiten, die durch

Nächste-Nachbar-Wechselwirkung gekoppelt sind und lokal der FitzHugh–Nagumo Kinetik gehorchen. Abhängig von räumlichen und zeitlichen Korrelationen tritt die Formation von Structure Patterns durch unterschiedliche Mechanismen und in unterschiedlichen Parameter Regionen auf.

**Schlagwörter:**
Erregbarkeit, Rauschen, Momenten Dynamik, Musterbildung

# Contents

# Chapter 1

# Introduction

The description of a real world system is a formidable task. Let us make a gedankenexperiment: We want to measure the intensity of the light of a certain wavelength coming from the sun. The precise results of our measurement will depend on many factors: the temperature of sun's surface, the distance between sun and earth, the weather on earth, to name but a few. Let us exemplarily pick out the weather. It's behavior is determined by chaotic dynamics. Every physics undergraduate knows the famous butterfly effect. How can we take into account all these complex atmospheric changes? The answer is simple: We cannot. Certainly not with our today computer power and storage capabilities and more importantly not with our scientific understanding. It is the physicists task to find elementary principles in and to extract the key properties out of natural systems. The understanding of nature and the prediction of the behavior of real world systems depend thereon.

It is not only the overwhelming complexity of real world systems that renders the exact prediction of their behavior impossible. While Einstein was convinced of "Gott würfelt nicht" todays quantum physicists state that any observation we do is inherently afflicted with randomness.

The typical procedure to cope with our desire for simplification and the incapability to give an exact complete description of nature is either to imply random fluctuations to the idealized deterministic descriptions we develop of nature or to neglect the fluctuations and to go with the deterministic (average) behavior, only. While the latter method works well in many cases physicists have demonstrated the importance of fluctuations for a long time [31, 68, 113].

One reason that down to the present day makes scientists neglect fluctuations is the erroneous assumption that they have nothing but a blurring effect. Many studies have proved this assumption wrong [55, 73, 121]. It was shown that the quantitative measures of the fluctuations become additional control parameters of the system and can thus enrich the dynamics of a system.

Especially the interplay of noise and nonlinear systems is in the focus of many investigations [83]. Advances in computer power support recent studies and have helped to expand investigations to extended systems [38]. One large group of systems that exhibit nonlinear dynamics are excitable systems. Their behavior under the action of noise has been subject of many studies [71].

Since it is the center of the present work we give an introduction to excitability in sec. 1.1. It is followed by a short overview over a typical and important example of a real world system exhibiting excitability namely the neuron. The model that was most frequently used in the present work and that has become an archetype model for excitability was derived in the context of neuron dynamics. In the final section of this chapter (1.3) we give an overview over this thesis.

## 1.1 Excitability

The concept of excitability can be found in a variety of different fields of science [13, 41, 82, 107, 111, 115]. Systems that at the first glance seem to have nothing in common like jellyfish [82], special chemical reactions [4], wildfires [3], neurons [61], soccer fans [33], epidemics [123], lasers [127], cardiac tissue [90] and plankton bloom [133] share the property of excitability. The variety and diversity of the different applications shows the importance and at the same time the universality of the phenomenon.

An excitable system possesses a stable fixed point. Stability is only a local property of the fixed point, though. This means that *small* perturbations (or stimuli) decay. In contrast, perturbations exceeding a certain threshold do not decay but the excitable system responds with a large excursion in phase space until finally returning to the fixed point again. This is illustrated in fig. 1.1. The timeseries representation of such an excitation is called a spike (cf. fig. 3.2). The time between two consecutive spikes is called the *interspike interval*.

The time span from the perturbation until the system is in the vicinity of the fixed point again is called the refractory time. During this period the system is mainly insensitive to further perturbations, i.e. the effect of a new perturbation on the trajectory itself as well as on the refractory time is for most measurements negligible.

As soon as the system is in the vicinity of the fixed point it can once more be excited. Here, the term *vicinity* is not well defined. The time from which on the system can be re-excited depends e.g. on the magnitude of the perturbation. In this context one usually refers to the *relative refractory time*.

If many excitable systems (or different sites of a continuous field that locally obeys excitable dynamics) interact, new, collective phenomena arise. The probably best known such phenomenon is the development of spiral waves. Consider a

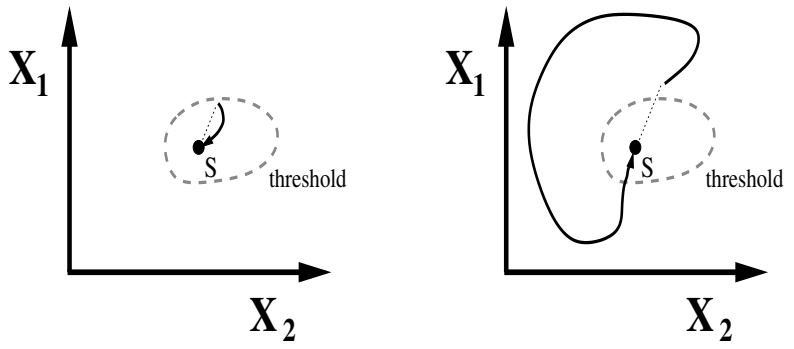


Figure 1.1: Response of a two variable ($x_1$, $x_2$) excitable system to sub- (left) and superthreshold (right) stimuli. The stable fixed point is labeled S. The perturbations are shown by the dotted lines, the trajectories of the system by the solid lines.

two dimensional extended array of excitable units that are each coupled to their neighbors. If a system is excited by some perturbation it can for proper coupling pull its neighbors above the excitation threshold. They can in turn excite their neighbors and a circular wave (called target pattern) of excitation moves through the extended system. After the excitation all systems return to their rest state . Due to inhomogeneities the wave can evolve into a rotating spiral instead of a circular structure. A typical example is shown in fig. 1.2. The spiral tip can either stand (rigid rotation) or move (meandering) [5, 14].

The figure shows a rotating spiral wave pattern in the light sensitive Belousov-Zhabotinsky (BZ) reaction. Due to its dynamical diversity and due to practical reasons like comparatively low implementation costs this chemical reaction has become the probably most popular experimental system to study excitability (although the dynamics are not restricted to excitability [80]). Under the correct circumstances the concentrations of the reactants form standing or moving patterns of various types [122].

The perturbations that lead to the excitation of excitable systems and with it to the initiation of spatial structures can not only be be obtained by deliberately added stimuli but also by random fluctuations. The resulting effects are often counterintuitive [8, 71, 81, 95]. Properly chosen fluctuations in excitable systems are responsible for improved wave transmission [55], enhanced signal detection [36, 72], pattern formation [105], phase synchronization [87], improved wave propagation [55], mean field oscillations [131], coherent wave nucleation [7] and other phenomena.

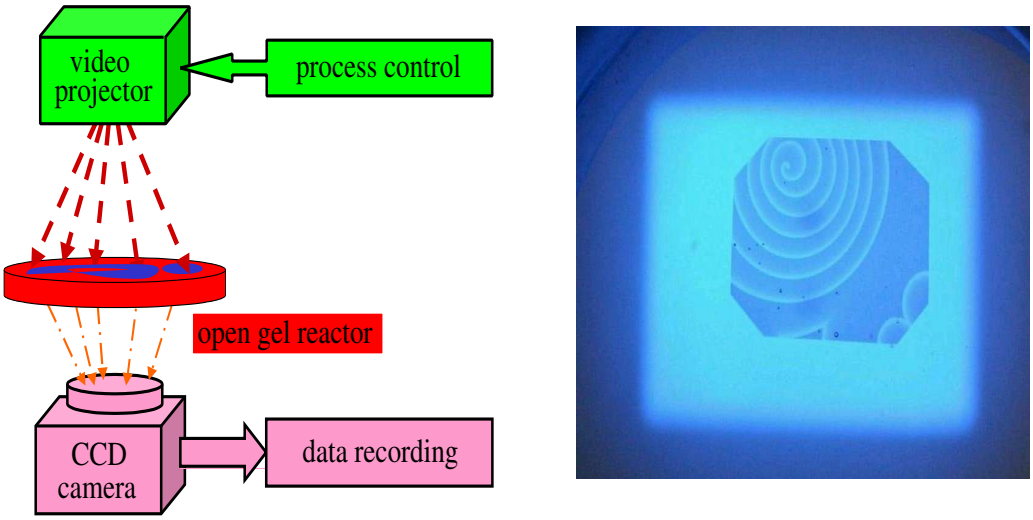


Figure 1.2: Rotating spiral waves in the light sensitive Belousov-Zhabotinsky reaction. Left panel: Schema of the setup at Technische Universität Berlin. The reaction takes place in a thin gel layer (octagon in the right panel). The video projector projects light of such an intensity that the dynamics of the reaction becomes excitable. The image is taken by a CCD camera and recorded. Right panel: Recorded image. The image shows the concentration of the oxidized form of the reaction catalyst. Experimental details can be found in [6]. Printed with permission from H. Engel and V. Beato.

## 1.2 Neuron Dynamics

One of nature's best researched examples of excitability is the neuron. In this section we therefore take a closer look at it, exemplarily for other excitable systems. First, we mention its physiology. There exist many mathematical models describing the dynamics of neurons. We present some of the most widely investigated ones and put special emphasis on the FitzHugh-Nagumo model which is used throughout this work. We discuss the interaction of many neurons, show how neurons are coupled in the brain and discuss the question of the best way to model this coupling. In vivo neurons are under permanent influence of fluctuating forces [119]. We address the question of how to incorporate these fluctuations to neuron models.

Since this can be only a brief sketch of the topic we want to refer to other analyses here. The well-disposed reader can find more detailed studies on neuron models for example in [30, 40, 61].

### Single Neuron Models

A typical neuron consists of three main parts: The dendritic branches (the input part), the soma (the processing part), and the axon (the output part). The dendritic branches form a widely ramified net. At the many ends it receives input from other neurons via synapses (order of magnitude $10^4$). Some neurons also receive input from receptors that are connected to the outside world (e.g. visual input in the retina). A signal coming to a synapse initiates in the dendrite a spatiotemporal modulation of the voltage across the cell membrane. The membrane is a rather good insulator except for ion channels and ion pumps within it. Their activity can be controlled and thereby the potential difference between the outside of the cell and the inside can be influenced. Their action causes the voltage difference initiated at the synapse to travel towards the soma.

Once the dendritic activity reaches the soma it is processed. In its easiest form this processing is approximated by simple integration. Once the integrated input from many synapses reaches a certain threshold a strong response is initiated consisting of another spatiotemporal modulation of the voltage drop across the cell membrane. The modulation of the voltage, also called an action potential, propagates from the soma along the axon. It should be mentioned here, that not all signals arriving at the soma assist its excitation. It depends on the character of the synapse whether a signal it receives favors (excitatory synapse) or hinders (inhibitory synapse) excitation at the soma. About 80 percent of all synapses are excitatory.

In contrast to the dendritic case where the voltage across the membrane decreases on its way from the synapse to the soma the action potential is a solitary pulse. The axon too, repeatedly branches out. The action potential runs through the different branches undamped until it reaches the end of these branches which again are connected to other neurons (or executing organs, e.g. muscles) via synapses. At the end of such a branch neurotransmitters are released to the outside of the presynaptic membrane which then diffuse through the so-called synaptic cleft to the dendrites of e.g. the next neuron and the process starts over again.

Several models with different levels of abstraction have been proposed for describing the action of a neuron. In their celebrated work from 1952, for which they later gained the Nobel prize, Hodgkin and Huxley studied the giant nerve fiber of a squid [52]. Their model states that the conductance of the membrane is influenced by flows of sodium, potassium, and other ions through ion channels in the cell membrane. These channels are opened and closed via messenger particles. With $n$, $m$, and $h$ the probability for the corresponding ion gates in the ion channels to be permissive and $g_{Na}$, $g_K$, and $g_L$ the conductance of the membrane for sodium, potassium and a leakage current, respectively, they proposed the following set of

coupled differential equations:

$$\begin{aligned} \dot{V} &= \frac{g_K n^4 (V - E_K) + g_{Na} m^3 h (V - E_{Na}) + g_L (V - E_L)}{C_M} \\ \dot{n} &= \alpha_n (1 - n) - \beta_n n \\ \dot{m} &= \alpha_m (1 - m) - \beta_m m \\ \dot{h} &= \alpha_h (1 - h) - \beta_h h \end{aligned} \tag{1.1}$$

Here $V$ is the voltage across the membrane, $C_m$ is the capacity of the membrane, and $E_{Na}$, $E_K$, and $E_L$ are the reversal potentials. In the experiment the flow rates of the messenger particles into and out of the membrane depend exponentially on the voltage (for details see e.g. [112]).

A simpler version of a neuron model was derived by FitzHugh [34] and independently by Nagumo, Arimoto and Yoshizawa [85]. It consists of two dynamical variables, only:

$$\begin{aligned} \dot{x} &= x - x^3 - y \\ \dot{y} &= \epsilon (x - ay - b) \end{aligned} \tag{1.2}$$

The FitzHugh–Nagumo (FHN) was derived from the Hodgkin-Huxley model but its range of application has been extended beyond neuron dynamics. We will use it extensively in this work and devote to it an extra section in chapter 3. See there for further details. In the FHN model a first step of abstraction has been applied: While the first variable $x$ represents the voltage across the neuron membrane the second variable $y$ has no direct physiological meaning. It is rather a general recovery variable.

Further abstraction has led to the integrate-and-fire (IF) neuron and the leaky integrate-and-fire (LIF) neuron model:

$$C\dot{V} + \frac{V(t)}{R} = I(t) \tag{1.3}$$

Eq. 1.3 represents the LIF model. The IF model is obtained by setting the second term on the left hand side to zero. Computations are started with some initial value $V_0$. Once a certain threshold value $V_{th}$ is reached $V$ is reset to the initial value $V_0$. These resetting events are interpreted as spiking events. In this form all biological mechanisms for the creation of the spike and its transmission are neglected. Although other opinions exist [125] many neurologists believe that the information that is processed in the brain is completely encoded in the spiking times [99]. With notable success [70] the IF and the LIF models reduce the dynamics of the neuron to a dynamics of spike events.

There are many more neuron models like the Hindmarsh-Rose [51] and the $\Theta$-neuron model. For a more detailed analysis see [40, 61].

### Neural Coupling

The functional properties of the brain are not determined by the single neuron dynamics alone. The are rather due to a complex interplay between a huge number of them. The individual states of all the neurons do not seem to determine the functional state of the brain (an adult human looses about $10^5$ neurons per day) but it is rather a complex state of the collectivity of the neurons. Their combined behavior is an expression of deliberate actions or of pathological behavior. An increased amount of synchrony between brain regions leads to tremor as found in Parkinson disease [116, 117] while too little synchrony is a sign of autism [126].

The gross of human sensory processing is performed in the neocortex which consists of the so-called gray matter, folded tissue between the scalp and the white matter. It has an area on the order of $3000cm^2$ and a depth of about $2-3$ mm. The roughly $10^{10}$ neurons in human neocortex are not homogeneously distributed but they are arranged in six layers parallel to the large surface. Interneural connections are concentrated within some of these layers [44].

Also within the surface plane the neurons are not homogeneously distributed. In minicolumns, anatomical and functional units of about $20 - 50\mu m$ diameter, about 110 neurons are grouped together [24]. It was shown that connections from neurons of specific layers are concentrated strongly along the axis of the microcolumn [69]. On these small scales also nonsynaptic interactions exist [30].

There exist larger functional units in neocortex: Macrocolumns have an typical diameter of 2 mm and a population of $10^5 - 10^6$ neurons, Broadman regions of 5 cm and $10^8$ neurons. Last but not least neocortex is separated into the two brain hemispheres.

Within a cubic centimeter of brain tissue there are axons with combined length of about one kilometer. In a good approximation every neuron sends an axon into the white matter that reenters neocortex at a different site. Coupling between the different functional units is not uniform. While within a minicolumn almost uniform neuronal activity exists neurons from regions of the brain that are some distance apart usually show much less synchronized behavior. Also, coupling topology within functional regions differs from region to region. For example in the part of neocortex responsible for vision different sites are coupled that form a periodic (hexagonal) pattern [9]. Furthermore, due to the release of neuromodulators the behavior of neocortex can be altered such that, depending on the brain state, local or global dynamics [30] dominate. For a more competitive treatment of neural coupling see [15, 30, 35].

### Noise in Neuron Ensembles

In vivo experiments of neuronal activity show a high degree of irregularity. On the one hand there is certainly some kind of code inside this signal that lets us think what we think and perform reasonable tasks. On the other hand is was found that if a certain signal is given as an input to an individual neuron its exact response varies from trial to trial [61]. This suggests that neuronal output consists of a meaningful signal [114] as well as of random fluctuations.

The origins of fluctuations (noise) in neurons are manifold. One kind of noise that is literally omnipresent is thermal noise. Its influence on neuronal dynamics is rather negligible compared to other sources, though [40]. The influence of the temporally varying finite number of open and closed ion channels, important in the transmission of the action potential, is much more important (*channel noise*). This process is far too complex for a deterministic description. We cannot but treat its influence stochastically. If one of the aforementioned fluctuations leads to the emission of a spike it serves as a random input for other neurons. Fluctuating input (*synaptic noise*) can also come from other sources: If the input of a receptor varies too quickly for a functional response it is reasonably modeled as noise. In neural populations differences between the individual neurons can be accounted for by fluctuations.

Depending on the model under study the incorporation of the fluctuations into the model can be orientated closer to or farther from the biological source. In the Hodgkin-Huxley model 1.1 for example fluctuations in the conductance of the membrane can be accounted for by adding noise to the dynamical variables for the messenger particles. For the leaky integrate-and-fire model 1.3 on the other hand fluctuations can only be implied as a general phenomenon. The question of the properties of the noise are closely related to this problem. As we will show in sec. 3.1 two noise terms with different properties inserted at different places in the FHN model can have the same influence on the dynamics.

For high firing rates arriving at the synapses of a neuron and for a small conductance change due to a single input spike, the synaptic current tends to a Wiener process. This is called the diffusion approximation [119].

Summarizing, it can be stated that the simulation of neural networks is a tedious task. In the above paragraphs we have concentrated on neocortex. Other neuron populations with different features exist. In this work we do not try do mimic the physiological aspects of noise and coupling as close as we can. We rather investigate generic situations in order to understand general mechanisms. Investigations of excitable systems with local or global coupling and with different noise sources will prove useful for this aim. Above all we do not explicitely investigate neurons. We have picked them merely as an example of an excitable medium. We hope that our results prove useful for the many fields in which excitable dynamics

matter.

## 1.3 Outline

A convenient and widely used tool to model dynamical systems with noise are Langevin equations, that is stochastic differential equations. An alternative approach is to describe these systems by their probability distribution. This distribution is composed by its moments or equivalently by its cumulants. We use a method based on cumulant dynamics in many places of this work. We therefore describe it in chapter 2. For our study it was often necessary to apply an approximation to the resulting system of equations. We introduce this approximation and discuss possible alternatives.

In chapter 3 we select one neuron model namely the FitzHugh-Nagumo model. In the case of an uncoupled individual system there exists a unique solution of the Fokker-Planck equation. We study this solution numerically and display the probability flux.

In chapter 4 we investigate a system with multiplicative noise and global coupling exhibiting a pure noise induced pitchfork bifurcation for which an exact solution is already known. We apply the method of the cumulant dynamics to the problem and study its performance. For a generalization of the model the exact solution is not known. In accordance with simulations of Langevin dynamics the cumulant method shows pure noise induced limit cycle oscillations and pure noise-induced excitability.

The interaction of noise and coupling shows interesting effects in the FitzHugh-Nagumo system, too. In chapter 5 we present a variety of different dynamical regimes found in this system ranging from small scale oscillations to spiking, period doubling, and chaos. We show in section 5.2 that increasing spatial correlations lead to a behavior resembling coherence resonance.

Up to this part we have concentrated on systems without spatial structure. In chapter 6 we examine an excitable 2-d system under the influence of additive dichotomous noise. We treat different cases where the noise varies either in space or in time or in both and we show that in all three cases an increase of noise leads to an enhancement of spatial order.

# Chapter 2

# Moment Dynamics

There are different ways to mathematically treat fluctuations. Between them there is the general difference that some are intrinsically stochastic, i.e. they incorporate random numbers, and some are deterministic. The latter deal with statistical properties of the fluctuations. The most popular representatives are the master equation and the Fokker-Planck equation (FPE). We will use the FPE for our investigations in chapter 3.

In this chapter (section 2.1) we introduce a different method that was extensively used in the present work. It is based on the moments of an ensemble distribution. The method will prove useful in chapters 4 and 5 for analytically and numerically analyzing different stochastic dynamical systems. We introduce a simple toy model and investigate it with alternative methods in order to demonstrate the benefit of this new method.

It turns out that for an effective use of the method we have to apply an approximation to the resulting system of equations for the moments. Different approximation methods are introduced and their effectiveness is discussed in section 2.2. The different approximation techniques are applied to the toy model introduced in section 2.1.

We will sum up the results in section 2.3.

## 2.1 Derivation of Moment Dynamics and Dynamics of the Mean

### 2.1.1 Definitions

Let us consider a probability distribution $p(x)$. Its n-th moment $M_n$ is defined as

$$M_n = \langle x^n \rangle = \int_{-\infty}^{\infty} x^n p(x) dx \tag{2.1}$$

The normalization condition for the probability density yields $M_0 = 1$. The first moment $M_1$ is the mean of the distribution. Often it is useful to use instead of the absolute value of $x$ its value relative to the mean. Its characteristics are described by the central moments

$$\mu_n = \langle (x - \langle x \rangle)^n \rangle = \int_{-\infty}^{\infty} (x - \langle x \rangle)^n p(x) dx \tag{2.2}$$

The zeroth central moment is again given by the normalization condition of the probability ($\mu_0 = 1$), the first central moment is zero ($\mu_1 = 0$), the second is the variance of the distribution.

The moments of a distribution are closely related to its cumulants $\kappa_n$. In order to express this relation we introduce the characteristic function $C(u)$ as the average

$$C(u) = \langle e^{iux} \rangle = \int_{-\infty}^{\infty} e^{iux} p(x) dx \tag{2.3}$$

The definition of the cumulants can be found in many textbooks [56, 101]. We use the following relation:

$$C(u) = \sum_{n=0}^{\infty} \frac{(iu)^n}{n!} M_n = \exp\left( \sum_{n=1}^{\infty} \frac{(iu)^n}{n!} \kappa_n \right) \tag{2.4}$$

This expression not only defines the cumulants of a distribution but at the same time provides the relation between the moments of a distribution and its cumulants. If all moments are known then under certain circumstances [91] the probability density is uniquely defined. We can then construct the characteristic function from the moments and via inverse Fourier transformation get back to the probability density.

Of special importance to us are cases in which we do not deal with only one random variable but with several (e.g. the FitzHugh-Nagumo system treated in chapters 3, 5, and 6). The concept of the moments is readily extended to such cases. We give here the example for the central moments of a two variable system:

$$\begin{aligned} \mu_{m,n} &= \langle (x - \langle x \rangle)^m (y - \langle y \rangle)^n \rangle \\ &= \int_{-\infty}^{\infty} \int_{-\infty}^{\infty} (x - \langle x \rangle)^n (y - \langle y \rangle)^m p(x, y) dx dy \end{aligned} \tag{2.5}$$

An algorithm for expressing the cumulants of a distribution in terms of its moments and vice versa along with several examples that will be needed in the course of this work is given in appendix A.

### 2.1.2 Moment Dynamics for a One-Variable System

Let us now consider the following system of $N$ identical coupled units each of which is described by one dynamical variable. The individual units are subject to independent multiplicative noise (Additive noise is treated equivalently. $g(x_i)$ is then a constant.). The corresponding system of Langevin equations reads:

$$\dot{x}_i = f(x_i, \bar{x}) + g(x_i)\xi_i(t) \qquad i = 1..N \tag{2.6}$$

The dot over the $x$ denotes the derivative with respect to time. $\bar{x} = \sum_{i=1}^{N} x_i$ is the mean value of the system. Special focus will be on systems where the function $f$ has the form

$$f(x_i, \bar{x}) = \hat{f}(x_i) + K(\bar{x} - x_j) \tag{2.7}$$

This corresponds to an ensemble of statistically identical elements in which each individual element is coupled with strength $K$ to the mean of the $N$ units. This *global coupling* will be used in the models of the chapters 4 and 5. Different coupling terms have been considered in [48]. The fluctuating term $\xi_i(t)$ is Gaussian and white. Without loss of generality we set its mean $\langle \xi_i \rangle = 0$. The correlations are given by

$$\langle \xi_i(t_1)\xi_j(t_2) \rangle = 2T\delta_{i,j}\delta(t_2 - t_1) \tag{2.8}$$

The system of equations 2.6 is interpreted in the Stratonovich sense. Systems with correlated noise have been considered in [47].

Eq. 2.6 is not the most general form we can treat with this method. More complex systems, especially with more than one variable per site are discussed later in this chapter and in appendix A.

Since eq. 2.6 describes a finite system the mean $\bar{x}$ is a stochastic variable. It is generally time-dependent. The Fokker-Planck equation for the system 2.6 with global coupling 2.7 can easily be written down:

$$\begin{aligned} \frac{\partial}{\partial t} P(x_1, \ldots x_N, t) &= -\sum_{i=1}^{N} \frac{\partial}{\partial x_i} \left[ \left( \hat{f}(x) + Tg(x)g^{(1)}(x) \right) P(x_1, \ldots x_N, t) \right] \\ &+ \sum_{i=1}^{N} \sum_{j=1}^{N} \frac{\partial}{\partial x_i} \left[ (x_i - x_j) P(x_1, \ldots x_N, t) \right] \\ &+ \sum_{i=1}^{N} \frac{\partial^2}{\partial x_i^2} \left[ TP(x_1, \ldots x_N, t) \right] \end{aligned} \tag{2.9}$$

$g^{(n)}$ denotes the $n$–th derivative of $g$ with respect to its argument. The system of $N$ units is ergodic. The Fokker-Planck equation has a unique solution that is globally attracting.

Let us now come back to the system of Langevin equations 2.6 and expand the functions $f$ and $g$ in a Taylor series around the mean $\bar{x}$. We obtain:

$$\dot{x_i} = \sum_{n=0}^{\infty} \frac{(x_i - \bar{x})^n}{n!} \Big[ f^{(n)}(x_i, \frac{x_i}{N} + \sum_{j \neq i} \frac{x_j}{N})|_{x_i=\bar{x}} + g(x_i)^{(n)}|_{x_i=\bar{x}} \xi(t) \Big] \tag{2.10}$$

$f^{(n)}$ is the $n$-th derivative with respect to the argument $x_i$. If $f$ and $g$ are polynomials the infinite sum breaks off at some finite value of $n$ since the derivative becomes zero afterwards.

The second argument of $f$ is written somewhat intricately. It is nothing more than the average $\bar{x}$ but by writing it like this we see that we have to consider $\bar{x}$, too, when taking the derivative. For small $N$ the dynamics of the variable $x_i$ strongly depends on the actual realization of the stochastic variable $x_j$.

Now we are interested in the limit of a large number of individual systems ($N \to \infty$). We assume that the ensemble of $N$ individual units obeys *molecular chaos*. This concept is also known as *repeated randomness assumption*, *Stosszahlansatz* or *random phase approximation* [56]. It states that the enormous number of microscopic variables ($x_i$) varies so much more rapidly than the macroscopic variables (e.g. $\bar{x}$) that almost instantly an equilibrium distribution is reached. This distribution belongs to the macroscopic variables as if these were fixed. Since the macroscopic variables are not fixed this distribution must be readjusted continously. The probability distribution of the single variables does not depend on the actual realizations of the other variables anymore. Their correlations disappear. The probability densities decouple:

$$P(x_1, x_2, \ldots, x_n, t) = P(x_1, t)P(x_2, t) \ldots P(x_N, t) \tag{2.11}$$

$\bar{x}$ can be expressed in terms of the single particle distribution function (we drop the index of $x_i$):

$$\bar{x} = \int x P(x, t) dx \tag{2.12}$$

Using this expression we can write down the corresponding Fokker-Planck equation for the one particle distribution density and we note that it becomes nonlinear:

$$\begin{aligned} \frac{\partial}{\partial t} P(x,t) &= -\frac{\partial}{\partial x} \Big[ \Big( \hat{f}(x) - Kx + K \int_{\mathbb{R}} x P(x,t) dx \\ &+ T g(x) g^{(1)}(x) \Big) P(x,t) \Big] + T \frac{\partial^2}{\partial x^2} P(x,t) \end{aligned} \tag{2.13}$$

The nonlinearity has severe implications on the properties of the stationary solution. The uniqueness of the solution is not guaranteed any more. Also, it is not

obliged to be globally attracting. The ergodicity of the system is lost. It is not valid to interchange averaging over time and averaging over the ensemble.

The assumption of molecular chaos was applied in a variety of different systems as for example in noise driven bistable systems [27, 28, 108], coupled noisy self-sustained oscillators [10, 11], and coupled phase oscillators [66]. It was shown to be valid in the limit of $N \to \infty$ in these systems.

Let us look in the limit of large $N$ at the deterministic macroscopic variable $\langle x \rangle = \lim_{N\to\infty} \frac{1}{N} \sum_{n=1}^{\infty} x_n$. We can now average over eq. 2.10 and write for the temporal evolution of $\langle x \rangle$:

$$\dot{\langle x \rangle} = \sum_{n=0}^{\infty} \frac{\mu_n}{n!} \Big[ f^{(n)}(x, \langle x \rangle)|_{x=\langle x \rangle} + T[g^{(1)}(x)g(x)]^{(n)}|_{x=\langle x \rangle} \Big] \tag{2.14}$$

with the central moments $\mu_n$ defined above. Remember that $\mu_0 \equiv 1$ and $\mu_1 \equiv 0$.

We have thus succeeded in expressing the dynamics of the mean of the $N$ systems by the central moments of their distribution. We have changed from a description of the system of $N$ units in terms of the microscopic dynamics (Langevin equations) to a description in terms of the macroscopic dynamics.

So far we have accomplished little since the central moments that we need to describe the dynamics of the mean are in general also time dependent. We need to describe their dynamics, too. From the system of equations 2.6 we can do this. The calculations are rather lengthy and we postpone them to the appendix A. Here, we restrict ourselves to give the results:

$$\begin{aligned} \dot{\mu}_n &= \sum_{m=0}^{\infty} n \frac{\mu_{n-1+m}}{m!} \Big[ f^{(m)}(x)|_{x=\langle x \rangle} + T(g(x)g^{(1)}(x))^m|_{x=\langle x \rangle} \Big] \\ &+ \sum_{m=0}^{\infty} n(n-1) \frac{\mu_{n-2+m}}{m!} T(g^2(x))^{(m)}|_{x=\langle x \rangle} \end{aligned} \tag{2.15}$$

It is interesting to look at the situation where the functions $f$ and $g$ that determine the dynamics are polynomials. This is the case in the examples we study in chapters 4 and 5. From equation 2.14 we see that the highest order moment that the dynamics of the mean depends on is given by the highest power of $x$ in $f + Tgg^{(1)}$.

From equation 2.15 we can see that the dynamics of the $n$-th central moment depends on the $(n+m)$-th central moment. This $m$ is given by the maximum of the highest powers of $x$ in $f + Tgg^{(1)}$ minus one and $g^2$ minus two.

### A Toy Model

Let us apply what we have just derived to a simple model:

$$\begin{aligned} f(x) &= a + bx + K(x - \langle x \rangle) \\ g(x) &= d + ex \end{aligned} \tag{2.16}$$

We again use the Stratonovich interpretation. From eq. 2.16 on we simplify our notation. We neglect the notation $\bar{x}$ and write only $\langle x \rangle$. It goes without saying that the results from the simulations of Langevin equations of a finite amount of individual units stay stochastic variables.

According to eqs. (2.14) and (2.15) the dynamics of the mean and the second central moment are given by:

$$\begin{aligned} \dot{\langle x \rangle} &= \langle x \rangle (b + e^2 T) + a + deT \\ \dot{\mu}_2 &= 2e^2 T \langle x \rangle^2 + 4deT\langle x \rangle + 2d^2 T + \mu_2(2b - 2K + 4e^2 T) \end{aligned} \tag{2.17}$$

We find that the dynamics of the mean and the dynamics of the second central moment do not depend on any other moment. We also note that the dynamics of the mean does, for the global coupling term we have chosen, not depend on the coupling constant $K$. In the term in eq. 2.14 with $m = 1$ we have $\langle \langle x \rangle - x \rangle = 0$ and the term $\frac{\delta}{\delta x}(K(\langle x \rangle - x))$ is multiplied by $\mu_1$ which is zero. Higher derivatives are also zero. Thus, a coupling term of this form never enters the dynamics of the mean. Due to the accordant arguments it enters the dynamics of the second moment via the term $-2K\mu_2$.

For the mean we can easily compute:

$$\langle x \rangle = \left( \langle x \rangle_0 + \frac{a + deT}{b + e^2 T} \right) e^{(b + e^2 T)t} - \frac{a + deT}{b + e^2 T} \tag{2.18}$$

with the initial condition that $\langle x \rangle$ takes the value $\langle x \rangle_0$ at time $t = 0$. $\langle x \rangle$ goes to $a + deT$ for large $t$ if $b + e^2 T < 0$ and diverges otherwise (For $b + e^2 T = 0$ and $a = -deT$ the mean $\langle x \rangle$ stays constant.). The stationary values for $\langle x \rangle$ and $\mu_2$ are given by (The hat marks the steady state solutions.):

$$\begin{aligned} \hat{\langle x \rangle} &= \frac{a + deT}{b + e^2 T} \\ \hat{\mu}_2 &= \frac{\left( e\hat{\langle x \rangle} + d \right)^2 T}{K - (b + 2\, e^2\, T)} \end{aligned} \tag{2.19}$$

We do not want to investigate this solution in detail now but postpone the study to the next section where we will treat this model as a limit of a little more complex system.

The temporal evolution of the higher central moments does depend on other moments. Their dynamics is given by:

$$\begin{aligned}\dot{\mu}_n &= \mu_{n-2} n(n+1)T(d^2 + 2de\langle x\rangle + e^2\langle x\rangle^2) \\ &+ \mu_{n-1}(n(a + b\langle x\rangle + eT(3d + \langle x\rangle + e\langle x\rangle^2)) + 2n^2 eT(d + e\langle x\rangle)) \\ &+ \mu_n(n(b - K + 3Te^2) + 2n^2 Te^2) \end{aligned} \tag{2.20}$$

The system of equations for the dynamics of the higher central moments does not decouple but since we can explicitely compute the lower order moments we can successively also compute the higher order moments. We note that from a quadratic nonlinearity in $f$ or in $g$ on, the dynamics of the $n$-th central moment depends on higher moments and can generally not be directly computed with this method.

A simple model with such nonlinearities reads:

$$\begin{aligned} f(x) &= a + bx + cx^3 + K(x - \langle x\rangle) \\ g(x) &= d + ex \end{aligned} \tag{2.21}$$

Here we chose a cubic nonlinearity in the function $f$ in order to guaranty boundedness. The dynamics of the moments with explicitely written dynamics of the mean and of the second central moment read:

$$\begin{aligned}\dot{\langle x\rangle} &= a + d\,e\,T + c\,\langle x\rangle^3 + \langle x\rangle\,\left(b + e^2\,T + 3\,c\,\mu_2\right) + c\,\mu_3 \\ \dot{\mu}_2 &= 2\,\langle x\rangle^2\,\left(e^2\,T + 3\,c\,\mu_2\right) + 2\,\langle x\rangle\,\left(2\,d\,e\,T + 3\,c\,\mu_3\right) \\ &+ 2\,\left(d^2\,T + b\,\mu_2 - K\,\mu_2 + 2\,e^2\,T\,\mu_2 + c\,\mu_4\right) \\ \dot{\mu}_n &= d^2\,(n-1)\,n\,T\,\mu_{n-2} + a\,n\,\mu_{n-1} + d\,e\,n\,(2\,n-1)\,T\,\mu_{n-1} + c\,n\,x^3\,\mu_{n-1} \\ &+ b\,n\,\mu_n - K\,n\,\mu_n + e^2\,n^2\,T\,\mu_n + n\,x^2\,\left(e^2\,(n-1)\,T\,\mu_{n-2} + 3\,c\,\mu_n\right) \\ &+ x\,(K\,n\,\mu_{n-1} + n\,(2\,d\,e\,(n-1)\,T\,\mu_{n-2} + b\,\mu_{n-1} - K\,\mu_{n-1} \\ &+ e^2\,(2\,n-1)\,T\,\mu n - 1 + 3\,c\,\mu_{n+1})) + c\,n\,\mu_{n+2} \\ &= F(\mu_{n-2}, \mu_{n-1}, \mu_n, \mu_{n+1}, \mu_{n+2}) \end{aligned} \tag{2.22}$$

The eqs. 2.22 form an infinite system of coupled equations. We cannot solve this system exactly. Suitable approximation techniques are required to close this infinite system.

## 2.2 Approximation Techniques

There are several possible ways to apply approximations to the system 2.22. Common techniques to reduce it to a finite set of equations are to set either the central

moments [103] or the cumulants [47, 75, 76] above a certain order to zero. Each method has its own pros and cons.

We emphasize that for all probability distributions the cumulants either vanish after the first cumulant (no fluctuations), or after the second one (Gaussian distribution; see sec. A.4), or all of them have to be taken into account [45, 93]. Truncating the hierarchy after a different finite number of cumulants is inconsistent with non-negative probability distributions. This does not necessarily mean that the results obtained for the mean and for the moments or cumulants are altogether useless [103].

Similarly it is not possible that all central moments (or non-central moments) from a certain order other than one on become zero.

### Neglecting Central Moments From a Certain Order On

The probably easiest way to truncate the infinite system of eqs. 2.14 and 2.15 is to neglect all central moments from second order on.

$$\mu_n = 0 \qquad n \geq 2. \tag{2.23}$$

Since the first central moment is always zero (as is the first cumulant; see eq. A.13) this approach is equivalent to neglecting all central moments from first order on ($n \geq 1$). In other words we neglect all fluctuations. The corresponding probability distribution is then given by a delta peak located at the mean. The dynamics of the mean (which is the only dynamical variable) is then for additive noise given by the deterministic dynamics. For multiplicative noise the dynamics (using the Stratonovich interpretation) is given by the deterministic dynamics plus the Stratonovich shift (cf. eq. 4.7). In chapter 4 we mention some studies that follow this method and apply it to our own problem. For the problem at hand (eq. 2.21) the resulting dynamical system reads:

$$\dot{\langle x \rangle} = a + Ted + (b + Te^2)\langle x \rangle + c\langle x \rangle^3 \tag{2.24}$$

We note at once that the dynamics of the mean $\langle x \rangle$ does not depend on the coupling strength $K$. Such a dependence of the dynamics can thus not possibly be reproduced in this approximation.

For small noise intensities the probability distribution of an ensemble is often strongly concentrated around the mean. In the case of a globally coupled system like eq. 2.6 with 2.7 this can normally be aided by high coupling coefficients $K$. The high order central moments are then usually small compared to the low oder ones. In this case it may be a useful approximation to neglect the central moments from a certain order on. Unfortunately it cannot be guaranteed that taking into account one more central moment yields better results than not taking it into account.

When setting all central moments above second order to zero the dynamics reads:

$$\begin{aligned} \dot{\langle x\rangle} &= a + deT + \langle x\rangle(b + e^2T + 3c\mu_2) + c\langle x\rangle^3 \\ \dot{\mu_2} &= 2x^2\left(e^2T + 3c\mu_2\right) + 4xdeT + 2\big(d^2T + \mu_2(b - K + 2e^2T)\big) \end{aligned} \tag{2.25}$$

The effect of the coupling now enters the dynamics of the mean. It does so not directly but via the second central moment.

When setting all central moments above third order to zero the dynamics reads:

$$\begin{aligned} \dot{\langle x\rangle} &= a + deT + c\mu_3 + \langle x\rangle(b + e^2T + 3c\mu_2) + c\langle x\rangle^3 \\ \dot{\mu_2} &= 2x^2\left(e^2T + 3c\mu_2\right) + 2x\left(2deT + 3c\mu_3\right) + 2\big(d^2T + b\mu_2 \\ &- K\mu_2 + 2e^2T\mu_2\big) \\ \dot{\mu_3} &= 3cx^3\mu_2 + 9cx^2\mu_3 + 3x\left(b\mu_2 - K\mu_2 + 5e^2T\mu_2\right) \\ &+ 3\big(a\mu_2 + 5deT\mu_2 + Kx\mu_2 + b\mu_3 - K\mu_3 + 3e^2T\mu_3\big) \end{aligned} \tag{2.26}$$

When setting all central moments above fourth order to zero the dynamics reads:

$$\begin{aligned} \dot{\langle x\rangle} &= a + deT + c\mu_3 + \langle x\rangle(b + e^2T + 3c\mu_2) + c\langle x\rangle^3 \\ \dot{\mu_2} &= 2x^2\left(e^2T + 3c\mu_2\right) + 2x\left(2deT + 3c\mu_3\right) + 2\big(d^2T + b\mu_2 \\ &- K\mu_2 + 2e^2T\mu_2 + c\mu_4\big) \\ \dot{\mu_3} &= 3cx^3\mu_2 + 9cx^2\mu_3 + 3x\left(b\mu_2 - K\mu_2 + 5e^2T\mu_2 + 3c\mu_4\right) \\ &+ 3\big(a\mu_2 + 5deT\mu_2 + Kx\mu_2 + b\mu_3 - K\mu_3 + 3e^2T\mu_3\big) \\ \dot{\mu_4} &= 4cx^3\mu_3 + 4x^2\big(3e^2T\mu_2 + 3c\mu_4\big) + 4x\big(6deT\mu_2 + b\mu_3 - K\mu_3 + 7e^2T\mu_3\big) \\ &+ 4\big(3d^2T\mu_2 + a\mu_3 + 7deT\mu_3 + Kx\mu_3 + b\mu_4 - K\mu_4 + 4e^2T\mu_4\big) \end{aligned} \tag{2.27}$$

### Neglecting Cumulants From a Certain Order On

As well as neglecting the central moments from a a certain order on we can do the same with the cumulants. Neglecting all cumulants from second order on means neglecting all fluctuations. This case was treated in the last subsection and leads to eq. 2.24.

The probably most common approach to truncate the set of equations 2.14 and 2.15 or its multi-variable equivalent is to set all cumulants above second order to zero:

$$\kappa_n = 0 \qquad n \geq 3 \tag{2.28}$$

This condition holds for the Gaussian distribution (see sec. A.4). We therefore call it the *Gaussian approximation*. This is the only way (apart from neglecting all

fluctuations) to reduce the infinite set to a finite one without accepting negative or non-normalizable probability densities.

The consequences of this approach are substantial. We assume that the systems are centered according to a Gaussian distribution around the mean. Additional to fixed relations between the even order central moments (see sec. A.4) that means that all odd order central moments vanish. The systems are symmetrically distributed around the mean. The only way to justify these assumptions is to refer to the results that are obtained with the Gaussian approximation (chapters 4 and 5 and literature [47, 75, 76]). All these examples show some deviations of the results obtained by the Gaussian approximation compared to those obtained by different methods but also exhibit remarkable qualitative consistency.

The dynamics for the cumulants for the toy model in Gaussian approximation read:

$$\begin{aligned} \dot{\langle x\rangle} &= a + deT + \langle x\rangle(b + e^2T + 3c\kappa_2) + c\langle x\rangle^3 \\ \dot{\kappa_2} &= 2\big(e^2Tx^2 + 2deTx + d^2T + \kappa_2(b - K + 2e^2T) + 3cx^2\kappa_2 + 3c{\kappa_2}^2\big) \end{aligned} \tag{2.29}$$

We see that the coupling strength $K$ does not directly affect the dynamics of the mean $\langle x\rangle$ but comes in via the second cumulant $\kappa_2$.

We can also neglect all cumulants above third order. As stated above this is not consistent with a non-negative normalizable probability distribution. Still, we can set up the equations:

$$\begin{aligned} \dot{\langle x\rangle} &= a + deT + c\kappa_3 + \langle x\rangle(b + e^2T + 3c\kappa_2) + c\langle x\rangle^3 \\ \dot{\kappa_2} &= 2\big(d^2T + 2deTx + 3cx\kappa_3 + b\kappa_2 - K\kappa_2 + 3cx^2\kappa_2 + 3c{\kappa_2}^2 \\ &+ e^2T\left(x^2 + 2\kappa_2\right)\big) \\ \dot{\kappa_3} &= 3\big(a\kappa_2 + 5deT\kappa_2 + 5e^2Tx\kappa_2 + cx^3\kappa_2 + 9cx{\kappa_2}^2 - K\kappa_3 \\ &+ 3e^2T\kappa_3 + 3cx^2\kappa_3 + 10c\kappa_2\kappa_3 + b\left(x\kappa_2 + \kappa_3\right)\big) \end{aligned} \tag{2.30}$$

Another, less often used method is called the *excess approximation*. It consists of neglecting all cumulants above 4-th order:

$$\begin{aligned} \dot{\langle x\rangle} &= a + deT + c\kappa_3 + \langle x\rangle(b + e^2T + 3c\kappa_2) + c\langle x\rangle^3 \\ \dot{\kappa_2} &= 2\big(d^2T + 2deTx + 3cx\kappa_3 + c\kappa_4 + b\kappa_2 - K\kappa_2 + 3cx^2\kappa_2 + 3c{\kappa_2}^2 \\ &+ e^2T\left(x^2 + 2\kappa_2\right)\big) \\ \dot{\kappa_3} &= 3\big(a\kappa_2 + 5deT\kappa_2 + 5e^2Tx\kappa_2 + cx^3\kappa_2 + 9cx{\kappa_2}^2 - K\kappa_3 \\ &+ 3e^2T\kappa_3 + 3cx^2\kappa_3 + 10c\kappa_2\kappa_3 + b\left(x\kappa_2 + \kappa_3\right) + 3cx\kappa_4\big) \\ \dot{\kappa_4} &= 4\big(a\kappa_3 + 7deT\kappa_3 + bx\kappa_3 + b\kappa_4 - K\kappa_4 + e^2T\big(6{\kappa_2}^2 + 7x\kappa_3 + 4\kappa_4\big) \\ &+ c\left(6{\kappa_2}^3 + x^3\kappa_3 + 10{\kappa_3}^2 + 3x^2\kappa_4 + 3\kappa_2\left(7x\kappa_3 + 4\kappa_4\right)\right)\big) \end{aligned} \tag{2.31}$$

In order to test the different approximations we look at numerical results of the toy model eq. 2.21 for different parameter sets. As order parameter we use the stationary value of the mean which we call $\langle x \rangle_0$. We especially want to test the quality of the approximations for different strengths of the nonlinearity $c$. For properly chosen parameters the dynamical system 2.21 is associated with a bistable potential. In order to obtain better comparability we chose the initial conditions such that the mean did not end up in the *wrong* minimum of the potential.

The results are depicted in fig. 2.1 for $e = 0$, i.e. for purely additive noise.

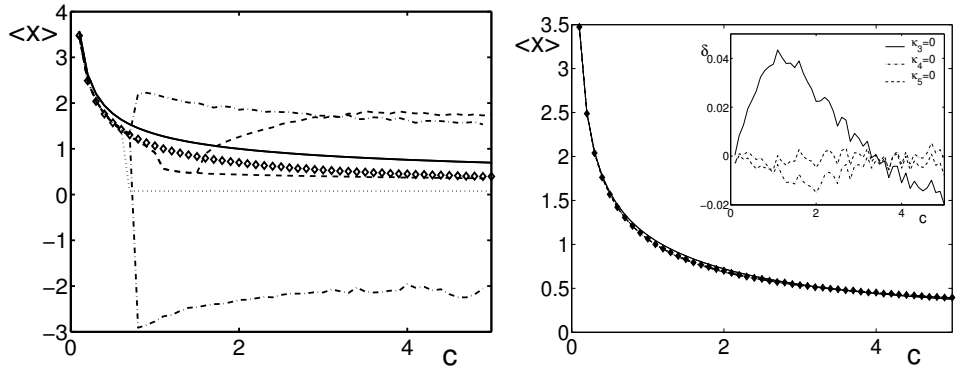


Figure 2.1: Performance of different approximation techniques versus strength of the nonlinearity. In both pictures the results from a Langevin simulation with $N = 100000$ is depicted by the diamonds. Left panel: Moments from order $M$ on have been neglected. Solid line: $M = 2$; dotted line: $M = 3$; dash-dotted: $M = 4$; Dashed: $M = 5$. Where two lines of the same style are shown the solutions oscillated and the minimum and maximum values (computed from several oscillation periods) are both shown. From a certain $c$-value on these approximations (except for the lowest order approximation) show qualitatively wrong results (oscillations). Right panel: Cumulants from order $K$ on have been neglected. Solid line: $K = 3$; dash-dotted line: $K = 4$; dashed line: $K = 5$ (The solution for $K = 2$ is the same as for $M = 2$ in the left panel). In the inset the deviations $\delta$ from the Langevin simulation are shown. Parameters: $a = 1$, $b = 1$, $d = 1$ ,$e = 0$, $T = 1$.

In this case, for $c = 0$ the steady probability distribution of a single uncoupled system is a Gaussian distribution.

We see that for small strengths of the nonlinearity all approximations perform decently. For higher values the approximations that consist of neglecting high order moments completely fail from certain critical values of $c$ on. These critical values are different for each approximation. The more moments are taken into account the higher the $c$ value from which on the approximation method becomes

useless. For large negative $c$ values these methods even predict oscillations of the mean $m_x$. Interestingly, the failure of the approximations is not associated with a sudden increase of the higher (neglected) central moments. The stationary values of these moments are plotted in fig. 2.2.

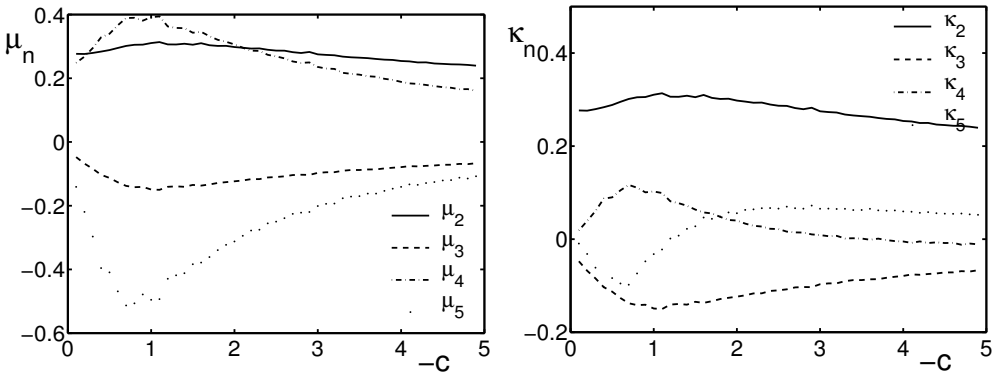


Figure 2.2: Moments (left panel) and cumulants (right panel) as obtained by Langevin simulations with $N = 100000$ versus strength of the nonlinearity $-c$. $c$ is taken negative in order to avoid divergence of $m_x$. The higher order cumulants are small compared to $\kappa_2$. This is a hint that the Gaussian approximation may be a good one. Parameters: $a = 1$, $b = 1$, $d = 1$ ,$e = 0$, $T = 1$.

The approximation methods that are based on neglecting cumulants above a certain order work well for all $c$ values we studied. This is demonstrated in the right panel in fig. 2.1. The discrepancy between the results from the Gaussian approximation and from the Langevin simulations does not monotonically depend on the strength of the nonlinearity but shows a more complex behavior. For a closer look refer to fig. 2.2. The decreasing values of $\kappa_3$ and $\kappa_4$ suggest (For a complete description all cumulants should be looked at.) that the distribution becomes more Gaussian-like again for large negative values of the strength of the nonlinearity $c$.

We have also studied the influence of the noise intensity on the performance of the different approximations. In order to do this we fixed the strength of the nonlinearity $c = -1$ and varied the parameter $d$ which governs the strength of the additive noise. The other parameters remain the same as in the previous case. The results are plotted in fig. 2.3. The influence of strong noise intensities on the approximations that are based on neglecting central moments from a certain order on is rather intuitive. For increasing intensities the corresponding results abruptly deviate from the results of the Langevin simulations successively. Those that take into account more moments fail at a higher noise intensity than those

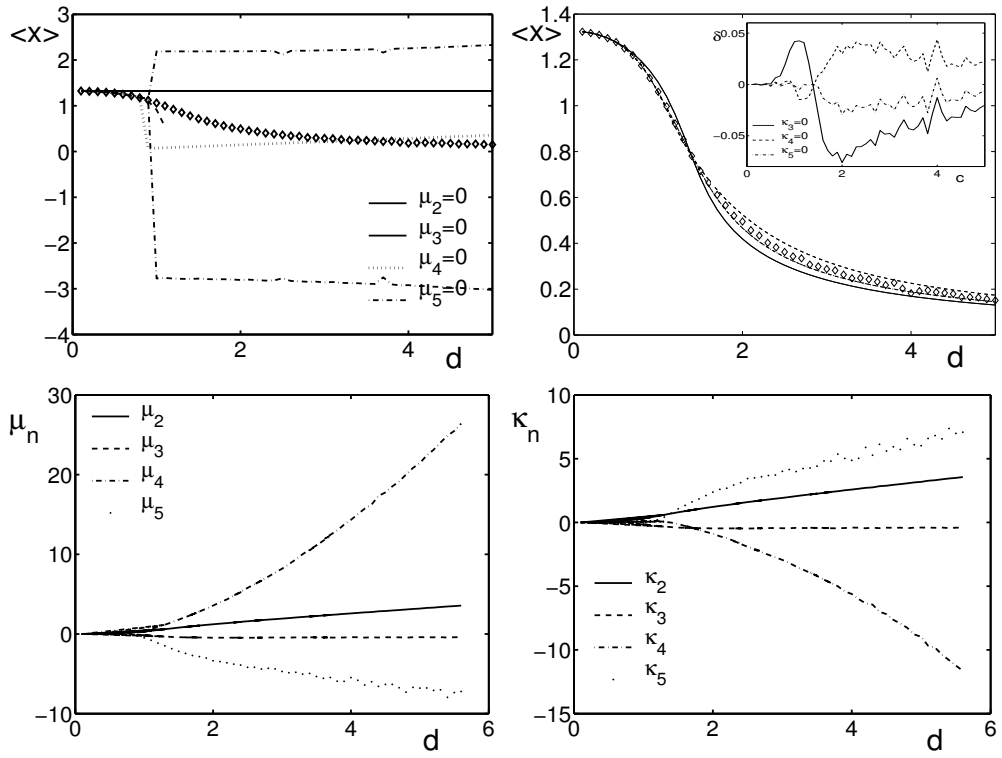


Figure 2.3: Upper row: Performance of the different approximations versus additive noise intensity $d$. Lower row: Moments (left) and cumulants (right) as obtained by Langevin simulations with $N = 100000$. Parameters: $a = 1$, $b = 1$, $c = 1$ ,$e = 0$, $T = 1$.

with less moments. Again the methods that consist of neglecting cumulants from a certain order on overall perform better. Interestingly, for the study with varying strength of the nonlinearity as well as for that with varying noise intensity there is a non-monotonous behavior of the difference of the results from the Langevin simulations and from the cumulant approximation. We cannot conclude that the quantitative performance of the approximation fails for strong noise intensities or for highly nonlinear systems.

We have looked at a special model, only. The performance of the different approximations certainly depends on the model under investigation. Further investigation on the applicability of the methods remains necessary. In the course of this work we will study several models with the help of the moment dynamics but we cannot give an all-embracing answer to this problem.

## 2.3 Summary

We have described a method to analytically describe dynamical systems with additive or multiplicative noise in terms of the central moments of their distribution. Special emphasize was put on ensembles of systems which are globally coupled. If the functions describing the dynamics of the individual system are linear the evolution of the mean of the ensemble and the stationary solution for the moments can be given explicitely in the limit of large particle numbers. If they are nonlinear their dynamics forms an infinite set of coupled equations that we cannot solve. Several approximation techniques were introduced that allowed for a reduction of this infinite to a finite set. Their properties were discussed and their quality demonstrated quantitatively.

# Chapter 3

# Stationary Probability Distributions for the FitzHugh–Nagumo Model

In this chapter we investigate the individual stochastic FitzHugh–Nagumo System (FHN). Locally and globally coupled systems with FHN kinetics are used in chapters 5 and 6. Here we study numerically the stationary probability distributions and the probability flux via the method of the Fokker–Planck equation.

In section 3.1 we introduce the model and give its dynamical properties in some detail. It is followed by a section about a phenomenon where noise induces order into a system which is called coherence resonance (sec. 3.2). We will find reminiscences of this phenomenon in section 3.3 where we present the numerical results from our investigation of the stationary probability distribution corresponding to the stochastic FHN. In the last section (sec. 3.4) we show the flux of the probability.

## 3.1 The FitzHugh–Nagumo Model

The FHN system was first introduced in the early sixties. As mentioned in chapter 1 it was derived from the Hodgkin-Huxley model of the squid giant axon. FitzHugh (1961) [34] and independently Nagumo, Arimoto and Yoshizawa (1962) [85] developed it to describe nerve cell phenomena. Despite its relative simplicity it shares many of the essential features with the Hodgkin-Huxley model and with real neurons. In the course of time it has been applied to a variety of other physical [32,79], chemical [80], and biological [1] systems and has become a standard model for excitable dynamics [71,87]. Whole books have been written that deal explicitely with the FHN [102]. In this section we cannot give a complete treatment but we restrict ourselves to some properties that will be needed in the course of the present work.

The FHN has been studied in a variety of different forms. The model equations

we will consider have a single cubic nonlinearity and read:

$$\begin{aligned} \dot{x} &= x - x^3 - y \\ \dot{y} &= \epsilon\,(x - ay - b) \end{aligned} \tag{3.1}$$

where $\dot{x}$ denotes the derivative of $x$ with respect to time (and $\dot{y}$ respectively). The dynamical variables $x$ and $y$ as well as the parameters $\epsilon$, $a$, and $b$ are taken to be real and positive. Due to reasons that will become clear later the variable $x$ is usually called the *activator* and $y$ the *inhibitor*. In terms of neuron dynamics $x$ describes the voltage drop across the nerve cell membrane. $y$ does not represent a chemical concentration as they were incorporated in the Hodgkin-Huxley model but is rather a general recovery variable.

It is insightful to have a closer look at the so-called *nullclines* of the system 3.1. These are the two functions $y(x)$ that are obtained by setting $\dot{x} = 0$ and $\dot{y} = 0$:

$$y = x - x^3 \tag{3.2a}$$

$$y = \frac{x - b}{a} \tag{3.2b}$$

Eq. 3.2a is usually called the *cubic nullcline* or *activator nullcline*, eq. 3.2b the *linear nullcline* or *inhibitor nullcline*. We will call the region to the left of the minimum (to the right of the maximum) of the activator nullcline the left (right) outer branch and the region between these extrema the middle branch.

The slope and position of the linear nullcline depends on the parameters $a$ and $b$. Some examples are shown in fig. 3.1. At the intersections of the nullclines in

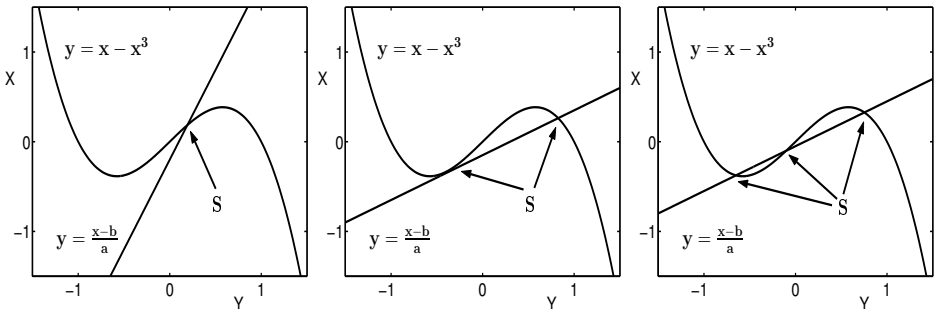


Figure 3.1: Nullclines in the FitzHugh–Nagumo System. Depending on the parameters $a$ and $b$ there exists a different number of fixed points. The fixed points are represented in phase space as intersections of the nullclines. Left panel: 1 fixed point ($a = 0.5$, $b = 0.1$); middle panel: 1 fixed point ($a = 2.0$, $b = 0.3$); right panel: 1 fixed point ($a = 2.0$, $b = 0.1$);

phase space $\dot{x}$ and $\dot{y}$ both vanish. They therefore represent the fixed points of the

system. We see that the FHN can have either one, two or three fixed points. For $a > 1$ there is always exactly one fixed point. For the case $a > 1$ let us define $b^{\pm} := \pm 2a(\frac{1}{3a} - \frac{1}{3})^{\frac{3}{2}}$. For $b^- < b < b^+$ there are three, for $b = b^+$ or $b = b^-$ there are two, and otherwise there is only one fixed point.

In the excitable parameter regime of the FHN there exists only one fixed point. Since our special interest is in these systems we give here the expression for the fixed point for this case $(a, b > 0)$ explicitely:

$$\begin{aligned} x_0 &= \frac{2^{\frac{1}{3}}\ (a-1)}{\left(27\,a^2\,c + \sqrt{108\,(1-a)^3\,a^3 + 729\,a^4\,c^2}\right)^{\frac{1}{3}}} \\ &+ \frac{\left(27\,a^2\,c + \sqrt{108\,(1-a)^3\,a^3 + 729\,a^4\,c^2}\right)^{\frac{1}{3}}}{3\,2^{\frac{1}{3}}\,a} \\ y_0 &= \frac{x_0 - b}{a} \end{aligned} \tag{3.3}$$

Note that the location of the fixed points does not depend on the parameter $\epsilon$. As we will see later their stability does. In the excitable case the fixed point lies on one of the outer branches of the activator nullcline. The reverse statement is true only in the limit $\epsilon \to \infty$.

The stability of the fixed points can be studied via a linear stability analysis. This means that we look at a system initially sitting at the fixed point of interest: $x = x_0$, $y = y_0$. We then apply a small perturbation to the system: $x = x_0 + \delta_x$, $y = y_0 + \delta_y$. The temporal evolution of the perturbation determines the stability of the fixed point.

Our ansatz for $\delta_{x,y}$ is:

$$\delta_x = \tilde{x}e^{\lambda t}, \qquad \delta_y = \tilde{y}e^{\lambda t} \tag{3.4}$$

We insert this ansatz into eqs. 3.1 and neglect terms of second order in the perturbation ($\delta_x^2$, $\delta_x\delta_y$, $\delta_y^2$) and higher. This expresses the fact that we are looking for local stability, only. Large perturbations can show a different behavior.

We can now conveniently write down the linearized equation for the system's temporal evolution as a matrix equation with a matrix $\hat{\mathbf{M}}$ with entries $M_{i,j}$ $(i, j = 1, 2)$ and vector $\mathbf{x} = (x, y)$:

$$\hat{\mathbf{M}}\mathbf{x} = \lambda\mathbf{x} \tag{3.5}$$

with the values $M_{11} = 1 - x_0^2$, $M_{12} = -1$, $M_{21} = \epsilon$ and $M_{22} = -\epsilon a$. The matrix $\hat{\mathbf{M}}$ has two eigenvalues. They read:

$$\lambda_{1,2} = \frac{1 - 3x_0^2 - \epsilon a}{2} \pm \sqrt{\frac{(1 - 3x_0^2 - \epsilon a)^2}{4} - \epsilon - \epsilon a(1 - x_0^2)} \tag{3.6}$$

The eigenvalues determine the stability of the fixed point. They are generally complex. They depend on all three parameters $\epsilon$, $a$, and (via $x_0$) $b$. If the real parts of both of them $Re(\lambda_{1,2})$ are negative the fixed point is stable. If at least one real part is positive the fixed point is unstable.

Depending on the number of fixed points and on their stability the dynamics of the system changes dramatically. fig. 3.2 shows different dynamical regimes that

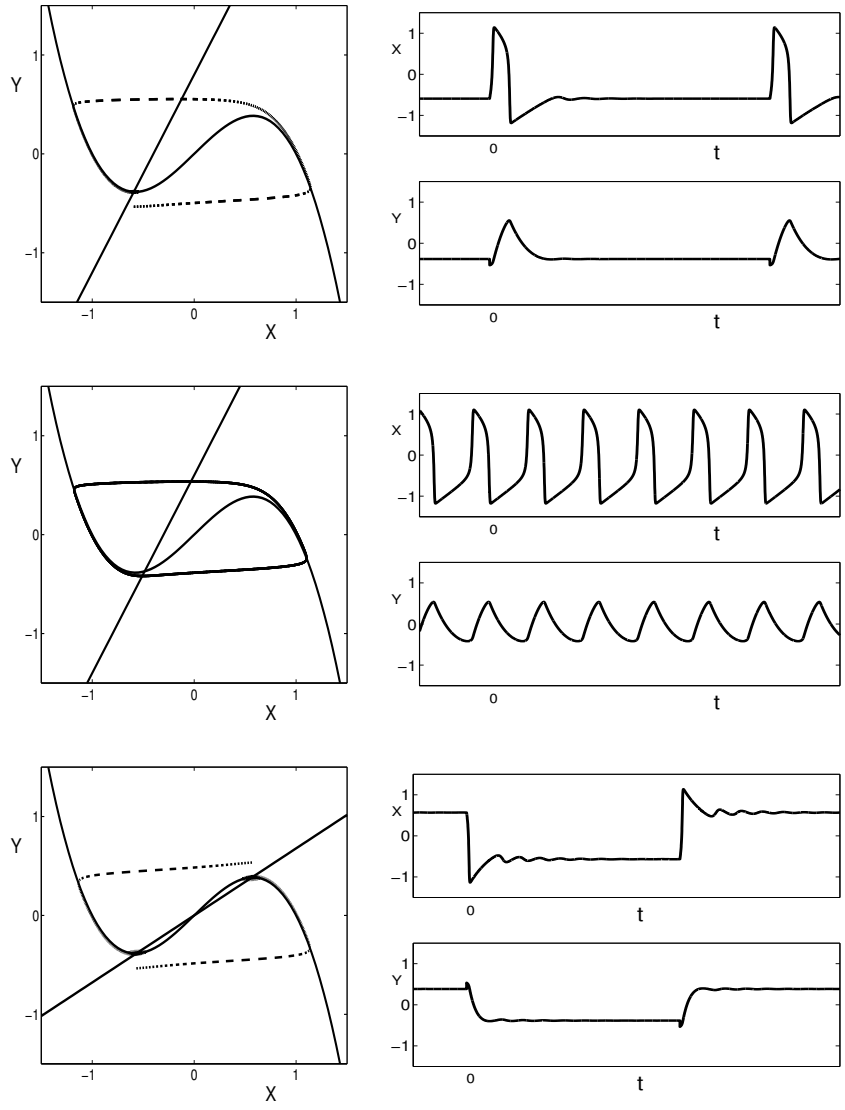


Figure 3.2: Depending on the parameters the FHN can either exhibit excitable (upper row; $a = 0.5$, $b = 0.4$), oscillatory (middle row; $a = 0.5$, $b = 0.3$) or bistable (lower row; $a = 1.475$, $b = 0.0$) kinetics. $\epsilon = 0.05$.

will be important in the present work:

In the case of excitable dynamics (upper panel) there exists only one fixed point which is located on one of the outer branches of the activator nullcline. This fixed point is stable. Small (subthreshold) perturbations decay. Perturbations exceeding a certain threshold (superthreshold) lead to a large excursion in phase space until the steady state is asymptotically approached again. The corresponding timeseries of the dynamical variables show large variations during small time intervals. They resemble action potentials observed in real neurons. In the following we will call these variations *spikes*. It is important to note that for a short time just after a spike is initiated the system cannot be excited again. This time is called the refractory time. It is to a good approximation independent of the form and magnitude of the perturbation.

In the case of oscillatory dynamics (middle panel) there is also only one fixed point but the real parts of the eigenvalues are no longer both positive. The fixed point is no longer stable and the system is attracted by a stable limit cycle instead. The timeseries of the system show nonintermittent oscillations. Small perturbations have little effect on the dynamics.

In the case of bistable dynamics (lower panel) there exist three fixed points two of which are stable. Once the system sits in one of the stable fixed points it can be perturbed beyond a threshold just as in the excitable case. It again performs a large excursion in phase space but does not return to the first steady state, but to the second. Another large perturbation is needed for the system to return to the initial point. To which of the fixed points the system is initially attracted depends on the initial conditions. The region in phase space from which a system is attracted to one of them is called its *basin of attraction*. Thus, in the scenario we have plotted in the lower panel of fig. 3.2 the perturbation from the first steady state brings the system into the basin of attraction of the other one. It is therefore not only the magnitude but also the *direction* of the perturbation that determines whether a perturbation grows or decays.

It is also the imaginary part of the eigenvalues 3.6 that has an influence on the dynamics. Fig. 3.3 shows that the stable fixed point in the excitable parameter regime (and also the two in the bistable regime) can be either a node (left panel) or a focus (right panel). As has been shown in [12] this has implications even on extended excitable media. The frequency with which the system spirals into the steady state (for a focus) is given by $\omega = \epsilon + \epsilon a(1 - x_0^2)$. We will see reminiscences of this behavior in chapter 5.

Important for the abruptness in the change of the activator $x$ compared to that of the inhibitor that we see during a spike is the so-called *separation of the timescales*. It is due to the smallness of the parameter $\epsilon$. The equations are said to be *stiff*. The activator evolves much faster than the inhibitor. This can be

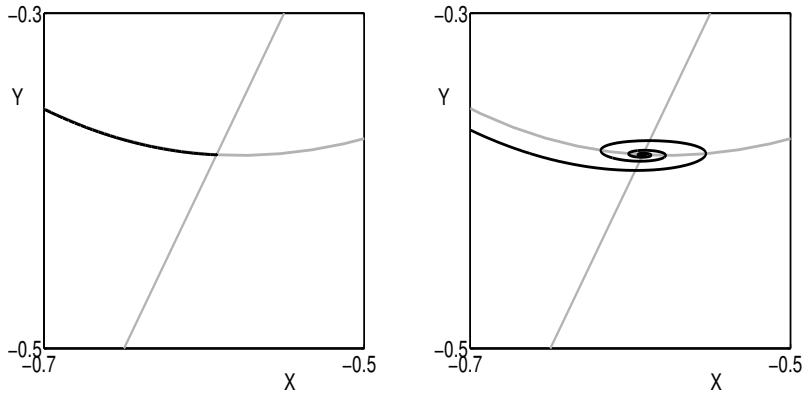


Figure 3.3: Real (left) and complex (right) eigenvalue in the excitable parameter regime. The stable fixed point becomes either a node (left) or a focus (right). The light gray lines show the nullclines, the black line a typical trajectory. $\epsilon = 0.05$ (left), 0.001 (right); $a = 0.5$, $b = 0.4$

observed in fig. 3.2 where the length of the dashes shows the speed of the system in phase space. Each dash represents the evolution during an equal time interval. Throughout this work we will assume $\epsilon \ll 1$.

As the two upper panels in fig. 3.2 suggest, the transition from the excitable to the oscillatory parameter regime can be established via a change of the parameter $b$. The bifurcation that the system undergoes is an Andronov-Hopf bifurcation or shorter just Hopf bifurcation. In the limit of a large timescale separation ($\epsilon \to 0$) it occurs when the intersection of the linear and the cubic nullcline move from an outer to the middle branch. For finite $\epsilon$ it occurs for intersections a little further outwards (higher absolute values of $x$). The critical value $\epsilon_c$ is given by:

$$\epsilon_c = \frac{1 - 3x_0^2}{a} \tag{3.7}$$

According to [63] the type of bifurcation (sub- or supercritical) cannot be determined in general, but for a particular parameter set. If the bifurcation is subcritical the amplitude of the stable oscillations is not a smooth function of the control parameter (otherwise it is). We will encounter this parameter range in chapter 6. It is then that a stable fixed point coexists with a stable limit cycle. An example for an excitable system is shown in [2]. We present an example of the bistable case in fig. 6.8. A perturbation from the stable fixed point can then lead to continuing oscillations. In this case one usually talks about a *hard excitation*.

In the parameter region we are interested in, the amplitude of the oscillations grows very quickly but smoothly from small oscillations around the fixed point

to spikes. This is shown in fig. 3.4. In the plot we show the amplitude of the

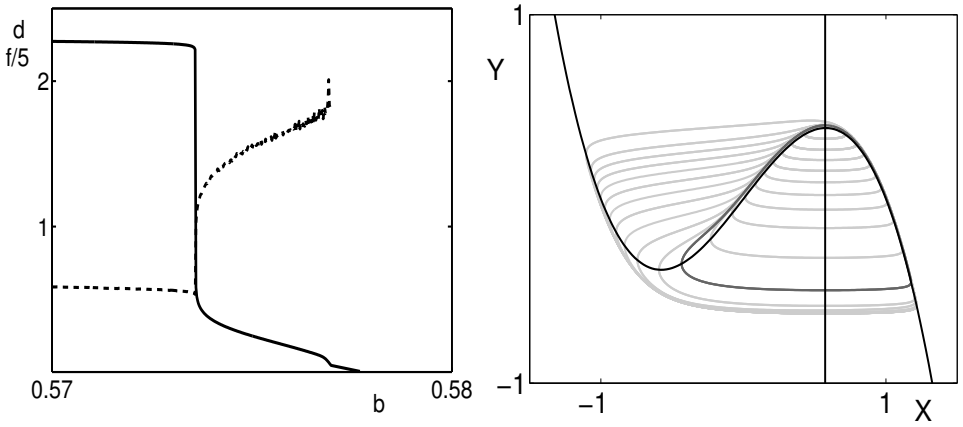


Figure 3.4: Canard explosion. Left panel: The amplitude $d$ of the oscillations grows very quickly but smoothly over a small parameter range. We have defined the amplitude $d$ as the difference between the maximum value of $x$ in a timeseries (longer than the period) and the minimum. The solid gray line plots the amplitude, the dashed black line plots one fifth (in order to see better) of the frequency of the oscillations. Right panel: Phase portrait for $c = c_0$ (dark gray) and $c = c_0 \pm 10^{n-12}$, $n = 1 \ldots 11$ (light gray). Higher values of $c$ produce smaller loops, lower values larger loops. The black lines are the cubic and the linear nullcline in the case $c = c_0$. Parameters: $b = 0.0$, $\epsilon = 0.05$. $c_0 = 0.57359225732$.

oscillations versus the parameter $b$. In order to define this amplitude we first define $x_{max}$ as the maximum value of a timeseries of $x$ (after some transient time; the timeseries is several periods long) and $x_{min}$ accordingly. The amplitude of the oscillations is then the difference between them:

$$d = x_{max} - x_{min} \tag{3.8}$$

The sudden increase of the amplitude is accompanied by a rapid decrease of the frequency. This is also shown in fig. 3.4. The small amplitude oscillations have a significantly smaller periodic time than the spikes. The width of the region where the amplitude increases and frequency decreases strongly depends on the timescale separation which is governed by the parameter $\epsilon$. In the limit $\epsilon \to 0$ is also goes to zero.

In the figure we also see the phase portraits of systems close to the sudden increase of the amplitude. We see that the trajectories follow the repelling slow manifold (middle branch of the cubic nullcline) for a considerable amount of time.

The phenomenon is known as *Canard explosion*. The observed changes are smooth. The Canard explosion is not a bifurcation. It has been observed experimentally in [79]. The authors used the FHN system for corresponding simulations. In recent works [74, 110, 124] a variety of new phenomena was found in this parameter region. We will find new such phenomena in chapter 5.

In various fields of natural sciences the FHN has been considered not only for a single system but also for an ensemble of coupled systems. We will do so in chapter 5 where the individual systems are coupled globally (eq. 5.1) and in chapter 6 where we the coupled system has a spatial structure (eq. 6.6). Although the term FitzHugh–Nagumo has been coined for zero-dimensional systems we will extend it to the aforementioned systems.

As discussed in chapter 1 the dynamics of neurons is subject to many rapidly varying influences that cannot be described deterministically. This holds for many other (not only) excitable systems as well. It is therefore a common way to include random fluctuations in the modeling of neurons [119]. The problem of how to include fluctuations into the FHN model is a difficult one. For deterministic signals the method is rather clear. It was already FitzHugh in his original work who added a stimulus parameter to the activator dynamics. For neurons this seems obvious because a signal is usually applied in terms of an electrical stimulus (e.g. from other neurons). Since we have advertised the FHN model as a standard model for excitable systems we must add here that this may change depending on the actual system under consideration for deterministic as well as for stochastic signals. Different qualitative behavior for different cases have been reported in [29, 104].

The most common approach in literature to account for fluctuations is to apply additive Gaussian white noise to eq. 3.1. The question of whether to apply it to the activator $x$ [25, 109] or the inhibitor $y$ [87, 130] or both [29, 118] is not yet satisfactorily answered. In [29] qualitatively different behavior was reported for the different cases. There are good biological justifications for each way (Compare also chapter 1.): The input from the surrounding neurons that acts on the inhibitor is highly fluctuating. On the other hand the opening and closing of the ion channels in the nerve cell membrane that lead to the inhibition are also fluctuating. There are many more sources of fluctuations that are discussed for example in [40].

Last but not least we want to mention the following fact: Suppose that we put an additive Gaussian white noise source $\xi(t)$ into the inhibitor dynamics and consider the following Langevin equation:

$$\begin{aligned} \dot{x} &= x - x^3 - y \\ \dot{y} &= \epsilon\,(x - ay - b) + \xi(t) \end{aligned} \tag{3.9}$$

If we do a variable transformation $y = z - \eta(t)$ this system is equivalent to one in

which the noise is in the activator instead:

$$\begin{aligned} \dot{x} &= x - x^3 - z + \eta(t) \\ \dot{z} &= \epsilon\,(x - az - b) \end{aligned} \tag{3.10}$$

where the noise is now not Gaussian white anymore but has temporal correlations. The variable $\eta(t)$ constitutes an Ornstein-Uhlenbeck process:

$$\dot{\eta}(t) = -\eta(t) - \xi(t) \tag{3.11}$$

The Ornstein-Uhlenbeck process generates colored noise. The spectral power at high frequencies is damped out like $\frac{1}{\omega^2}$. In the case of neurons the physiological meaning of this would be that there exists some kind of bandpass filter in the synapses. For this filter there exists no experimental evidence.

In the following sections we will investigate situations with noise in the activator and also cases with noise in the inhibitor dynamics.

## 3.2 Coherence Resonance

Together with stochastic resonance [67, 71] coherence resonance belongs to the most popular representatives of situations where noise induces - against intuition - order into systems. In this case the coherence of the oscillatory output of a nonlinear system (see fig. 3.5) takes on a maximum value for a certain finite


Figure 3.5: *Beneficial* role of noise: Fluctuations of a finite nonzero intensity lead to an optimally coherent output.

nonzero intensity of applied fluctuations.

The term coherence resonance was first introduced by Pikovsky and Kurths [95]. Other names for the phenomenon (*stochastic resonance without external periodic force* [37], *internal stochastic resonance* [86]) have not been so widely accepted.

In order to understand the mechanism behind the effect let us consider the stochastic FHN system in the excitable parameter regime near the bifurcation to the oscillatory state. The main effects of the noise term are the following:

A system far from the fixed point which moves along the deterministic trajectory (fig. 3.2) in the noiseless case deviates from this trajectory if noise is applied. If the noise intensity is small, so will be the deviations.

The second effect comes into play when the system approaches the fixed point. In the deterministic case the approach will be asymptotic and will take an infinite amount of time. In the noisy case the system approaches the fixed point, moves randomly around it, and due to this stochastic motion occasionally crosses the excitation threshold. A new spike is generated. In this context one often talks about *noisy precursors* of the bifurcations [86].

Now let us look at numerical simulations of system 3.13 with Gaussian white noise in the activator only. Fig 3.6 shows the resulting timeseries for different noise intensities. For low intensities the spikes are very rare. The system sits close to the fixed point most of the time. Since the noise is Gaussian, spikes will occur for any intensity after a very long time. This time goes to infinity as the intensity goes to zero, though. For increasing noise intensities spikes start to occur almost regularly. For even higher intensities they become less regular again.

Let us now look at a typical such spike train in detail (fig. 3.7). Let us call the interspike interval (ISI), i.e. the time between two successive spikes, $\tau$. It is useful to split this time into two separate ones namely into an activation time $\tau_a$ and an excursion time $\tau_e$: $\tau = \tau_a + \tau_e$. This splitting is useful because the activation and the excursion time are affected differently by the fluctuations. It takes a large noise intensity to affect a system that has just been excited during its excursion along the excitation loop. The effect of increasing noise on the activation time is much more drastic. It decreases rapidly with increasing noise. If there is no noise the system will never be excited and the activation time goes to infinity. The most coherent output is observed when the system is reexcited almost instantly whenever it returns to the fixed point but is hardly affected during an excitation. In the limit of large noise intensities the fluctuations govern the dynamics at all times.

The probably most common measure for coherence resonance is the ratio of the standard deviation of the ISI and its mean $\langle\tau\rangle = \lim_{N\to\infty} \frac{1}{N} \sum_{i=1}^{N} \tau_i$ which is known as the coefficient of variation:

$$R = \frac{\sqrt{\langle\tau^2\rangle - \langle\tau\rangle^2}}{\langle\tau\rangle} \tag{3.12}$$

For a constant rate of events, i.e. for a Poisson process, the standard deviation equals the mean and $R$ is one. For zero standard deviation, i.e. for a perfectly periodic process, it becomes zero.

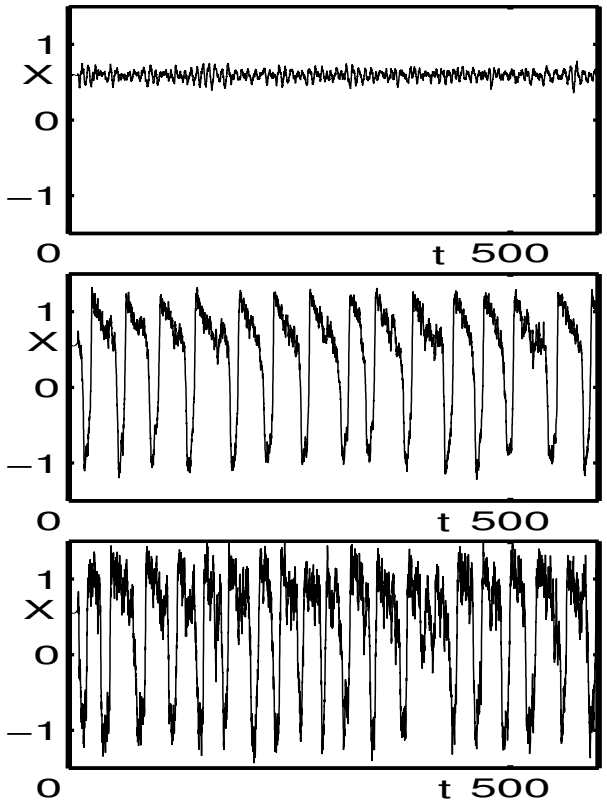


Figure 3.6: Timeseries of the noisy FHN for different noise intensities: With low noise intensity the spikes are very rare. The system stays at the steady state for most of the time (upper row) . For higher intensities regular spiking occurs (middle row). For even higher intensities it becomes more irregular again (lower row).

In the FHN system $R$ goes from 1 through a minimum and increases above 1 for high noise intensities [70]. We show in fig. 3.8 the coefficient of variation for different values of the timescale separation. For decreasing $\epsilon$, i.e. with better separation of the timescales, the minimum of $R$ gets slightly more pronounced and is shifted towards lower values of the noise intensity.

Coherence resonance was found experimentally in human tactile sensation experiments [26]. A similar effect has been found for extended systems [87, 94].

## 3.3 Probability Distribution

As mentioned above we will in this section investigate the influence of additive noise applied on both the activator and the inhibitor variable of the FHN system [64].

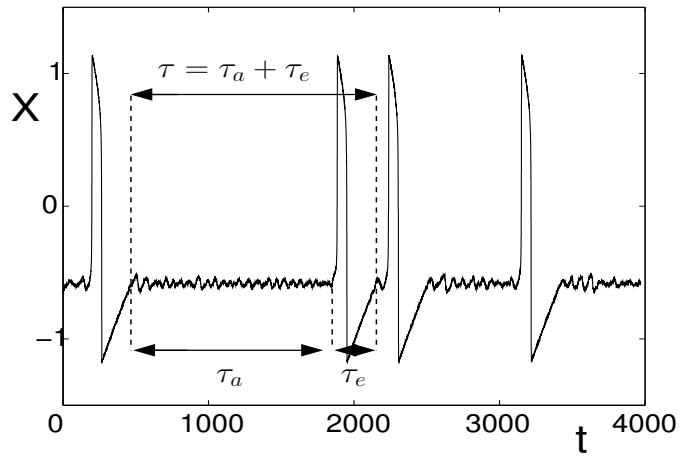


Figure 3.7: Noise evokes a new timescale: the mean activation time. It is much more noise intensity-dependent than the mean excursion time.

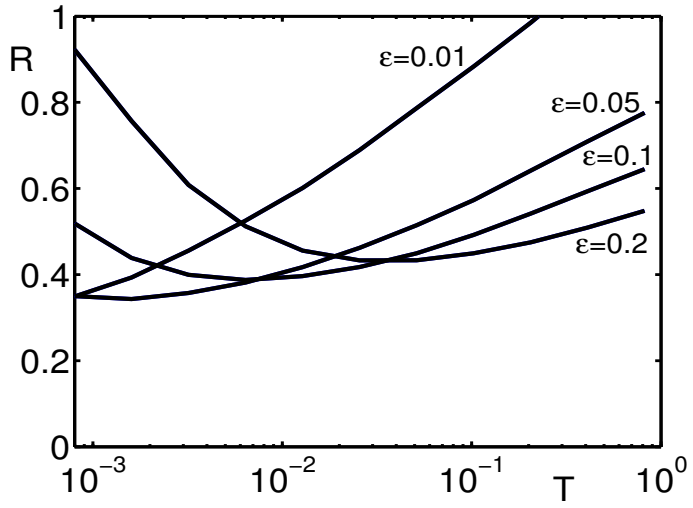


Figure 3.8: Coefficient of variation $R$ for different values of timescale separation in the FitzHugh–Nagumo system. There exists a minimum in R, i.e. a maximally coherent output, for a finite noise intensity. Parameters: $a = 0.5$, $b = 0.44$; $\epsilon$-values are given close to the corresponding lines.

The Langevin equations have the following form:

$$\begin{aligned} \frac{\partial x}{\partial t} &= \frac{1}{\epsilon}\left(x - x^3 - y\right) + \xi_x(t) \;=\; f_x(x,y) + \xi_x(t) \\ \frac{\partial y}{\partial t} &= \gamma x - y + b + \xi_y(t) = f_y(x,y) + \xi_y(t) \end{aligned} \tag{3.13}$$

where $\xi(t)$ is Gaussian white noise with $\langle \xi(t) \rangle = 0$ and $\langle \xi_i(t_1)\xi_j(t_2) \rangle = 2T_i\delta_{i,j}\delta(t_1 - t_2)$ $(i, j = x, y)$. The equations 3.13 differ somewhat from the FHN equations we showed in the previous section. By the variable transformation $t \to \frac{t}{\epsilon}$, $\epsilon \to \frac{\epsilon}{\gamma}$, $b \to \frac{b}{\gamma}$, and $T_y \to T_y \frac{\epsilon}{\gamma}$ they can be transformed into one another.

The system 3.13 can equivalently be described in terms of the following two-dimensional Fokker–Planck equation (FPE):

$$\begin{aligned} \frac{\partial}{\partial t}P(x,y,t) \;=\; & -\frac{\partial}{\partial x}\frac{1}{\epsilon}\Big(x - x^3 - y\Big)P(x,y,t) \;-\; \frac{\partial}{\partial y}\Big(\gamma x - y + b\Big)P(x,y,t) \\ & + T_x \frac{\partial^2}{\partial x^2}\,P(x,y,t) \;+\; T_y \frac{\partial^2}{\partial y^2}P(x,y,t). \end{aligned} \tag{3.14}$$

We are interested in the stationary solutions of this equation.

$$\frac{\partial}{\partial t}P_0(x,y) = 0 \tag{3.15}$$

Eq. 3.14 is a linear FPE. The system described by this equation is ergodic. It has a unique stationary solution which is globally attracting. The forces cannot be derived from a potential. The probability flux will therefore not vanish in the stationary solution. An exception to this is when $\partial_x f_y = \partial_y f_x$ holds. The forces then posses a potential. The stationary solution to the FPE 3.14 is then Boltzmann-like :$P_0(x,y) \sim exp[\frac{-1}{T}\int_{(0,0)}^{(x,y)} \mathbf{f}(x',y')d\mathbf{s}']$ with the noise intensity $T$ in the $x$- and $y$-dynamics [43]. It holds $\epsilon\gamma = -1$ and the potential has one or two minima. We find a two-dimensional mono- or bistable system for this particular situation. Fixed points have real eigenvalues, only. The net flux then vanishes: $J(x,y) \equiv 0$.

This flux-free solution has been extended to a situation with four correlated noise sources [54]. Their intensities obey a generalized potential condition in dependence on the parameters of the deterministic model.

In general an analytic solution for the stationary probability distribution cannot be obtained. Thus numerical solutions are needed. We show here results of simulations of eq. 3.14. Throughout the section we use a parameter set for which the system exhibits excitability.

We applied different numerical techniques. For the cases with noise in the inhibitor variable we used a finite elements method [65]. The minimal resolution for all cases was kept between 100 and 200 in each direction. The results for the activator noise were obtained using finite difference methods. In this case the full system 3.14, i.e. the time-dependent problem, was simulated until the system relaxed into the stationary state and the probability distribution did (almost) not change anymore. The exact criterion was that the absolute value of the probability difference between a point at a given time and the same point at $t = 1$ later summed up over the whole grid was less than $10^{-10}$. These simulations were tested with

several algorithms: Euler, 5–th order Runge-Kutta and a semi-implicit method based on the Crank-Nicholson scheme [97]. They all performed similarly well.

We start with a situation where the noise in the activator variable $x$ is set to zero: $T_x = 0$. The remaining parameters are: $\epsilon = 0.1$, $a = 2.0$, $b = 1.4$. $T_y$ will be varied. With respect to the nullclines of the system we could now look at the situation as if the cubic nullcline were shifted up and down randomly.

For the deterministic case ($T_y = 0$) the stationary probability distribution forms a delta peak at the fixed point. The behavior for increasing intensities is shown in fig. 3.9. If a small amount of noise is added, the system starts moving randomly around the fixed point. It very rarely crosses the excitation threshold and spikes. This situation corresponds to a Poissonian spike train [95]. The probability distribution is peaked around the deterministic steady state ($T = 0.01$ in fig. 3.9). In fig. 3.9 we can see only one maximum.

It should be noted here that for low noise intensities the density decays so quickly that the numerical accuracy may well be too low to observe reasonable results further away from the steady state.

For increasing noise intensity two saddle points together with a minimum in between them become visible in the density plot ($T = 0.1$ in fig. 3.9). A crater-like structure emerges. Even with the moderate timescale separation of $\epsilon = 0.1$ the probability density is clearly concentrated over the outer branches of the cubic nullcline. This corresponds to a circular motion of the system. It is in this parameter region that coherence resonance occurs. The system follows the deterministic trajectory of a spike, which was shown in the upper panel of fig. 3.2, quite closely. The transitions from one outer branch to the other happen at distinct values of the inhibitor. On the other hand it is also excited quickly after returning to the fixed point which is expressed by the high probability density on the deterministic excursion loop.

For further increasing noise intensity the minimum of the probability density vanishes ($T = 0.46$, $T = 1.0$ in fig. 3.9). The influence of the noise on the system during its excitation loop now becomes prominent. The transition between the two peaks of the distribution take place at a broad range of inhibitor values centered with maximal probability at $y = 0$.

When we vary the parameter $\epsilon$ that governs the separation of the timescales we find a qualitatively similar behavior. The results are shown in fig. 3.10. The value of $\epsilon$ does not affect the position nor the shape of the system's nullclines. The remaining parameters are fixed to $\gamma = 2.0$, $b = 1.4$, and $T_y = 0.1$. They are chosen such that for small $\epsilon$ values the deterministic system is close to the oscillatory regime (cf. fig. 3.2), i.e. it has a small excitation threshold.

For small values of $\epsilon$ the distribution again consists of a crater-like structure ($\epsilon = 0.01$, in fig. 3.10) just like the one we observed for intermediate noise intensity

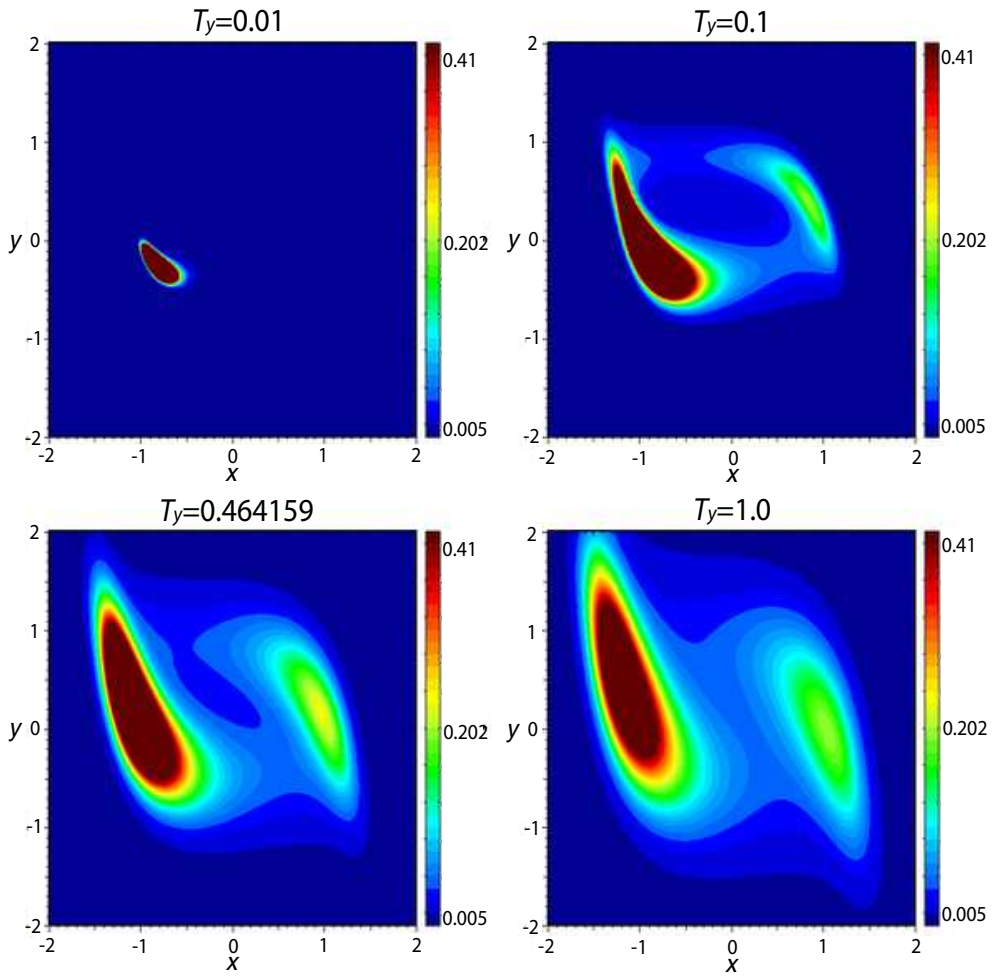


Figure 3.9: Stationary probability distributions for $b = 1.4$, $\epsilon = 0.1$, and $\gamma = 2$. The inhibitor noise intensity is varied. It is given above the individual panels. Note the qualitative topological change. At first we can observe one maximum, only. For increasing noise it broadens. We see two maxima, two saddle points and one minimum. For even higher intensities the minimum and one saddle point vanish again.

in the last figure (fig. 3.9). The density is located above the deterministic spike trajectory even more narrowly than before. The maxima on the outer branches of the cubic nullcline are pronounced. This is due to the large timescale separation. The system moves much slower along these outer branches than during a transition from one branch to the other (which is done for an almost constant value of the slow inhibitor $y$). This is again the region where coherence resonance occurs. The

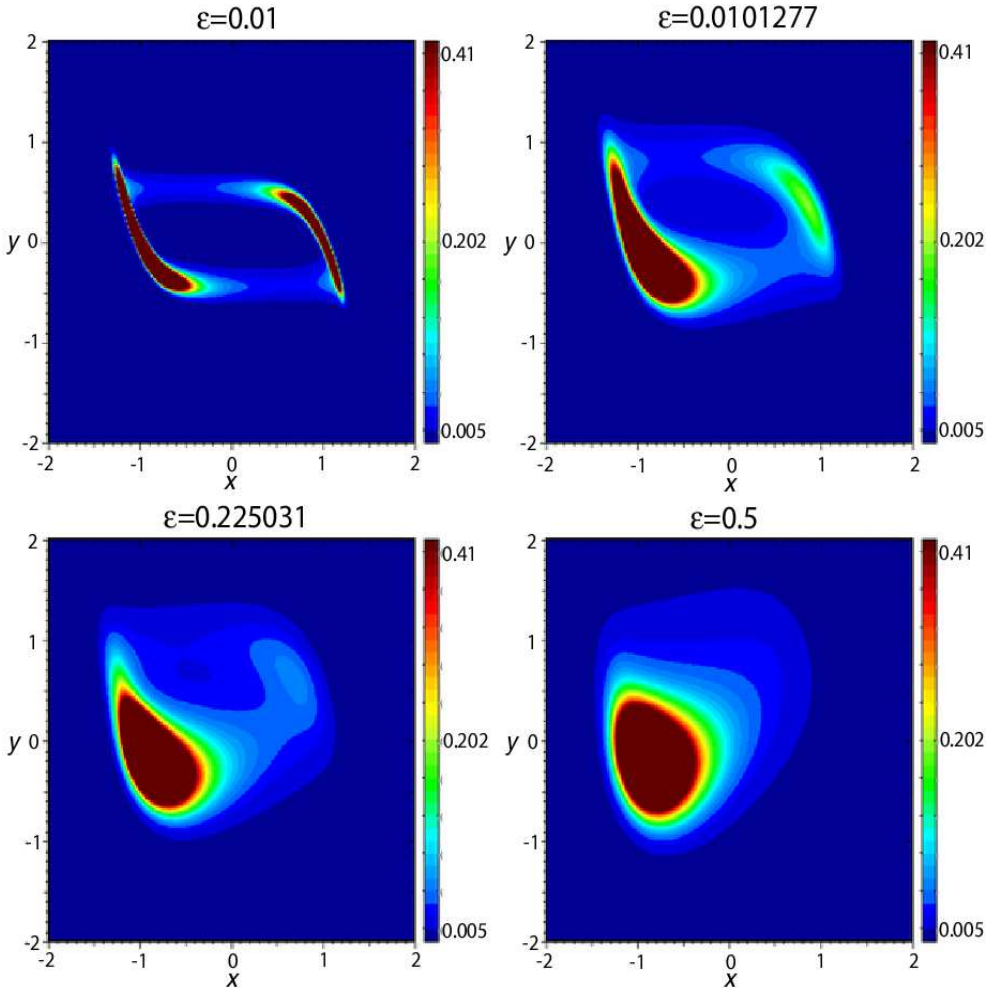


Figure 3.10: Stationary probability distributions for $b = 1.4$, $T_y = 0.1$, and $\gamma = 2$. The inhibitor noise intensity is varied. It is given above the individual panels. Note the qualitative topological change. At first we can observe one maximum, only. For increasing noise it broadens. We see two maxima, two saddle points and one minimum. For even higher intensities the minimum and one saddle point vanish again.

spike trains of $x(t)$ are almost periodic.

For increasing $\epsilon$, i.e. for a smaller timescale separation, the peak in the probability distribution near the deterministic fixed point grows at the expense of the second peak ($\epsilon = 0.23$ in fig. 3.10).

For large $\epsilon$ we see a new behavior ($\epsilon = 0.5$, in fig. 3.10). The saddle-points, the minimum, and one maximum vanish and only one maximum remain. This peak

is shifted from the deterministic fixed point towards higher $x$-values and it is very outspread. Here, the coherence of the oscillations of $x(t)$ has vanished.

We have also studied the case where the noise does not act on the inhibitor variable $y$ but on the activator variable $x$, i.e. $T_y = 0$ and $T_x \neq 0$ in eq. 3.13. We have scanned the plane of the timescale-separation $\epsilon$ and the weighted diffusion constant $\hat{T}_x = \epsilon T_x$. We find qualitatively different stationary probability distributions as shown in fig. 3.11

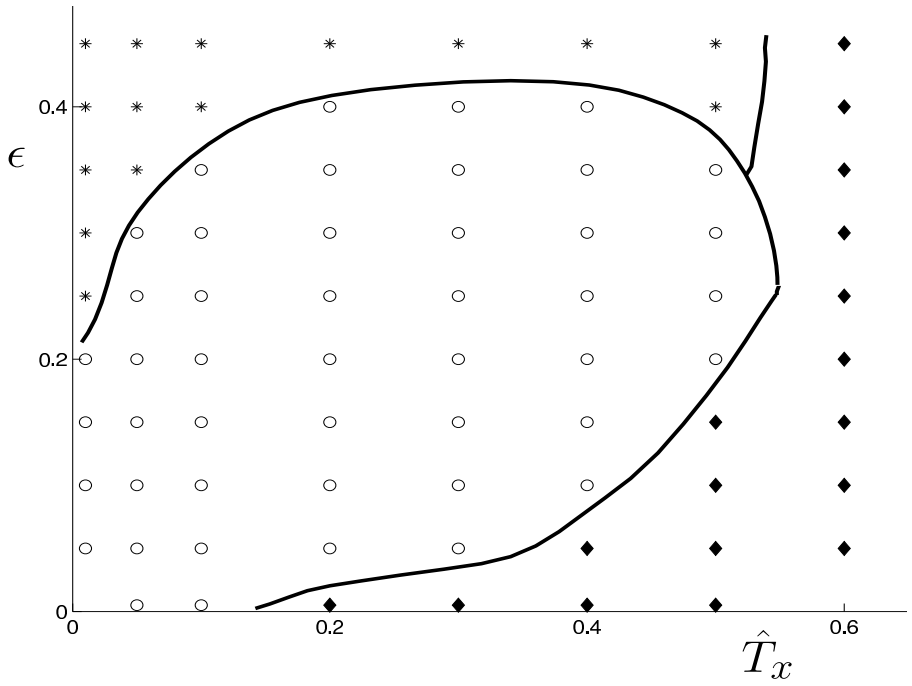


Figure 3.11: Scan of the plane of the timescale-separation $\epsilon$ and the weighted noise intensity $\hat{T}_x = \epsilon T_x$: We find qualitatively different stationary probability distributions. Empty circles ($\circ$) denote parameter sets where minima of the stationary probability occur. At black diamonds we find two maxima and at asterisks ($*$) one maximum, only. The black lines are drawn to guide the eye.

We distinguish three different regions: In the first region we find one maximum, only. It is located at low noise intensities and high $\epsilon$ values. The corresponding points are marked with an asterisk in fig. 3.11. We have computed a contour plot of the probability density for a typical example. It can be seen in fig. 3.12(a).

In the second region we find a crater-like structure of the probability density consisting of two maxima, one minimum, and two saddle points. This region is limited at high $\epsilon$ and high $\hat{T}$ values. The corresponding contour plot can be seen

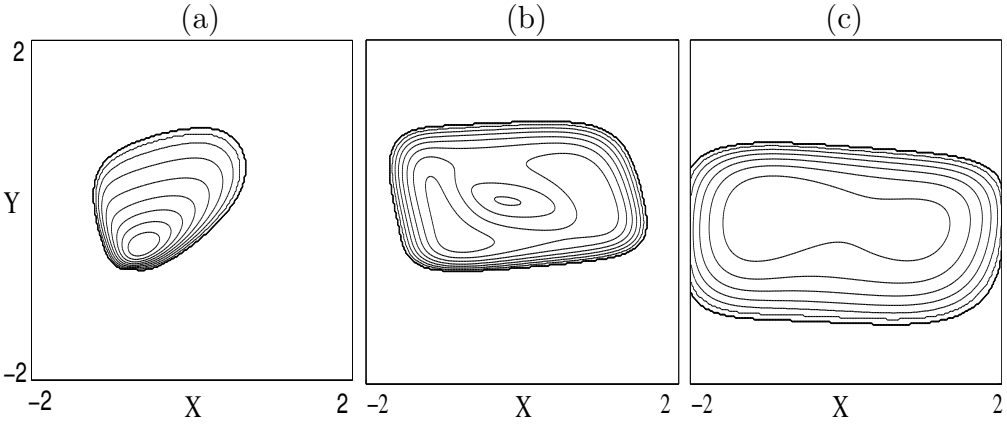


Figure 3.12: Contour plots of typical examples of the different density plots as distinguished in fig. 3.11. We find either a single maximum ((a); $*$ in fig. 3.11) or two maxima, a minimum, and two saddle points ((b); $\circ$ in fig. 3.11) or two maxima and one saddle point ((c); black diamonds in fig. 3.11). Parameters: $\gamma = 2$, $b = 0.8$ (all); $\gamma = 2$, $b = 0.8$. Parameters: $\epsilon = 0.35$, $T_x = 0.01$ (a); $\epsilon = 0.05$, $T_x = 0.1$ (b); $\epsilon = 0.05$, $T_x = 0.6$ (c).

in fig. 3.12(b). This is the region of coherence resonance. We show here that this region extends to larger $\epsilon$ values than considered in [70].

In the third region we find two maxima and one saddle as shown in the contour plot in fig. 3.12(c). It is located at small $\epsilon$ values and high noise intensities. The corresponding systems do not follow the deterministic trajectory of the excited deterministic system any more.

## 3.4 Probability Flux

In this section we study the probability flux of the stationary solutions. We will present the flux fields and compare them to the original force fields of the deterministic system. The simulations in this section are again done without activator noise ($T_x = 0$) and the finite elements method is used.

From $\frac{\partial P}{\partial t} = -\Delta \mathbf{J}$ we find the two components of the probability flux in accordance with eq. 3.14:

$$\begin{aligned} J_x(x,y) &= v_x\, P(x,y) = \frac{1}{\epsilon}\left(x - x^3 - y\right)\, P(x,y) \\ J_y(x,y) &= v_y\, P(x,y) = (\gamma\, x - y + b)\, P(x,y) - T_y \frac{\partial}{\partial y}\, P(x,y) \end{aligned} \tag{3.16}$$

For the stationary case we see at once that the divergence of the probability flux is zero, $\nabla \mathbf{J} = 0$. This does in this case obviously not imply that the flux is constant in space or vanishes like in systems with one degree of freedom.

The flux $\mathbf{J}$ is conservative, incompressible and cannot contain sinks and sources. It contains closed loops, only. The only possible singularities are centers and saddles. This is a difference to the deterministic force field which, as we showed in section 3.1, contains - depending on the parameters - foci or nodes.

Still, if the diffusion constant is small, one could expect that the topology of the deterministic flux and of the probability flux behave similarly.

The nullclines of the probability flux are readily computed:

$$y = (x - x^3) \tag{3.17a}$$

$$y = (\gamma x + b) - \frac{T_y}{P}\frac{\partial P}{\partial y} \tag{3.17b}$$

Results of the numerical simulation of such a vector flux field together with the corresponding probability distribution are shown in fig. 3.13.

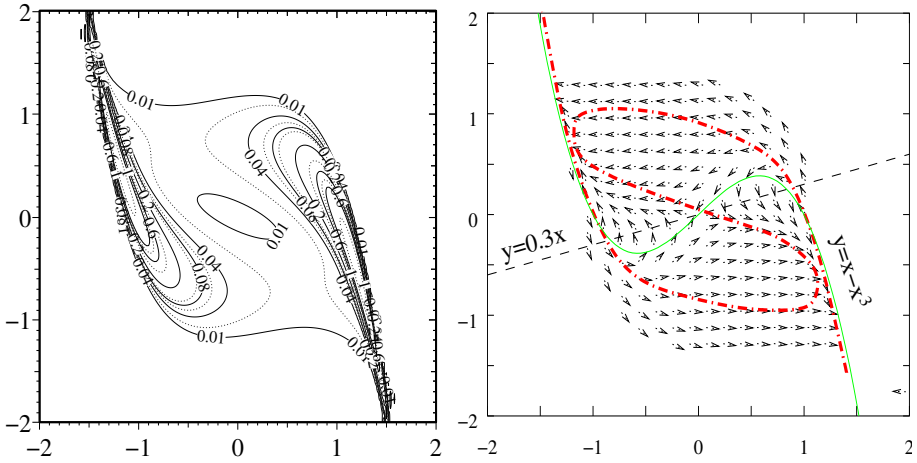


Figure 3.13: Stationary distribution (left) and flux (right) of the probability density. The dashed black and the solid light line represent the nullclines of the deterministic system and the dashed light line shows the $y$-nullcline of the probability flux $J_y$. The system is in the bistable parameter regime. Parameters: $b = 0$, $\gamma = 0.3$, $\epsilon = 10^{-1}$, and $T_y = 0.5$.

The parameter set corresponding to the example is in the bistable parameter region. The direction of the flux is indicated by the little arrows. In regions where there are no such arrows the probability density and also the flux becomes extremely small and the numerical error correspondingly large.

We also show the numerically obtained nullclines. Note that the analog to the cubic nullcline, given by eq. 3.17c(a), does not depend on the probability. It is always equal to the deterministic cubic nullcline. It is only the analog of the inhibitor nullcline that is affected by the noise. In fig. 3.13 we show the nullclines of the probability flux together with the nullclines of the deterministic dynamics. We see that the nullcline at which the $y$ component of the flux $J_y$ vanishes clearly deviates from the deterministic counterpart. An exception occurs at the fixed points of the deterministic system where the two almost coincide. Further away from the fixed points the nullclines exhibit a complicated behavior.

Now let us come back to the excitable parameter regime. We therefore fix the parameter to: $\epsilon = 0.1, \gamma = 2.0, b = 1.4$. The noise intensity $T_y$ will again be varied. The results we obtain qualitatively differ from one another. This is demonstrated in fig. 3.14. The plots for low noise intensity show that almost the whole flux is located near the deterministic fixed point. Here the intervals between two consecutive spikes in a spike train obey a Poissonian distribution. The system is excited very rarely. In the contour plot only one maximum is observable. It is located at the center of the flux. The second nullcline shows a complicated behavior. This may be due to large numerical errors that occur in regions where the probability density and the flux are extremely small.

For higher noise intensities the probability density at the right outer branch of the deterministic cubic nullcline quickly increases. This is the region of coherence resonance. We again find the crater-like structure in the probability density.

At a further increase of the noise intensity we see not only that the minimum of the probability distribution vanishes but we also observe a qualitative change in the nullclines of the probability flux, namely that they exhibit additional intersections. An additional center and a saddle point in the flux field can be found. The flux resembles the one observed in the bistable case 3.13.

## 3.5 Summary

We have numerically investigated the stationary probability distribution and the probability flux of the FitzHugh–Nagumo system with additive Gaussian white noise. The influence of noise on both, the activator and the inhibitor variable has been studied. We also varied the parameter $\epsilon$ which governs the separation of the timescales of the activator and the inhibitor. We have found differences in the topology of the stationary probability distribution. We distinguish three different cases. We either find a single maximum or two maxima and a saddle point or two maxima, one minimum, and two saddle points. The latter occurs where the system exhibits coherence resonance.

The flux of the probability also shows qualitative changes when varying the

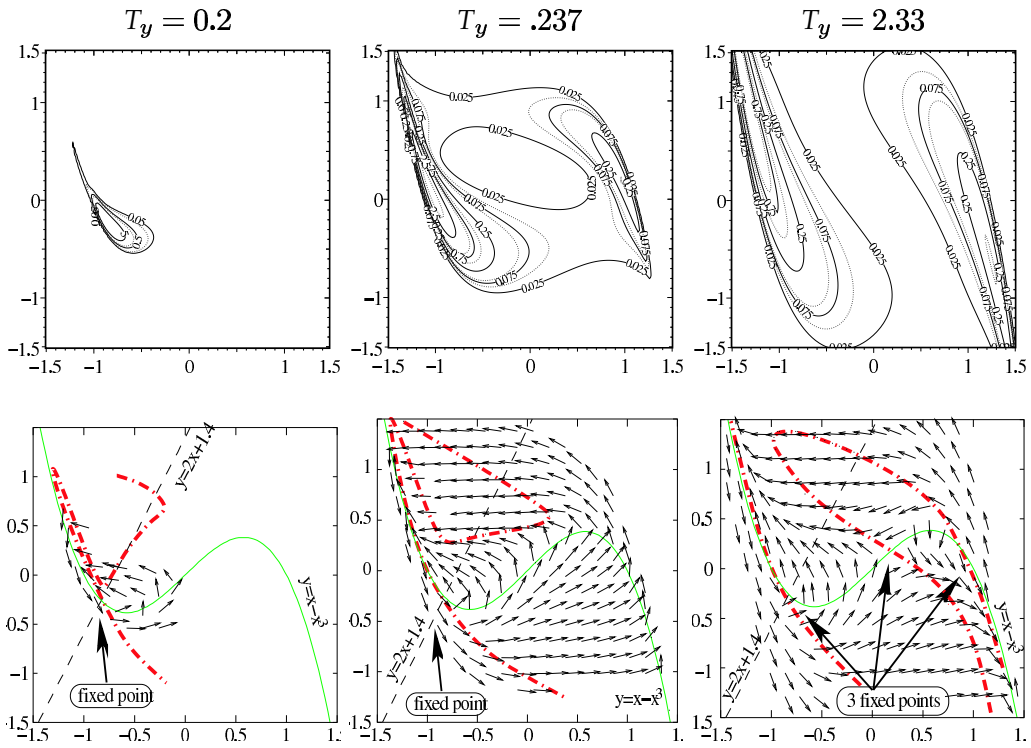


Figure 3.14: Probability distribution and flux of the probability density in the stationary case of eq. 3.14. The upper row shows contour plots of the probability density with the inhibitor noise intensity $T_y$ given above each column. The lower row shows the corresponding flux fields. The nullclines of the deterministic dynamics are depicted as dotted line (activator nullcline) and as dashed line (inhibitor nullcline). The inhibitor nullcline of the probability flux is marked by the dash-dotted line. Note that for high noise intensities the nullclines have additional intersections. The systems are in the excitable parameter regime. Parameters: $\gamma = 2.0$, $b = 1.4$ and $\epsilon = 0.1$.

noise intensity. For high intensities a saddle and a center emerge. This is accompanied by additional intersections of the nullclines of the flux.

The different combinations of singularities can be used to classify different dynamical regimes in such systems.

# Chapter 4

# Pure Noise-Induced Oscillations and Pure Noise-Induced Excitability

In this chapter we demonstrate how excitability can be generated by the interaction of fluctuations and coupling. The system we investigate does not have an excitable parameter regime by itself, i.e. without noise. It is the noise that creates this regime.

The parameter regime of noise-induced excitability is close (in parameter space) to a regime of noise-induced oscillations. The two regimes are separated by an Andronov-Hopf bifurcation.

We will start off with a simple model and gradually increase its complexity. In section 4.1 we reexamine a one-variable model that was originally introduced in [16]. For certain parameters this model exhibits for increasing noise intensity a transition from a monostable to a bistable state via a pitchfork bifurcation and back.

In section 4.2 we add a second dynamical variable to the dynamics and find that the transition from the monostable to the bistable state is replaced by a transition from a monostable to an oscillating state. As in the previous case there exists a reentrance into the monostable regime for increasing noise intensity.

By adding an additional parameter properly to the dynamics the system exhibits excitability. This is shown in section 4.3.

## 4.1 Pure Noise-Induced Pitchfork Bifurcation

Noise induced phase transitions are among the most popular examples proving that, counterintuitively, fluctuations are under certain circumstances able to create order. Many different variations of such transitions were introduced in literature [38]. Spatial patterns can be induced via noise-induced phase transitions [19, 92,

129]. Stochastic resonance has been demonstrated to occur in systems in a noise-induced phase [128]. Ratchet-like transport has been found to occur [98]. The influence of colored noise has been investigated [59, 77, 78]. First and second-order phase transitions have been found [84].

### 4.1.1 Exact Solution: Selfconsistent Equation

We start with what may be considered a standard model for the investigation of pure noise-induced phase transitions [16, 17]. It describes an ensemble of $N$ statistically identical units that are coupled to each other via their average. The individual units are subject to independent multiplicative noise. The original form reads:

$$\dot{x_i} = f(x_i) - \frac{K}{N}\sum_{j=1}^{N}(x_i - x_j) + g(x_i)\xi_i(t), \qquad i = 1 \ldots N \tag{4.1}$$

where the noise term $\xi(t)$ is Gaussian and white with mean and correlations given by:

$$\langle \xi_i(t) \rangle = 0, \qquad \langle \xi_i(t)\xi_j(t') \rangle = 2T\delta_{ij}\delta(t - t') \tag{4.2}$$

Eq. 4.1 is interpreted in the Stratonovich sense.

The nonlinear functions $f$ and $g$ are determined by the following polynomials:

$$\begin{aligned} f(x) &= -x(1 + x^2)^2 \\ g(x) &= 1 + x^2 \end{aligned} \tag{4.3}$$

For sufficiently high coupling strength the system undergoes (in the limit $N \to \infty$) a phase transition for increasing noise intensity: It starts with a phase with vanishing mean ($\langle x \rangle = 0$), then enters a phase where the mean takes one of two finite nonzero values ($\langle x \rangle \neq 0$) which are symmetrically centered around zero, and then reenters into the first phase ($\langle x \rangle = 0$). In the following we will call the phase with $\langle x \rangle = 0$ the *disordered* and that with $\langle x \rangle \neq 0$ the *ordered* phase. Since the ordered phase does not exist in the absence of noise the phenomenon is called a *pure* noise-induced phase transition.

In previous works often a self-consistent approach was used to investigate the bifurcation diagram. The method consists of the following steps: Eq. 4.1 is replaced by:

$$\dot{x} = f(x) - K(x - \langle x \rangle) + g(x)\xi(t) \tag{4.4}$$

where $\langle x \rangle$ is determined by the equation

$$\langle x \rangle = \int_{-\infty}^{\infty} xP(x, \langle x \rangle) \tag{4.5}$$

using a stationary state probability $P(x, \langle x \rangle)$ which we assume to be uniquely determined for a given $\langle x \rangle$ by the corresponding Fokker–Planck equation. It reads:

$$\begin{aligned} P(x, \langle x \rangle) &= \frac{1}{Z} \frac{1}{1+x^2} \\ & \quad e^{-\frac{x^2}{2T} + \frac{K}{2T(1+x^2)} + \frac{K\langle x \rangle}{2T}\left(\frac{x}{1+x^2} + \arctan x\right)} \end{aligned} \tag{4.6}$$

where $Z$ is a normalization constant determined by the usual normalization condition $\int_{-\infty}^{\infty} P(x, \langle x \rangle) dx = 1$.

By taking the derivative with respect to $\langle x \rangle$ at $\langle x \rangle = 0$ in 4.5 the phase boundary in the parameter space of noise intensity and coupling strength can be exactly determined. The resulting phase diagram is shown as the solid line in fig. 4.1.

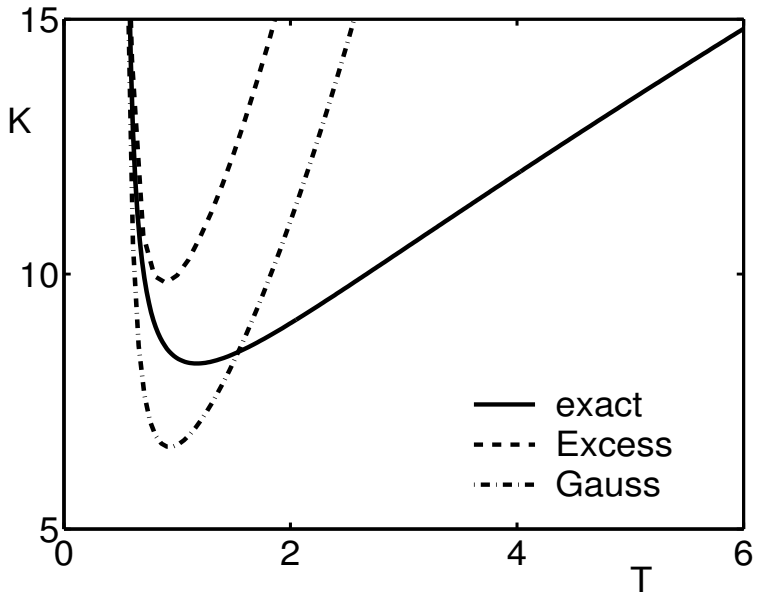


Figure 4.1: Pitchfork bifurcation. Above the curves the system is in the ordered, below them in the disordered state. The Gaussian as well as the Excess approximation perform good for low noise intensities but considerably overestimate the critical value of $K$ at high noise intensities. Still, both show the correct qualitative behavior.

The approach based on the selfconsistent equation 4.5 does not yield any information about the amplitude of the order parameter. In order to extract this information the authors of earlier studies [17, 89] approximated:

$$\begin{aligned} \langle \dot{x} \rangle &\approx f(\langle x \rangle) + T g(\langle x \rangle) g'(\langle x \rangle) \\ &= (2T-1)\langle x \rangle + (2T-2)\langle x \rangle^3 - \langle x \rangle^5 \end{aligned} \tag{4.7}$$

By doing this they neglected the fluctuations $x - \langle x \rangle$. In the limit of infinite coupling strength ($K \to \infty$) this approximation becomes exact. Using linear stability analysis we find that in this approximation the fixed point is stable for $T < \frac{1}{2}$. For $T > \frac{1}{2}$ it becomes unstable. This result is confirmed by the (exact) self-consistent approach.

The reentrant into the disordered state that is observed for finite coupling strength cannot be described using eq. 4.7. Thus, the fluctuations have to be taken into account.

Here we therefore go beyond this approximation. With the help of the moment dynamics that was discussed in chapter 2 we will find an analytic expression for the reentrant. We will also derive an approximate bifurcation diagram. The exact solution from the self-consistent equation will provide a benchmark for our results.

According to eq. 2.14 the dynamics of the mean $\langle x \rangle$ in terms of the central moments $\mu_n$ is given by:

$$\begin{aligned} \dot{\langle x \rangle} &= (2T-2)\mu_3 - \mu_5 + [2T - 1 + 3(2T-2)\mu_2 - 5\mu_4]\langle x \rangle \\ &\quad -10\mu_3\langle x \rangle^2 + (2T - 2 - 10\mu_2)\langle x \rangle^3 - \langle x \rangle^5 \end{aligned} \tag{4.8}$$

Note that the coupling constant $K$ does not explicitely occur in this equation. It enters indirectly via the moments. Their dynamics can be calculated using eq. 2.15. As an example we treat here the second central moment which is governed by the equation:

$$\begin{aligned} \dot{\mu}_2 &= 2T + 2[4T - (1+K)]\mu_2 + (6T-4)\,\mu_4 - 2\mu_6 \\ &+ [4(4T-3)\mu_3 - 10\mu_5]\,\langle x \rangle + [4T + 12(2T-1)\mu_2 - 20\mu_4]\,\langle x \rangle^2 \\ &- 20\mu_3\langle x \rangle^3 + (2T - 10\mu_2)\langle x \rangle^4 \end{aligned} \tag{4.9}$$

Since the nonlinear Langevin equation 4.1 is not a Gaussian process higher than second order moments play a role. This manifests itself in eq. 4.9 where we see that the temporal change of the second central moment depends on the state of up to the sixth moment. Indeed from eq. A.10 we learn that the system of equations for the moment dynamics forms an infinite set of coupled ordinary differential equations.

We cannot solve this infinite set. Still, we can learn something from it [57]: Looking at eq. 4.1 we recognize immediately the reflection symmetry with respect to $x = 0$: $f(-x) = -f(x)$, $g(-x) = g(x)$. We conclude that the mean $\langle x \rangle$ as well as the odd order moments have a fixed point $\langle x \rangle^* = 0$ ($\mu^*_{2n+1} = 0$) at just that value (The star denotes the steady values.). Its stability remains to be determined. If we assume that the probability distribution is unique and its steady state is globally attracting for a given $\langle x \rangle$ (cf. chapter 2) then we know that perturbations orthogonal to $\langle x \rangle$ in the space spanned by $\langle x \rangle$ and the moments $\mu_n$

will decay. We therefore have to investigate perturbations in $\langle x \rangle$, only. We make the ansatz $\langle x \rangle = \langle x \rangle^* + \delta\langle x \rangle$. In linear approximation the temporal evolution of the perturbation $\delta\langle x \rangle$ is given by:

$$\dot{\delta}\langle x \rangle = [2T - 1 + 6(T-1)\mu_2^* - 5\mu_4^*]\delta\langle x \rangle \tag{4.10}$$

The fixed point is stable for:

$$2T - 1 + 6(T-1)\mu_2^* - 5\mu_4^* < 0 \tag{4.11}$$

Unfortunately this equation does not help us to obtain the bifurcation diagram because we do not know the stationary moments $\mu_2$ and $\mu_4$. Anyway we can study the influence of the moments. Even order moments (and even order central moments) are always positive. We therefore see from eq. 4.11 that the fourth order central moment always supports stability of the fixed point. The role of the second moments changes at $T = 1$: For lower values it supports stability for higher values instability. The zeroth order term $(2T - 1)$ changes from supporting stability to supporting instability when $T$ grows beyond $\frac{1}{2}$. For increasing fluctuations $\mu_4$ grows disproportionately high (see fig. 4.2) compared to the other moments present in eq. 4.11. It eventually dominates the equation.

Since in the small noise limit all terms support stability and in the high noise limit the $\mu_4$ dynamics becomes dominant and also supports stability the ordered phase (unstable fixed point at the origin) can exist for intermediate values, only. This is in contrast to the approximation 4.7 but in accordance with the exact solution from the selfconsistent equation 4.5.

In order to investigate the model in more detail we apply the Gaussian approximation (cf. chapter 2) to eq. 4.8 and to the dynamics of the central moments. In this approximation all odd order central moments vanish: $\mu_{2n+1} = 0$. Even order moments $\mu_{2n}$ can be expressed by the variance $\mu_2$. The relations we need can be found in appendix A. For better legibility we denote in this approximation the mean with $m_x$ (and later also $m_y$) and the variance with $D_x$ (and later also $D_y$ and covariance $D_{xy}$).

In the Gaussian approximation the equation for the dynamics of the mean 4.8 becomes:

$$\begin{aligned} \dot{m}_x &= [2T - 1 + 3(2T-2)D_x - 15D_x^2]m_x \\ &\quad +(2T - 2 - 10D_x)m_x^3 - m_x^5 \end{aligned} \tag{4.12}$$

From this we find with the help of a linear stability analysis that the fixed point $m_x^* = 0$ becomes unstable via a pitchfork bifurcation at:

$$2T - 1 + 6(T-1)D_x^* - 15D_x^{*2} = 0 \tag{4.13}$$

From eq. 4.9 we infer that at the fixed point the following equation has to be satisfied:

$$2T + 2[4T - 1 - K]D_x^* + (6T - 4)D_x^{*2} - 30D_x^{*3} = 0 \tag{4.14}$$

With these two equations the bifurcation is determined. The critical value of the coupling strength $K_c$ reads:

$$K_c = 4T - 1 + \frac{T}{D_x^+} + 3D_x^+(3T - 2) - 15(D_x^+)^2, \qquad T > 0.5 \tag{4.15}$$

where

$$D_x^+ = \frac{1}{5} + \sqrt{\frac{1}{25}(T-1)^2 + \frac{1}{15}(2T-1)} \tag{4.16}$$

is the larger one of the two solutions for $D_x^*$ that come out of eq. 4.13. A physically useful solution exists only if $T > 0.5$. For $\frac{\sqrt{10}-2}{3} \leq T < 0.5$ both solutions are negative, for smaller positive values of $T$ they are complex. For $T > 0.5$ there is always exactly one positive solution. In the limit $T \to 0.5$ $D_x^+$ becomes zero and $K_c$ goes to infinity.

We show the bifurcation diagram in fig. 4.1. We find that the Gaussian approximation yields a qualitative agreement with the exact solution which was obtained from the self-consistent equation 4.5: For increasing noise intensities the system undergoes a phase transition from the disordered to the ordered state and then back. A certain coupling strength is necessary for this phenomenon to occur.

The quantitative agreement of the approximation with the exact result is good at low noise intensities. For high intensities it yields considerably higher values of the critical coupling strength.

In order to take a direct look at the quality of the Gaussian approximation we have computed the central moments explicitely. In fig. 4.2 we show the second and the fourth order central moments as they were obtained from the simulation of the Langevin equation 4.1 and compare them to the results from the Gaussian approximation.

Along with the Gaussian approximation we have also plotted the Excess approximation, that is the one obtained by neglecting the cumulants above 4-th order (cf. chap. 2). The explicit equations are too long to be quoted here. We could not find an analytic expression for the bifurcation but did numerical simulations. The results are also shown in fig. 4.1. It correctly predicts the qualitative behavior, too, but the quantitative agreement is worse than in the Gaussian approximation. The Excess approximation always overestimates the critical coupling strength at which the bifurcation occurs.

With the help of the moment dynamics we can obtain quantitative results for the mean $m_x$ as a function of the noise intensity. An example for a coupling

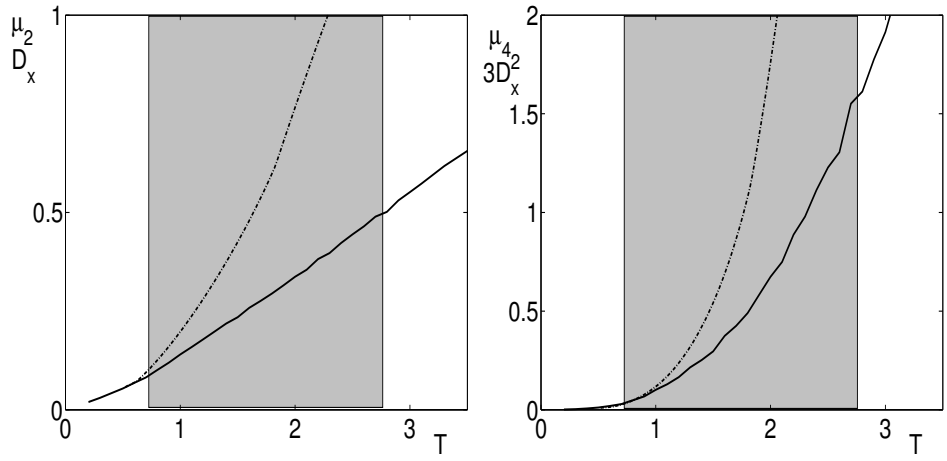


Figure 4.2: Stationary central moments $\mu_2^*$ (left panel) and $\mu_4^*$ (right panel) obtained by the Langevin simulation compared to the results for $D_x$ (left panel) and the forth moment in Gaussian approximation ($3\ D_x^2$; right panel). Up to $T = 1$ the agreement is good. The gray regions depict the noise intensities where the ordered state occurs.

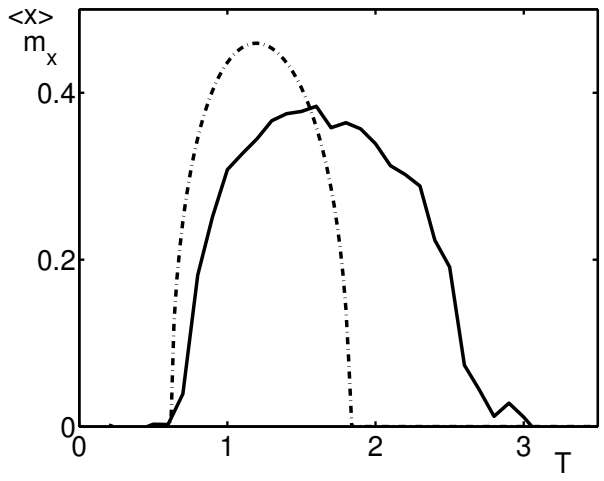


Figure 4.3: $\langle x \rangle$ and $m_x$ as a function of the noise intensity. The solid black line depicts the results from the Langevin simulation ($\langle \langle x \rangle \rangle$), the dashed-dotted gray line the results from the Gaussian approximation ($m_x$). Parameters: $K = 10.0$; $N = 100000$.

strength that is sufficiently high to support the disordered-ordered-disordered transition is shown in fig. 4.3. The results obtained from the Langevin equation 4.1

are presented for comparison. Again we see that the quality of the approximation is good for low noise intensities. The maximum amplitude is overestimated.

## 4.2 Pure Noise-Induced Hopf Bifurcation

Let us now slightly complicate the model. We introduce a second variable $y$ and write:

$$\begin{aligned} \dot{x}_i &= f(x_i) - \frac{K}{N}\sum_{j=1}^{N}(x_i - x_j) + g(x_i)\xi_i(t) - y \\ \dot{y}_i &= ax_i \qquad\qquad\qquad\qquad i = 1 \ldots N \end{aligned} \tag{4.17}$$

with the same functions $f$ and $g$ as in the previous section (eq. 4.3). We have chosen the parameter $a$ to be small and positive (We fixed $a = 0.1$ throughout the chapter.). This value ensures a clear timescale separation and will in a further upgrading of the system in section 4.3 support excitability.

In this case an analytic expression for the stationary probability distribution $P(x, y, \langle x \rangle)$ is not available. The method based on the selfconsistent equation (eq. 4.5 and replacing $P(x, \langle x \rangle)$ with $P(x, y, \langle x \rangle)$) is therefore not applicable in a straightforward way. It has been applied, though, in the limit of small $a$ for determining the systems nullclines [58].

We start investigating the model by numerically simulating the system of Langevin equations 4.17. From a certain coupling strength on we find that for low noise the individual systems are centered around the origin of phase space while for increasing intensities the mean starts oscillating around it. For further increasing intensities the oscillations stop again. The bifurcation diagram is shown in fig. 4.4.

In analogy to the previous section we will call the oscillating state the ordered state and the steady state the disordered state. An example of these oscillations can be found in fig. 4.5.

The individual elements of the ensemble are represented by the small dots. Their average which is described by $\langle x \rangle$ and $\langle y \rangle$ is depicted by the fat dot. The timeseries of the average is shown as the solid line. The individual elements move as a cloud around the fixed point. The mean itself oscillates around the origin of phase space which is located in the middle of each snapshot.

The timeseries of the individual elements is very noisy. Still, the underlying oscillations are clearly visible. A typical example is shown in fig. 4.6.

In order to investigate the dynamical behavior of the mean we set as a first

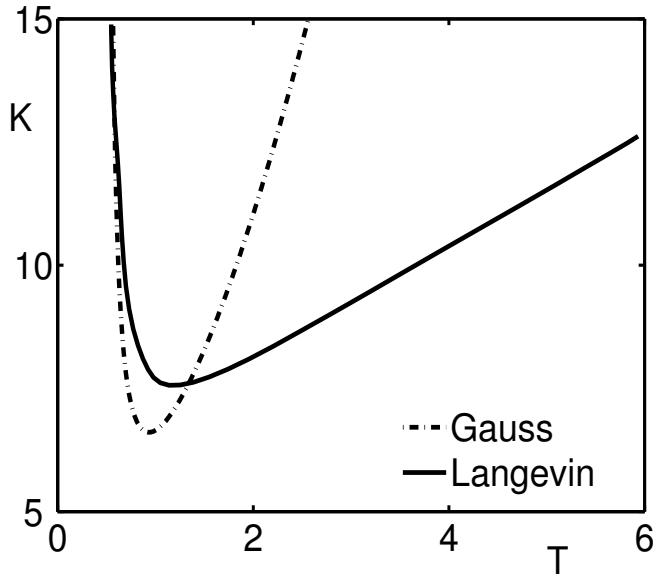


Figure 4.4: Hopf bifurcation. Above the curves the system is in the ordered, below them in the disordered state. Again, the Gaussian approximation performs good for low noise intensities but considerably overestimates the critical value of $K$ at high noise intensities. Still, is reproduces the correct qualitative behavior. $a = 0.1$.

approximation:

$$\begin{aligned} \dot{\langle x \rangle} &= f(\langle x \rangle) + Tg(\langle x \rangle)g'(\langle x \rangle) - \langle y \rangle \\ \dot{\langle y \rangle} &= a\langle x \rangle \end{aligned} \tag{4.18}$$

This ansatz is the two dimensional analog to eq. 4.7. As mentioned above it becomes exact in the limit of infinite coupling strength ($K \to \infty$).

We can easily compute the nullclines of the system. They are determined by the equations:

$$y = -x\left(1+x^2\right)^2 + 2\epsilon x\left(1+x^2\right) \tag{4.19a}$$

$$x = 0 \tag{4.19b}$$

We show plots for different noise intensities in fig. 4.7. The nullcline that is determined by 4.19b lies on the ordinate of the coordinate system. The slope of the other nullclines changes sign at $x = 0$ for $T = 0.5$. At this value a Hopf bifurcation occurs.

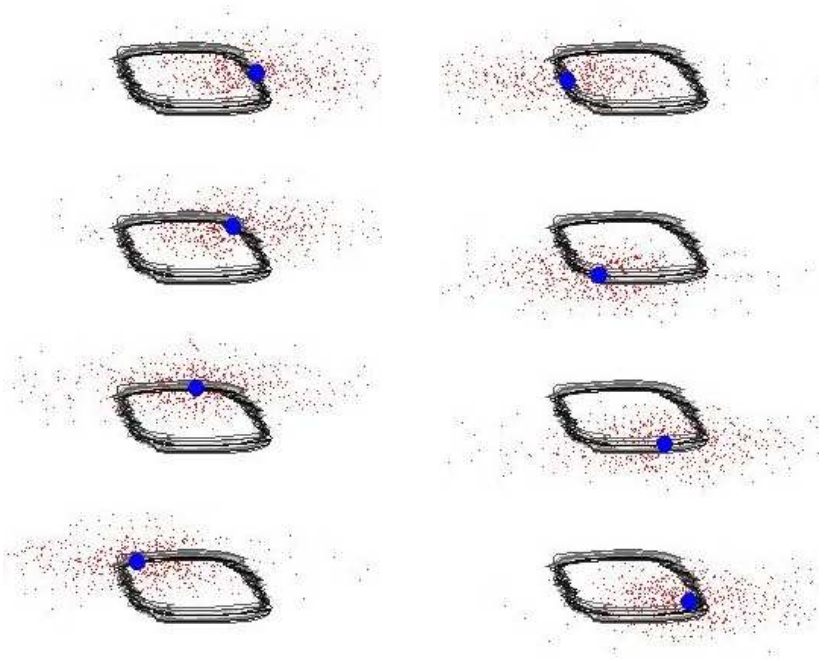

Figure 4.5: Noise-induced oscillations. The different panels show snapshots of the ensemble in phase space. The small dots show the individual elements, the fat dot represents the average of the ensemble and the solid line the trajectory of the average. Time goes from upper left to lower left and then from upper right to lower right. $N = 625$, $K = 10.0$, $T = 1.0$.

In order to go beyond the approximation of eq. 4.18 we compute the moment dynamics for the system 4.17. The dynamics of the mean now depends on the

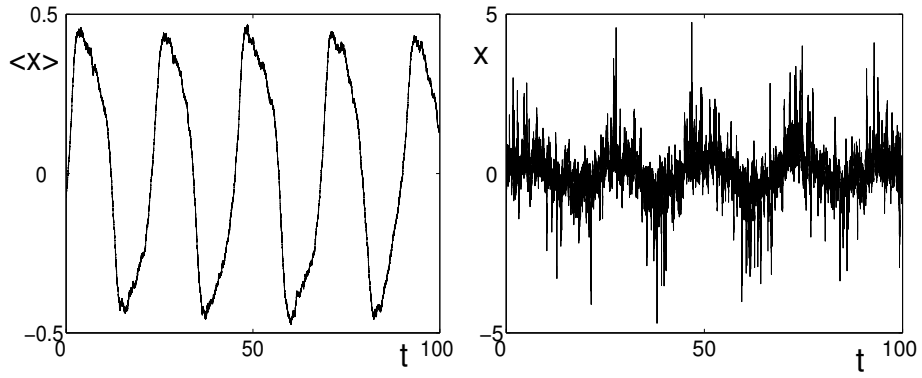


Figure 4.6: Oscillations of the mean $\langle x \rangle$ and of a randomly chosen individual $x$. $N = 10000$, $K = 10.0$, $T = 1.0$.

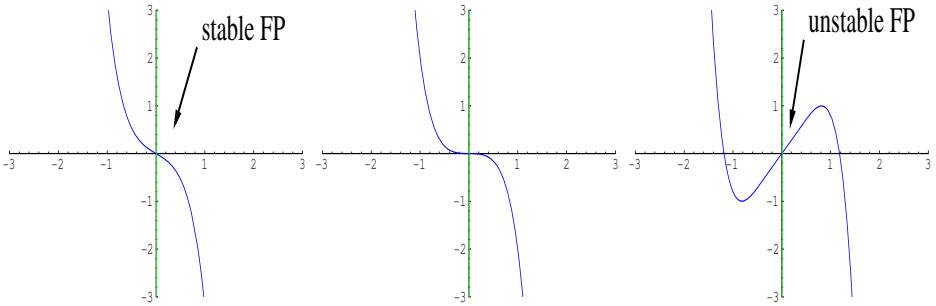


Figure 4.7: Nullclines of the approximation 4.18 for $T = 0.2$ (left panel), $T = 0.5$ (middle panel), and $T = 1.2$ (right panel). One nullclines coincides with the ordinate. The stability of the fixed point at $x = 0$, $y = 0$ is lost at $T = 0.5$ (stable below).

mixed central moments $\mu_{m,n}$ (cf. chapter 2):

$$
\begin{aligned}
\dot{m}_x &= (2T-2)\mu_{3,0} - \mu_{5,0} \\
&+ \left[2T - 1 + 3(2T-2)\mu_{2,0} - 5\mu_{4,0}\right] m_x - 10\mu_{3,0} m_x^2 \\
&+ (2T - 2 - 10\mu_{2,0}) m_x^3 - m_x^5 - m_y \qquad (4.20a) \\
\dot{m}_y &= a m_x \qquad (4.20b) \\
\dot{\mu}_{2,0} &= 2T + 2\left[4T - (1+K)\right]\mu_{2,0} - 2\mu_{1,1} + (6T-4)\mu_{4,0} \\
&- 2\mu_{6,0} + 2\left[(10T-6)\mu_{3,0} - 5\mu_{5,0}\right] m_x \\
&+ 2\left[2T + 6(2T-1)\mu_{2,0} - 10\mu_{4,0}\right] m_x^2 \\
&- 20\mu_{3,0} m_x^3 + (2T - 10\mu_2) m_x^4 \qquad (4.20c) \\
\dot{\mu}_{0,2} &= 2a\mu_{1,1} \qquad (4.20d) \\
\dot{\mu}_{1,1} &= (2T - K - 1)\mu_{1,1} + a\mu_{2,0} - \mu_{0,2} + (2T-2)\mu_{3,1} - \mu_{5,1} \\
&+ \left[3(2T-2)\mu_{2,1} - 5\mu_{4,1}\right] m_x + \left[3(2T-2)\mu_{1,1} - 10\mu_{3,1}\right] m_x^2 \\
&- 10\mu_{2,1} m_x^3 - 5\mu_{1,1} m_x^4. \qquad (4.20e)
\end{aligned}
$$

We show here the dynamics of the lowest order moments, only. They are the ones we need for the Gaussian approximation.

Taking into account the symmetry of the model 4.17 with respect to a transformation $x \to -x$ and $y \to -y$ we conclude that there must be a fixed point at $m_x^* = m_y^* = \mu_{2n+1,m}^* = \mu_{n,2m+1}^* = 0$. The stationary even moments are determined by an infinite set of coupled equations that is given by A.10. We show here three conditions that can be derived from 4.20:

$$\begin{aligned} 0 &= 2T + 2\left(4T - 1 - K\right)\mu_{2,0}^* + 2(3T-2)\mu_{4,0}^* - 2\mu_{6,0}^* \\ 0 &= a\mu_{2,0}^* - \mu_{0,2}^* + 2(T-1)\mu_{3,1}^* - \mu_{5,1}^* \\ 0 &= \mu_{1,1}^* \end{aligned} \tag{4.21}$$

The stationary moments are not fully determined by these equations. Once we apply the Gaussian approximation the equations become valuable, though. In this approximation all central moments can be expressed by $\mu_{2,0}$, $\mu_{1,1}$, and $\mu_{0,1}$. The relations we need can be found in appendix A.

Within the Gaussian approximation the three stationary moments $\mu_{2,0}^*$, $\mu_{1,1}^*$, and $\mu_{0,1}^*$ are determined by the three equations 4.21 (In this approximation we again change to the notation $m_x$, $m_y$, $D_x$, $D_y$, $D_{xy}$ introduced earlier.). The infinite set of equations for the moments together with the dynamics of the mean eq. 4.20 becomes a closed set of five variables. (For the explicit form see eq. 4.32 and set $b = 0$.)

With the stationary solutions for the mean values and the moments we can now perform a linear stability analysis. We write in linear approximation for the evolution of a small perturbation

$$\dot{\vec{\delta}} = \hat{J}\vec{\delta} \tag{4.22}$$

with the vector $\vec{\delta}^T = \left(\delta m_x\ \delta m_y\ \delta D_x\ \delta D_y\ \delta D_{xy}\right)$ and the Jacobian $\hat{J}$ which reads:

$$\begin{pmatrix} \lambda_1 & -1 & 0 & 0 & 0 \\ a & 0 & 0 & 0 & 0 \\ 0 & 0 & \lambda_2 & 0 & 0 \\ 0 & 0 & 0 & 0 & 2k \\ 0 & 0 & k & -1 & \lambda_3 \end{pmatrix} \tag{4.23}$$

where

$$\begin{aligned} \lambda_1 &= 2T - 1 + 3(2T-2)D_x^* - 15(D_x^*)^2 \\ \lambda_2 &= 2(4T - 1 - T) + 24(T-1)D_x^* - 90(D_x^*)^2 \\ \lambda_3 &= 2T - 1 - T + 3(2T-2)D_x^* - 15(D_x^*)^2 \end{aligned} \tag{4.24}$$

Since the Jacobian 4.23 is of block diagonal form the stability of $m_x$ and $m_y$ at the fixed point $m_x^* = m_y^* = 0$ is separated from that of $D_x$, $D_y$, and $D_{xy}$. For the analytic investigation we have to consider the upper left block, only. Its eigenvalues are given by:

$$\rho_\pm = \frac{1}{2}\left(\lambda_1 \pm \sqrt{\lambda_1^2 - 4a}\right) \tag{4.25}$$

Since we have chosen $a > 0$ the fixed point becomes unstable at $\lambda_1 = 0$. This condition is equivalent to the condition for the pitchfork bifurcation in the previous section. The critical coupling strength at which the Hopf bifurcation occurs is therefore also given by eq. 4.15. It is plotted in fig. 4.4 together with results from Langevin simulations. Quantitatively the disagreement is rather large but the qualitative features are again correctly reproduced.

For a closer look at the oscillations we introduce $\hat{r} = \sqrt{\langle x\rangle^2 - \langle y\rangle^2}$. As the radius of the oscillations $r$ we then define the maximum of $\hat{r}$ during a certain time (long compared to an oscillation period). This value is plotted in fig. 4.8 and

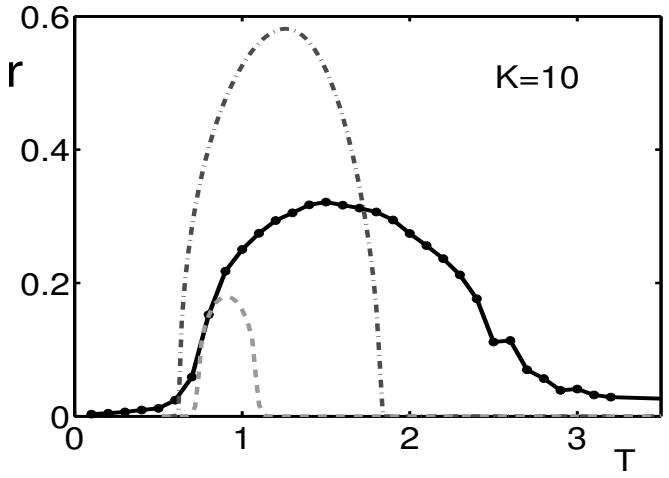


Figure 4.8: Radius of oscillations $r$ versus noise intensity. Results from Langevin simulations ($N = 10000$; solid line), Excess approximation (dashed line) and Gaussian approximation (dash-dotted line) are shown. $a = 0.1$.

compared to the results from the moment dynamics. Here the radius is defined as above but with $m_x$ instead of $\langle x\rangle$ and $m_y$ instead of $\langle y\rangle$.

Not only the radius of the oscillations but also their shape depends on the parameters. In fig. 4.9 we see that for small radii the oscillations resemble those of a harmonic oscillator. For higher radii they look strikingly similar to oscillations

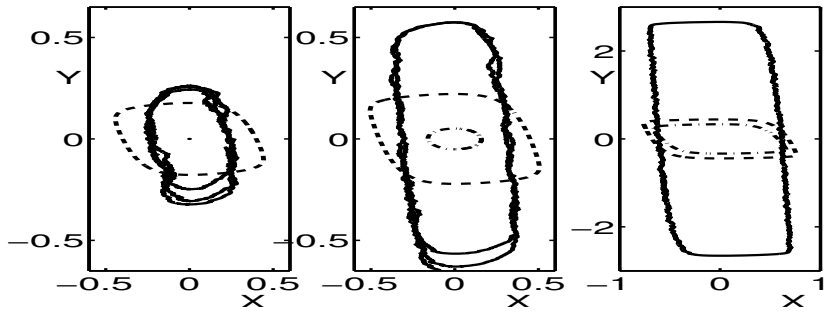


Figure 4.9: Limit Cycles for different values of the coupling strength $K$ (from left to right: $K = 9, 10, 20$). The solid black line shows results from the Langevin simulation, the dashed dark gray line from the Gaussian approximation and the dash-dotted light gray line from the Excess approximation. Parameters: $N = 10000$ (for Langevin), $T = 1$, $a = 0.1$

observed in the FitzHugh-Nagumo system (cf. chapter 3). This holds also for the Gaussian and the Excess approximation.

### 4.2.1 Local Coupling - Noise-Induced Spiral Patterns

In this part of the section we take a look at the effect of local coupling. In contrast to the one-variable [18] case we expect new patterns. We introduce a spatial alignment and change the coupling term in eq. 4.17 so that it now becomes:

$$\begin{aligned} \dot{x_{i,j}} &= f(x_{i,j}) + K\Delta x_{i,j} + g(x_{i,j})\xi_{i,j}(t) - y \\ \dot{y_{i,j}} &= a x_{i,j} \qquad\qquad\qquad\qquad i = 1 \ldots l_1, j = 1 \ldots l_2 \end{aligned} \tag{4.26}$$

Here $\Delta$ is the discrete version of the Laplace operator. The noise $\xi_{i,j}$ is again Gaussian and white:

$$\langle \xi_{i,j}(t) \rangle = 0, \qquad \langle \xi_{i,j}(t)\xi_{k,l}(t') \rangle = \sigma^2 \delta_{ik}\delta_{jl}\delta(t - t') \tag{4.27}$$

The parameter $a$ is fixed as before: $a = 0.1$.

The moment dynamics method does not work in the usual way in this case. We therefore restrict ourselves to the simulation of the Langevin dynamics 4.26. We find that again for strong enough coupling the system shows with increasing noise intensity a transition from one state to another and a reentrant into the first state. In analogy to the previous sections we call the state with intermediate noise intensities the ordered state, the other one the disordered state.

In the disordered state the behavior of the system does not differ much from the global coupling case of the previous section. The single systems stay close to

the origin of phase space. In the ordered state their behavior changes: They start to oscillate. Diffusive coupling leads to spatially homogenized regions. A spiral emerges (fig. 4.10).

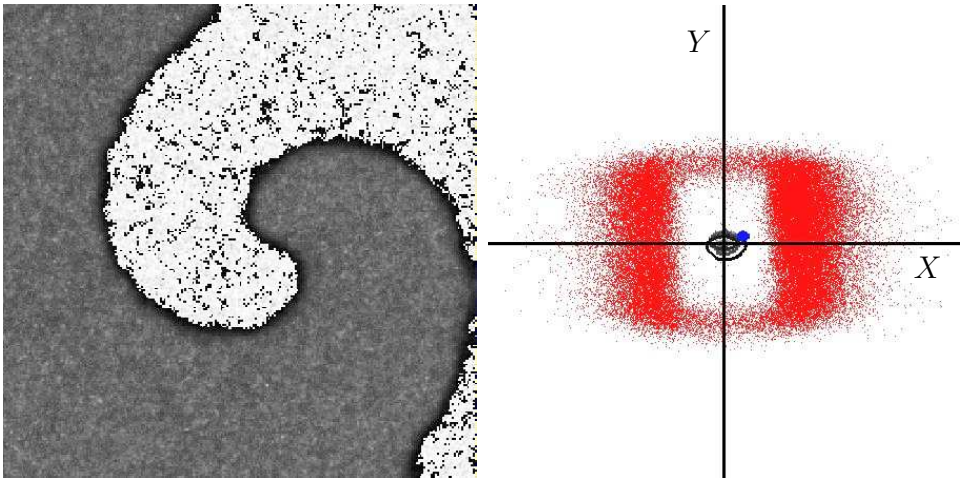


Figure 4.10: Ordered state in the case of local coupling. In real space (left panel) we find a rotating spiral wave(high $x$-values are dark, low values light). In the right panel we show the phase portrait. The small dots show the individual systems, the fat dot the mean and the solid line the timeseries of the mean. As can be seen, the mean hardly moves. The individual systems oscillate around the origin of phase space. Parameter: $T = 2$, $K = 50$, $a = 0.1$.

## 4.3 Pure Noise-Induced Excitability

In this section we will apply the final upgrade to our system in terms of an additional parameter $b > 0$:

$$\begin{aligned} \dot{x}_i &= f(x_i) - \frac{K}{N}\sum_{j=1}^{N}(x_i - x_j) + g(x_i)\xi_i(t) - y \\ \dot{y}_i &= a(x_i + b) \qquad\qquad i = 1 \ldots N \end{aligned} \tag{4.28}$$

The functions $f$ and $g$ and the noise term $\xi_i(t)$ are the same as in the previous sections (eq. 4.3 and 4.2). The parameter $a$ is again fixed ($a = 0.1$).

For a first rough approximation we again set:

$$\langle f(x)\rangle = f(\langle x\rangle), \quad \langle g(x)\rangle = g(\langle x\rangle) \tag{4.29}$$

and we find a fixed point at:

$$\begin{aligned} x^* &= -b \\ y^* &= b(1-2T+b^2)(1+b^2) \end{aligned} \tag{4.30}$$

The fixed point is stable for small $T$ and becomes unstable at

$$T_c = \frac{5b^4+6b^2+1}{6b^2+2} \tag{4.31}$$

This is a monotonic function of $b$ (remember we set $b>0$) that starts with $T_c = \frac{1}{2}$ for $b=0$ just as we found in the previous section and grows proportional to $b^2$ in the limit of large $b$. As mentioned before this approximation becomes correct in the limit of infinite coupling.

For finite coupling we turn to the moments dynamics method. The dynamics of the mean and the moment dynamics are readily computed. We give them directly in the Gaussian approximation:

$$\begin{aligned} \dot{m_x} &= \left[2T-1+6(T-1)D_x-15D_x^2\right] m_x \\ &+ 2(T-1-5D_x)m_x^3 - m_x^5 - m_y && \text{(4.32a)} \\ \dot{m_y} &= a(m_x+b) && \text{(4.32b)} \\ \dot{D_x} &= 2T+2\left[4T-(1+K)\right]D_x - 2D_{xy} + (3T-2)6D_x^2 - 30D_x^3 \\ &+ 4\left[T+3(2T-1)D_x-15D_x^2\right]m_x^2 + 2(T-5D_x)m_x^4 && \text{(4.32c)} \\ \dot{D_y} &= 2aD_{x,y} && \text{(4.32d)} \\ \dot{D_{xy}} &= (2T-K-1)D_{xy} + aD_x - D_y + (T-1)6D_xD_{xy} - 15D_x^2D_{xy} \\ &+ 6\left[(T-1)D_{xy} - 5D_xD_{xy}\right]m_x^2 - 5D_{xy}m_x^4. && \text{(4.32e)} \end{aligned}$$

Note that the parameter $b$ destroys the symmetry under the transformation $m_x \to -m_x$, $m_y \to -m_y$. The origin is no longer a fixed point which is instead given by:

$$\begin{aligned} m_x &= -b \\ D_{xy} &= 0 \\ Dy &= aD_x \\ m_y &= -[2T-1+3(2T-2)D_x-15D_x^2]b \\ &- (2T-2-10D_x)b^3 + b^5 \end{aligned} \tag{4.33}$$

and $D_x$ is given by the (real) positive solution of

$$\begin{aligned} 0 &= D_x^3 + D_x^2[6(3T-2)-60b^2] + D_x[12b^2(2T-1) \\ &- 10b^4 + 2(4T-K-1)] + 2T + 4b^2T + 2b^4T \end{aligned} \tag{4.34}$$

In the parameter regime we study there is always exactly one positive solution.

The stability of this solution can in principle be computed via a linear stability analysis. Unfortunately the block diagonal of the Jacobian 4.23 from the previous section is now destroyed by the presence of the parameter $b$. The calculations become significantly more complex. We resort here to a numerical investigation.

For this we fix the parameter $b = 0.75$ and start off with Langevin simulations. Depending on the coupling constant and the noise intensity we find three different dynamical regimes. Typical timeseries are shown in fig. 4.11.

The first regime we call monostable. The mean is centered around a fixed value. We have applied perturbations to the system by shifting $\langle x \rangle$ and $\langle y \rangle$ but leaving the central moments constant, i.e. we added a certain value to each $x_i$ and each $y_i$ of the ensemble. Various other methods are possible. The described perturbations of different sizes decay (upper panel in fig. 4.11). Tests with various other magnitudes and directions in the plane of $\langle x \rangle$ and $\langle y \rangle$ showed similar results. The second regime we call excitable. Although in this regime, too, we find only one stable fixed point the dynamical behavior is quite different: Here the system is also centered around a fixed value but an adequate small perturbation leads to a large excursion in phase space until the starting point is reapproached again (upper panel in fig. 4.11). The third regime we call oscillatory. Here $\langle x \rangle$ and $\langle y \rangle$ show continuous oscillations without having applied any perturbations (lower panel in fig. 4.11).

The two timeseries of the excitable and the monostable case shown in fig. 4.11 clearly exhibit different behavior but a strict boundary between the two regimes is hard to define. In fig. 4.12 we show the phase diagram as obtained by numerical simulations of the moment dynamics 4.32. Here we found continuous periodic oscillations in the regime labeled oscillatory. At all other values we found exactly one stable fixed point which we call $\big(m_{y,0}\, m_{y,0}\big)$. As the distance to the fixed point we introduce $d = \sqrt{(m_x - m_{x,0})^2 + (m_y - m_{y,0})^2}$ which is generally time dependent.

In order to draw the bifurcation line between the regime we call monostable and the regime we call excitable we let the system relax to the fixed point and then applied a special perturbation. Those values at which $d$ after applying the perturbation ever grew on its way through phase space back to the fixed point we call excitable, those at which it monotonously decreased we call monostable. Applying this perturbation means that we set $m_x = 0.1$, $m_y = -0.1$, and left $D_x$, $D_y$, and $D_{xy}$ at the stationary values. In the $m_x$-$m_y$ phase space this describes a point that lies within the limit cycles obtained in the oscillatory regime. This choice of the perturbation proved practicable for the distinction between the two regimes. Small changes of this perturbation lead to hardly any changes in the phase diagram.

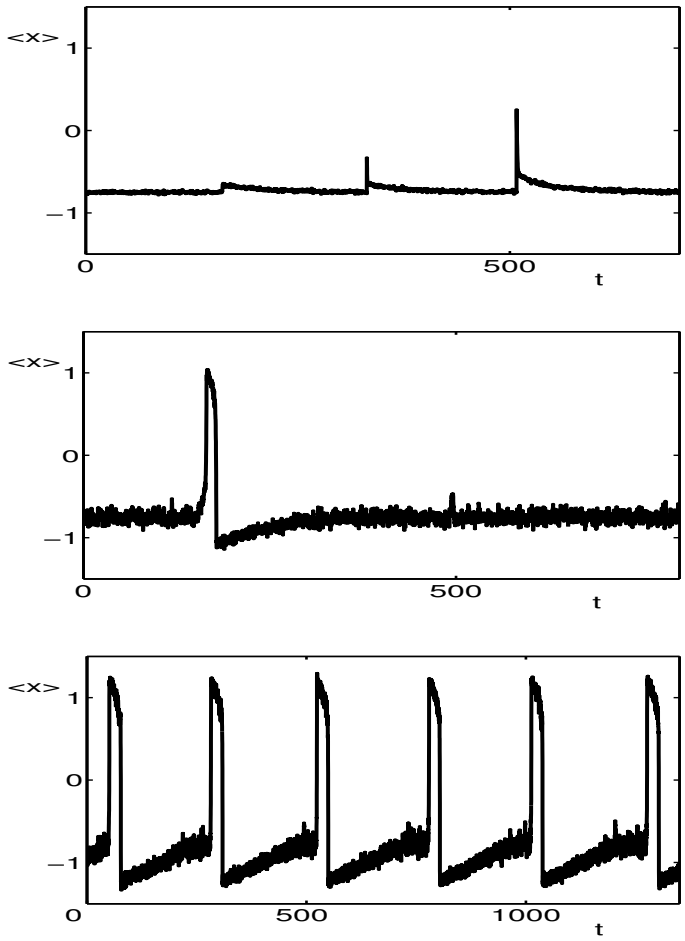


Figure 4.11: Timeseries for $\langle x \rangle$. In the upper panel perturbations of various magnitudes decay. The corresponding region in fig.4.12 is labeled *monostable*. In the middle panel a small perturbation (at $t \approx 150$) leads to a large response of the system (*excitable* in fig.4.12). In the lower panel continuous oscillation can be observed without external perturbation (*oscillatory* in fig.4.12). From top to bottom $T = 0.2$, $K = 10$; $T = 1.5$, $K = 35$; $T = 2.5$, $K = 35$. Other parameters: $N = 625$, $b = 0.75$, $a = 0.1$.

It is interesting to look at the transition from the excitable to the oscillatory regime in some detail. We find that it is rather complex as is shown in fig. 4.13. We see that when the fixed point looses stability the mean starts oscillating with a small amplitude around that fixed point. When the noise intensity increases the oscillations undergo a period doubling. Further period doublings lead to chaos. During this period doubling cascade the system still shows features of excitability.

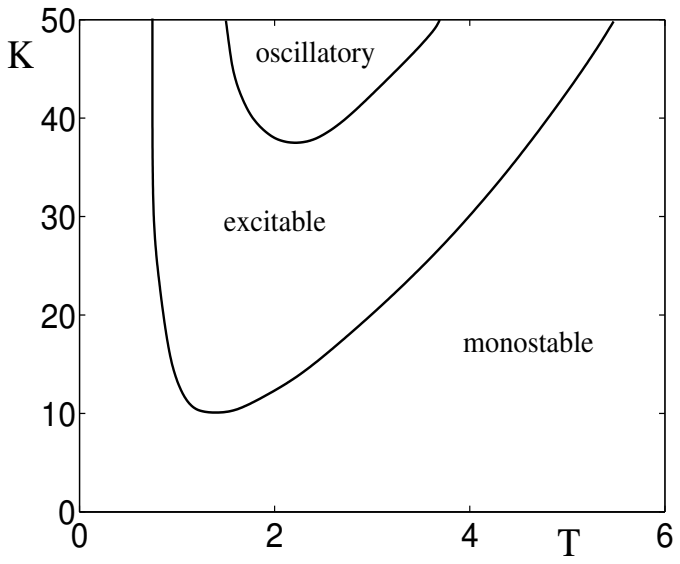


Figure 4.12: Bifurcation diagram in Gaussian approximation. See text for distinction between the regions labeled monostable and excitable. Parameters: $a = 0.1$, $b = 0.75$.

A perturbation exceeding a certain threshold leads to a large excursion in phase space (spike). We therefore call these small amplitude oscillations also *subthreshold oscillations*. With only a slight further increase of the noise intensity the oscillations quickly grow. This constitutes a *Canard Explosion* (cf. chap. 3). In this state the large amplitude oscillations (spikes) are interrupted by small amplitude oscillations (intermittent spiking). With increasing noise intensity the sub-threshold oscillations vanish. This complicated transition occurs in such a small parameter range that it cannot be resolved in the bifurcation diagram 4.12.

We look further into the details of the transition from subthreshold oscillations to spiking in chapter 5 where we find strikingly similar behavior in a globally coupled system with FitzHugh–Nagumo dynamics.

## 4.4 Summary

We have investigated three cases of pure noise-induced phase transitions. In all three cases the mean of the ensemble which served as an order parameter has a single stable fixed point for vanishing noise and in the limit of large noise intensity.

In the first case which is well known in literature there exists for increasing

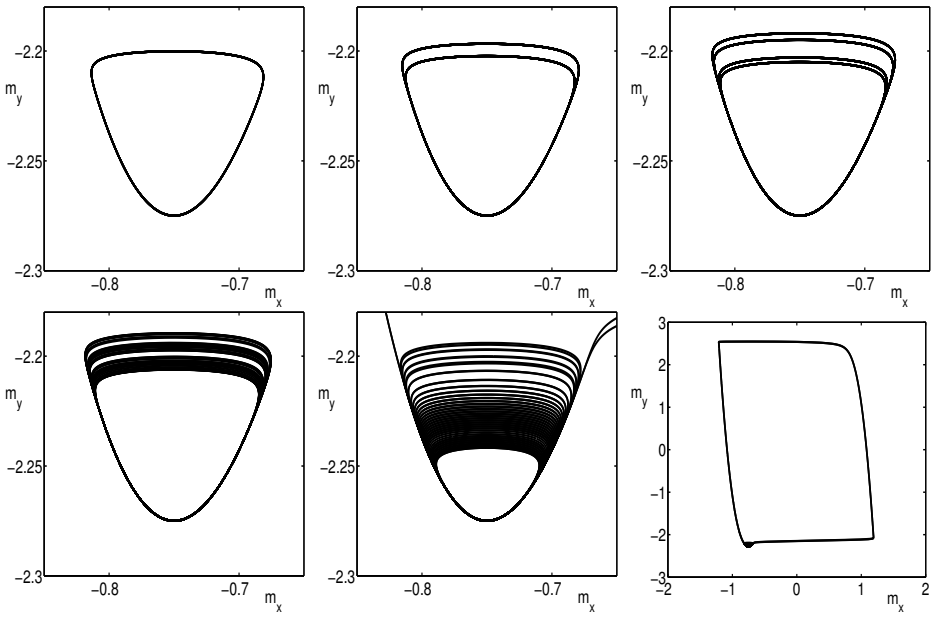


Figure 4.13: Transition from subthreshold oscillations to spiking. For increasing noise intensity the mean ($m_x$ and $m_y$) starts off at a stable fixed point (not shown), then starts to oscillate with a small amplitude. The oscillation undergoes a period doubling cascade until chaos emerges. After that the amplitude quickly increases. Parameters in the lower left picture are the same as in the lower middle picture but the section is enlarged. Note the small parameter range in which these changes occur. Noise intensity $T$ from left to right (upper row): 1.926585, 1.92658504, 1.926585052 and 1.926585055, 1.92658506 (lower row). Other parameters: $a = 0.1$, $b = 0.75$. Note the similarities to fig. 5.7.

noise intensity a pitchfork bifurcation towards a bistable state and a reentrant back to the monostable state. With the help of the moment dynamics method we have given an analytical expression describing the bifurcation.

In the second case we have found a Hopf bifurcation which is in Gaussian approximation determined by the same condition as the pitchfork bifurcation. For local coupling the model supports spiral pattern formation.

In the third case we have observed noise induced excitability. The transition from the excitable to the oscillating regime implies period doubling, chaos, and intermittent spiking, phenomena which are pure noise-induced as well.

# Chapter 5

# Noise-Induced Phenomena in an Ensemble of Globally Coupled FitzHugh-Nagumo Elements

In this chapter we investigate the dynamics of a globally coupled ensemble of $N$ excitable elements with FitzHugh-Nagumo dynamics under the influence of additive noise. The dynamics of the ensemble is enriched by the fluctuations compared to the deterministic case.

As order parameter we use the mean of the ensemble. For uncorrelated noise acting on each individual element (local noise) a coarse view yields a transition from a steady equilibrium for low noise intensities to global oscillations for intermediate intensities and back to the steady equilibrium for high intensities [130]. A closer look shows that this transition is dynamically rich. Diverse regimes of collective behavior are observed.

In section 5.1 we look at these different regimes. Subsection 5.1.1 covers the Langevin dynamics of the ensemble. Due to limited computer power this method is not exact enough for our purposes. In order to understand details and mechanisms of the noise-induced dynamics we consider the thermodynamic limit $N \to \infty$ of the ensemble and consider the moment dynamics for the ensemble (subsection 5.1.2).

In section 5.2 we introduce correlations in the noise sources. In this case the equations for the moment dynamics become stochastic themselves. The coherence of the observed oscillations depending on the correlation strength is investigated.

## 5.1 Local Noise: From Subthreshold Oscillations to Spiking

We study the following system of equations:

$$\begin{aligned} \epsilon \dot{x}_i &= x_i - \frac{x_i^3}{3} - y_i + K\left(\langle x\rangle - x_i\right), \\ \dot{y}_i &= x_i + a + \zeta_i(t), \qquad i = 1, \ldots, N. \end{aligned} \tag{5.1}$$

Here $\zeta_i(t) = \xi_i(t) + \eta(t)$ is the sum of local and global fluctuations. $\xi(t)$ and $\eta(t)$ are Gaussian and white and so is their sum. Their characteristics are determined by:

$$\begin{aligned} \langle \zeta_i(t)\rangle &= \langle \eta(t)\rangle = \langle \xi_i(t)\rangle = 0 \\ \langle \zeta_i(t_1)\zeta_j(t_2)\rangle &= 2T_{loc}\delta_{ij}\delta(t_1 - t_2) + 2T_{glob}\delta(t_1 - t_2) \end{aligned} \tag{5.2}$$

In this first part we set $\eta(t) = 0$ and thus neglect correlations between the fluctuations acting on the elements. Throughout the chapter we fix: $a = 1.05$ and $\epsilon = 0.01$. With these parameters an individual system without noise is in the excitable parameter regime (cf. sec. 3.1). The eigenvalues of the linearized dynamics have a nonzero imaginary part. Therefore the fixed point is a stable focus.

In the noiseless case ($\zeta_i(t) = 0$) it is easy to find the single fixed point of the system: $x_i = -a$, $y_i = \frac{a^3}{3} - a$ for all $i = 1 \ldots N$. We write down the characteristic equation

$$\left(\lambda^2 - \frac{1 - a^2}{\epsilon}\,\lambda + \frac{1}{\epsilon}\right)\left(\lambda^2 - \frac{1 - a^2 - K}{\epsilon}\,\lambda + \frac{1}{\epsilon}\right)^{N-1} = 0 \tag{5.3}$$

and find that the fixed point is stable for $a^2 > \max(1, 1 - K)$ and unstable otherwise. We note that positive coupling of whatever strength does not influence the stability of the fixed point.

The inclusion of fluctuations introduces a new control parameter namely the intensity of the noise $T_{loc}$. A change in this parameter affects the dynamics of the ensemble. In order to describe the set of elements characterized by eq. 5.1 we use the averages $\langle x\rangle = \sum_{i=1}^{N} x_i$ and $\langle y\rangle = \sum_{i=1}^{N} x_i$ which are generally time dependent. In [130] it was shown that an increase of $T_{loc}$ affects not only the position of the fixed point (Strictly speaking this is not a fixed point because the dynamics of the finite system 5.1 are always stochastic. Still, in our simulations the averages $\langle x\rangle$ and $\langle y\rangle$ varied only very little if they were at what we here call the stable fixed point.) but also its stability. For increasing $T_{loc}$ the fixed point looses stability, oscillations emerge, and it regains stability for even higher $T_{loc}$ again.

### 5.1.1 Langevin Dynamics

The transition from a stable fixed point to global oscillations and back exhibits a surprising complexity. We investigate it by means of direct simulation of 5.1 and show timeseries for the mean $\langle x \rangle$ and for an individual $x_i$ in fig. 5.1.

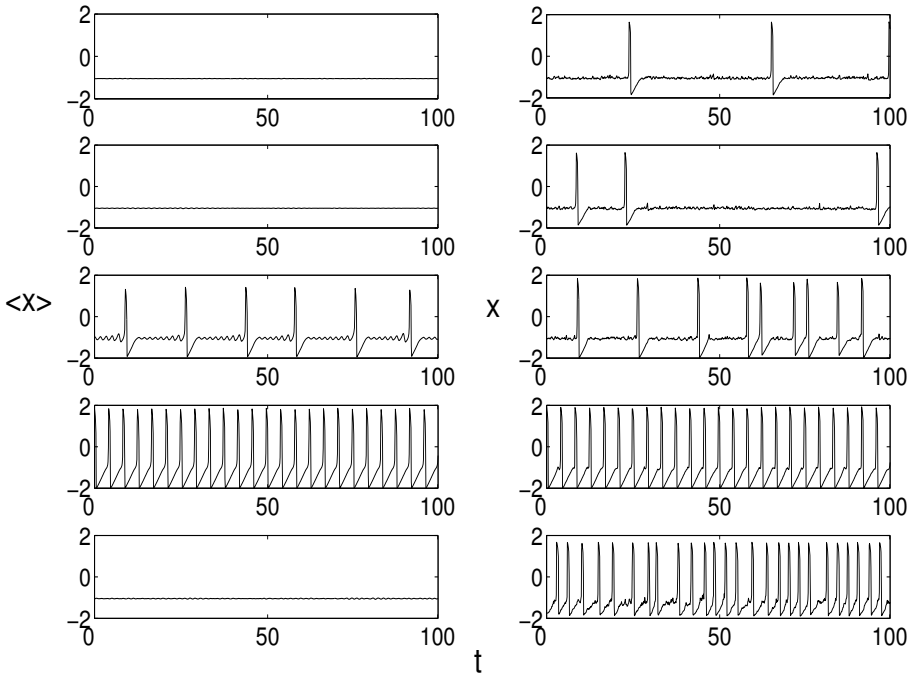


Figure 5.1: Timeseries for different noise intensities. The left column shows the ensemble average the right column a randomly chosen individual unit. For increasing noise intensity the spike rate of the single element increases quickly and then remains on a high level. The spike rate of $\langle x \rangle$ increases at first but then the synchronization between the individual elements is lost and the spike rate decreases again. Note the small range of noise intensities (from top to bottom): $T_{loc} = 2.7 \times 10^{-4}$, $2.8 \times 10^{-4}$, $2.9 \times 10^{-4}$, $3.0 \times 10^{-4}$, $3.1 \times 10^{-4}$. Other parameters: $K = 0.1$.

Here we used the Heun algorithm with step size $dt = 0.001$ for an ensemble of $N = 10^5$ elements. For nonzero noise the individual ensemble elements move randomly around the mean $\langle x \rangle$ and $\langle y \rangle$, occasionally cross the excitation threshold and spike. Due to the large number of elements and a lack of synchronization between them the mean $\langle x \rangle$ is hardly affected by these spikes.

The situation changes for higher intensities. The ensemble starts exhibiting collective dynamics. The mean starts oscillating with small amplitude around

the fixed point. The amplitude slightly increases until a spike emerges. These intermediate oscillations have also been observed in other theoretical [74] and experimental [79] studies. The individual elements often spike several times between two spikes of the mean. For further increasing noise the synchronization of the ensemble increases even more. The number of small oscillations of the mean between two spikes gradually decreases and the oscillations become more regular until uninterrupted spiking occurs. The individual units follow these spikes. The representation of the spikes in phase space strongly resemble those of spikes of uncoupled excitable units (cf. chapter 3).

A further increase of the noise intensity weakens the synchronization again. The individual units still spike but the mean does not. The amplitude of its oscillation decreases until the system returns to the fixed point again.

As a measure of the magnitude of the oscillations we introduce $d = max(\langle x \rangle) - min(\langle x \rangle)$. $max(\langle x \rangle)$ and $min(\langle x \rangle)$ are the extrema of a timeseries of length $t = 100$. This is much longer than the time of a typical oscillation (cf. fig. 5.1). In fig. 5.2 we show $d$ plotted against the noise intensity $T_{loc}$. We find a complex

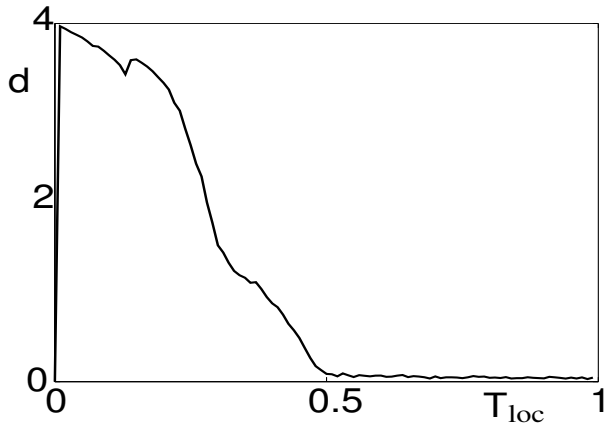


Figure 5.2: Magnitude of oscillations $d$ versus noise intensity $T_{loc}$. We find a complex dependency that agrees qualitatively very well with the features shown in fig. 5.14. Parameters: $\epsilon = 0.05$, $K = 0.5$.

dependency of the magnitude of the oscillations on the fluctuations. The amplitude quickly increases with increasing intensity, then slowly decreases, exhibits a hump, decreases again and finally almost completely decays. This complex structure will be further investigated in the next section.

The transition is even more complicated than we have seen so far: It is especially interesting to look at the Hopf bifurcation at low noise intensities. Typical phase portraits are presented in fig. 5.3. For small fluctuations the mean ($\langle x \rangle$ and

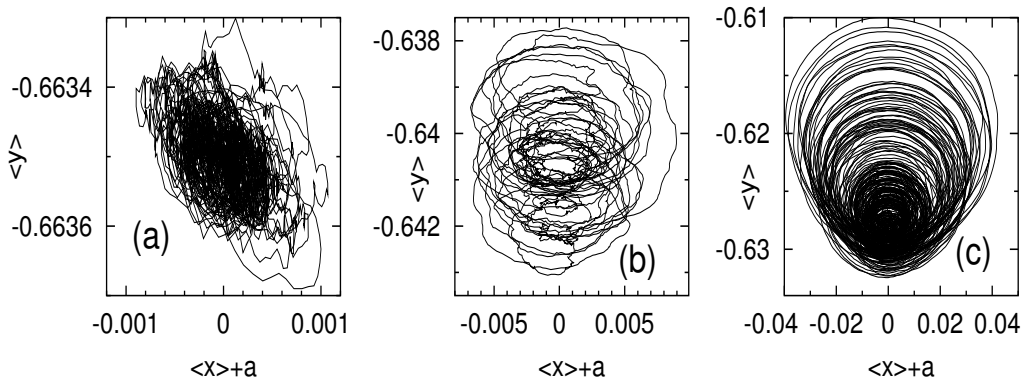


Figure 5.3: Noise-induced onset of local oscillations around the equilibrium for $a = 1.05$, $\epsilon = 0.01$, $K = 0.1$, $N = 10^5$: (a) $T_{loc} = 10^{-4}$, (b) $T_{loc} = 2.4 \times 10^{-4}$, (c) $T_{loc} = 2.7 \times 10^{-4}$. Changes in the phase portrait indicate a bifurcation from disordered fluctuations to subthreshold oscillations. Note the smallness of the oscillation amplitude.

$\langle y \rangle$) shows only minor excursions from some average value. For increasing noise the amplitude of these excursions grows. The time average of $\langle x \rangle$ is hardly at all affected whereas that of $\langle y \rangle$ is shifted towards smaller values. Besides qualitative changes occur. At first (5.3 (a)) the motion resembles a non-biased random walk. At slightly higher values of $T_{loc}$ (5.3 (b)) the motion gradually acquires the character of a noisy rotation. Still higher values (5.3 (c)) provoke phase portraits that are reminiscent of the spiral chaotic attractor.

The dynamics of the mean that we show are very noisy. In order to exclude numerical artefacts and finite size effects we have performed control runs with a much greater ($N = 3.2 \times 10^7$) number of coupled systems (fig. 5.4). We see that the system indeed starts oscillating with small amplitude. The fluctuations of the mean are too strong to determine chaos in the dynamics, though. The computations have been done on a cluster using a parallel computing algorithm. They are very time and memory consuming. Another substantial increase of the number of systems cannot be done with our hardware. We postpone the question whether the system indeed exhibits chaos to the next section.

In fig. 5.5 we present the bifurcation diagram of the system. We see that subthreshold oscillations and spiking both exist in a limited region of the parameter space, only. Too high and too low noise intensities as well as too high and too low coupling strengths suppress the oscillations of the mean. If the fluctuations are too small the ensemble is dominated by the deterministic dynamics and the individual systems stay close to the deterministic fixed point. If they are too large any coherence between the elements is destroyed. For insufficient coupling strength

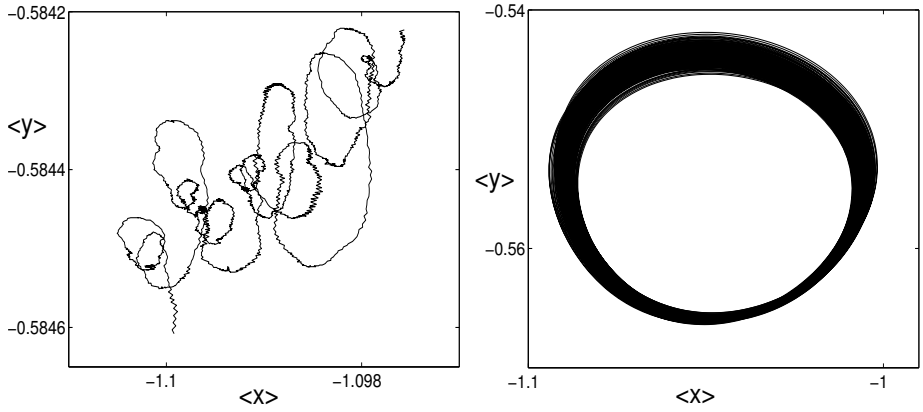


Figure 5.4: Small amplitude oscillations for $N = 3.2 \times 10^7$. In the left panel (lower noise intensity) a random walk like behavior can be observed. In the right panel (higher noise intensity) small amplitude oscillations can clearly be seen. The fluctuations are still too large for a detailed investigation of the dynamics. Parameters: $T_{loc} = 3.0 \times 10^{-4}$ (left), $T_{loc} = 3.2 \times 10^{-4}$ (right), $a = 1.05$, $\epsilon = 0.01$, $K = 0.1$.

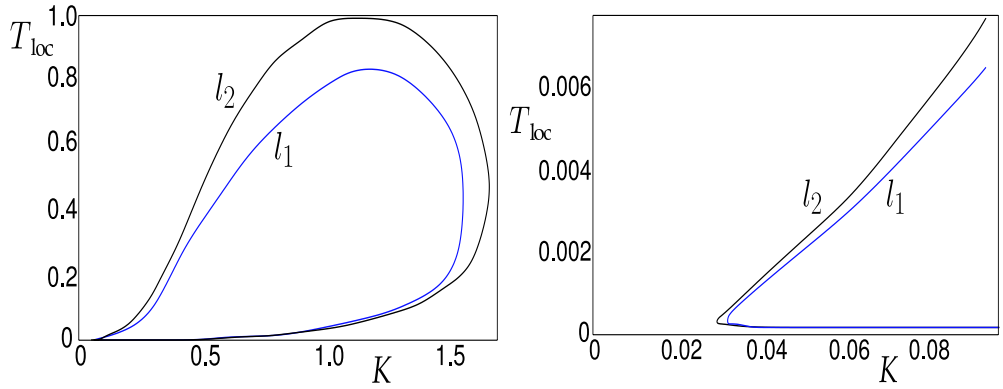


Figure 5.5: Domains of existence of non-stationary regimes in the coupling-strength $K$ and noise intensity $T_{loc}$ plane. There are no spiking states outside the inner curve $l_1$ and no oscillatory states at all outside the outer curve $l_2$. Left panel: global view; right panel: enlarged part for small values of $K$, other parameters like in fig. 5.3.

the elements feel little from one another. For $K = 0$ the mean of the ensemble ($\langle x \rangle$, $\langle y \rangle$) becomes (in the limit $N \to \infty$) identical to the temporal average of a single element (cf. chapter 3) and stops moving completely (finite $N$ leads to small

motion of the mean). If the coupling strength is too high it counteracts the noise, keeps the individual elements together, and prevents spiking.

As fig. 5.2 indicates the spiking starts abruptly for small noise intensities but the amplitude of the oscillations decays comparatively slowly for high intensities. The upper part of the curve $l_1$ is therefore somewhat arbitrarily drawn. We plotted the curve at those parameter values at which the magnitude of the oscillations $d$ equals one.

It is interesting to look at the power spectra of time series of the mean at the transition from subthreshold oscillations to spiking. Fig. 5.6 shows two typical

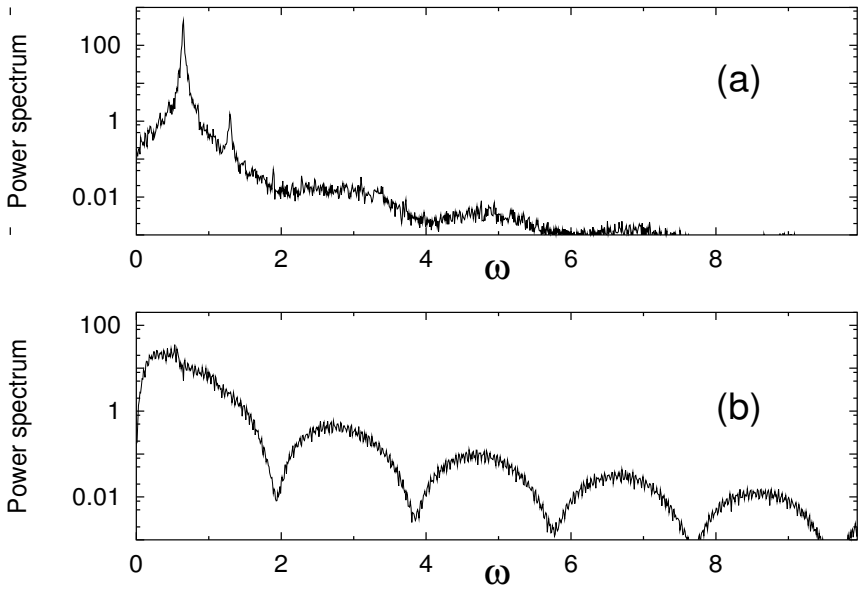


Figure 5.6: Power spectra of $\langle x \rangle$ for the subthreshold oscillation regime (upper panel, $T_{loc} = 2.71 \times 10^{-4}$) and for the spiking regime (lower panel, $T_{loc} = 2.73 \times 10^{-4}$). A strong, qualitative change can be observed with only a slight change in the noise intensity. Noisy precursors of the maxima in the spectrum which correspond to the spikes can be seen already in the small amplitude case. Other parameters: $a = 1.05$, $\epsilon = 0.01$, $K = 0.1$.

examples, one below the transition and one above. We see a drastic change in the shape of the spectrum. In the regime of subthreshold oscillations (fig. 5.6(a)) there are well-defined peaks over a noisy background. They correspond to the frequency of the small amplitude oscillations. Shortly after the transition (fig. 5.6(b)) the mean field is characterized by a broadband spectrum with deep minima. The latter correspond to the inverse recovery time of the system [96]. The peaks of the subthreshold oscillations can still be vaguely identified.

The minima in the spectrum of the spiking system (fig. 5.6(b)) can, albeit not so pronounced, already be recognized in fig. 5.6(a). They are precursors of the spiking regime [86] and are caused by the fact that the individual units of the ensemble exhibit intermittent spiking even before the transition of the mean field. Close before the threshold small clusters of such elements start to spike cooperatively, making thereby the inverse recovery time visible in the spectrum already at this stage.

Shortly below the transition to spiking of the mean the individual systems exhibit both, excitable and oscillatory behavior. Together with the mean they oscillate for some time with small amplitude. Occasionally they cross a certain threshold and undergo a large excursion in phase space just as in the excitable parameter regime. During a small oscillation of the mean its distance to this threshold also oscillates. It was shown in [74, 124] that this leads to multi-modal interspike interval distributions. The authors find imperfect phase locking between the interspike intervals and the fundamental frequency of the subthreshold oscillations.

### 5.1.2 Cumulant Dynamics

In the previous section we have seen several interesting phenomena which we now want to have a closer look at. For a more detailed analysis of the dynamics we look at the limit $N \to \infty$ and use the method of the moments dynamics (chap. 2). We therefore compute the temporal evolution of the mean values $m_x$ and $m_y$ as well as of the variances $D_x$ and $D_y$ and the covariance $D_{xy}$, all in Gaussian approximation. It is given by the set of equations:

$$\begin{aligned}
\epsilon \frac{d}{dt} m_x &= m_x - \frac{m_x^3}{3} - m_y - m_x D_x \\
\frac{d}{dt} m_y &= m_x + a \\
\epsilon \frac{d}{dt} D_x &= 2D_x(1 - D_x - m_x^2 - K) - 2D_{xy} \\
\frac{d}{dt} D_y &= 2(D_{xy} + T_{loc}) \\
\epsilon \frac{d}{dt} D_{xy} &= D_{xy}(1 - D_x - m_x^2 - K) - D_y + \epsilon D_x
\end{aligned} \tag{5.4}$$

The results of a simulation of system 5.4 with small noise intensity $T_{loc}$ are shown in fig. 5.7. For small fluctuations $T_{loc}$ there exists a stable fixed point (not shown). For increasing intensity of the noise this fixed point becomes unstable and a limit cycle with small amplitude emerges. For even stronger noise we find a period doubling of these oscillations. Further increase leads to a whole period doubling

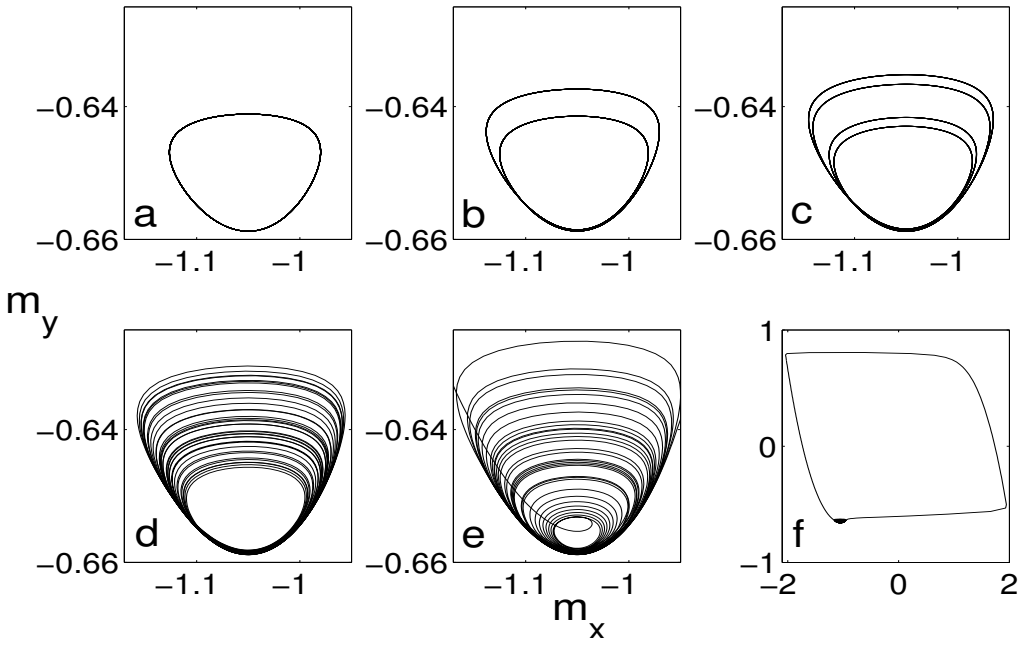


Figure 5.7: Phase space trajectories for different noise intensities. We see successive period doubling of the small amplitude oscillations until chaos emerges. Soon after, spiking starts. Note the small parameter range (from a to e): $T_{loc} = 0.00157$, 0.00158, 0.0015826, 0.001585, 0.001586; $K = 0.1$. Subplot e is an enlargement of f. Note the similarities to fig. 4.13.

cascade which culminates in chaotic dynamics. The amplitude of the chaotic oscillations is, at first, comparable to the amplitudes of the non–chaotic oscillations.

A subtle increase of the fluctuation intensity leads to a drastic but continuous increase of the amplitude of the oscillations, a phenomenon known as Canard explosion. In phase space the system moves for some part of the oscillation close to the repelling part of the slow manifold. The Canard explosion has been well studied in systems where the attractor is a limit cycle (also in the case of a single FHN system) [42, 74, 79, 124]. The peculiarity of our case is that it is not a limit cycle whose amplitude increases but a chaotic attractor as a whole.

It is especially interesting to compare fig. 5.7 to fig. 4.13 in the chapter on noise–induced excitability. The similarities are striking. Both systems share a stable fixed point, small scale limit cycles, period doubling, chaos, and even the Canard explosion of the chaotic attractor. This is especially remarkable because the two systems show little resemblance. They differ in their nonlinearity: While the FHN possesses a cubic nonlinearity the excitability model additionally possesses a quintic. The noise term in the FHN is additive, in the other one it is

multiplicative. On the other hand both systems show a clear timescale separation. We do not know what features are mandatory for a system to show this kind of complicated transition.

Let us now have a closer look at the system's phase space. The small value of $\epsilon$ is responsible for a clear timescale separation in eqs. 5.4: $m_x$, $D_x$, and $D_{xy}$ evolve on a fast timescale while $m_y$ and $D_y$ evolve on a slow one. Accordingly, there exists a two-dimensional subspace in the five-dimensional phase space which corresponds to slow motions. We call it the slow surface. In the single (uncoupled) FHN system the slow manifold is only one-dimensional (cf. chapter 3). Here, no period doubling cascade is observed. The change in the dimension of the slow manifold fits well to the observed increase of the diversity of the dynamics.

We set $\epsilon = 0$ and parameterize the slow surface by $m_x$ and $D_x$. Given arbitrary values of these two variables (only $D_x > 0$ is physically meaningful) the other three variables are determined to:

$$\begin{aligned} m_y &= m_x - m_x^3/3 - m_x D_x \\ D_{xy} &= D_x(1 - D_x - m_x^2 - K) \\ D_y &= D_x(1 - D_x - m_x^2 - K)^2 \end{aligned} \tag{5.5}$$

In order to describe the temporal evolution of the system *upon* the slow surface we have to solve the linear system:

$$\begin{aligned} (1 - D_x - m_x^2)\dot{m}_x \quad & -m_x\dot{D}_x \quad && = m_x + a \\ -4m_x D_x\dot{m}_x \quad & +(1 - 3D_x - m_x^2 - K)\dot{D}_x \quad && = D_x + \frac{T_{loc}}{1 - D_x - m_x^2 - K} \end{aligned} \tag{5.6}$$

With the solution we arrive at the dynamics for $m_x$ and $D_x$ on the slow surface:

$$\begin{aligned} \dot{m}_x &= \frac{a\ (D_x + {m_x}^2 + K - 1)\ (1 - 3\,D_x - {m_x}^2 - K)}{(D_x + {m_x}^2 + K - 1)\ (D_x\ (3D_x + K - 4) + (m_x^2 - 1)\ ({m_x}^2 + K - 1))} \\ &- \frac{m_x\left(1 + {D_x}^2 + 2\,D_x\ ({m_x}^2 + K - 1) + ({m_x}^2 + K)^2 - 2\ ({m_x}^2 - T_{loc} + K)\right)}{(D_x + {m_x}^2 + K - 1)\ (D_x\ (3D_x + K - 4) + (m_x^2 - 1)\ ({m_x}^2 + K - 1))} \\ \dot{D}_x &= \frac{-2\ (D_x + {m_x}^2 - 1)\ \left({D_x}^2 - D_x\ (1 + 2\,a\,m_x + {m_x}^2) - T_{loc}\right)}{(D_x + {m_x}^2 + K - 1)\ (D_x\ (3D_x + K - 4) + (m_x^2 - 1)\ ({m_x}^2 + K - 1))} \\ &- \frac{-2\,D_x\ (D_x - 2\,a\,m_x - {m_x}^2 - 1)\ K}{(D_x + {m_x}^2 + K - 1)\ (D_x\ (3D_x + K - 4) + (m_x^2 - 1)\ ({m_x}^2 + K - 1))} \end{aligned} \tag{5.7}$$

Stability against transversal perturbations is given for

$$(m_x^2 - 1)^2 + D_x(3D_x - 4) < K(1 - m_x^2 - D_x) \tag{5.8}$$

If inequality 5.8 is not fulfilled the surface is repelling. Fig. 5.8 shows a projection

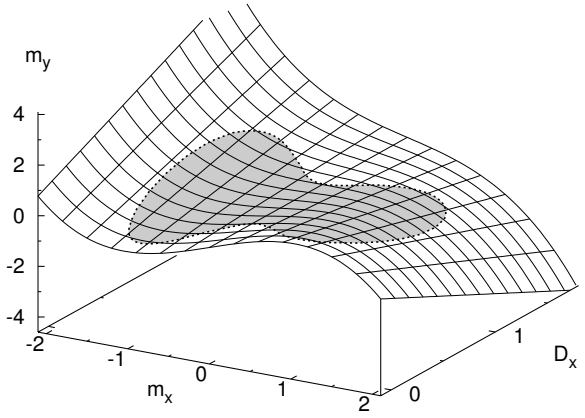


Figure 5.8: Projection of the slow surface onto the $m_x$, $m_y$, and $D_x$ space. The repelling part is plotted in gray. $K = 0.1$.

of the slow surface onto the $m_x$, $m_y$, and $D_x$ space and demonstrates the position of the repelling part.

The fixed point of the dynamical system 5.4 which we denote by a tilde over the variables can easily be computed to:

$$\begin{aligned} \tilde{m}_x &= -a \\ \tilde{m}_y &= \frac{a^3}{3} + a(\tilde{D}_x - 1) \\ \tilde{D}_x &= \frac{1 - a^2 - K}{2} + \sqrt{\frac{(1 - a^2 - K)^2}{4} + T_{loc}} \\ \tilde{D}_y &= \epsilon \tilde{D}_x + T_{loc}(a^2 + K - 1 + \tilde{D}_x) \\ \tilde{D}_{xy} &= -T_{loc} \end{aligned} \tag{5.9}$$

We have again dropped negative solutions for $\tilde{D}_x$ and $\tilde{D}_y$. We see that the steady value of $m_x$ does not depend on the noise intensity (nor on the coupling strength). This is in accordance with the results from the direct simulations of $N$ individual units.

The fixed point lies very close to the slow surface described by eq. 5.6. Only the small term $\epsilon D_x$ in the dynamical equation for $D_{xy}$ in the system 5.4 leads to a small deviation. Neglecting this difference we see that the fixed point moves on

the slow surface with a change of the parameters. With an increase of the noise intensity $T_{loc}$ from zero on it moves from the attracting to the repelling part.

An example of a system that possesses a fixed point in the repelling part of the slow surface is shown in fig. 5.9. The system moves close to the slow surface

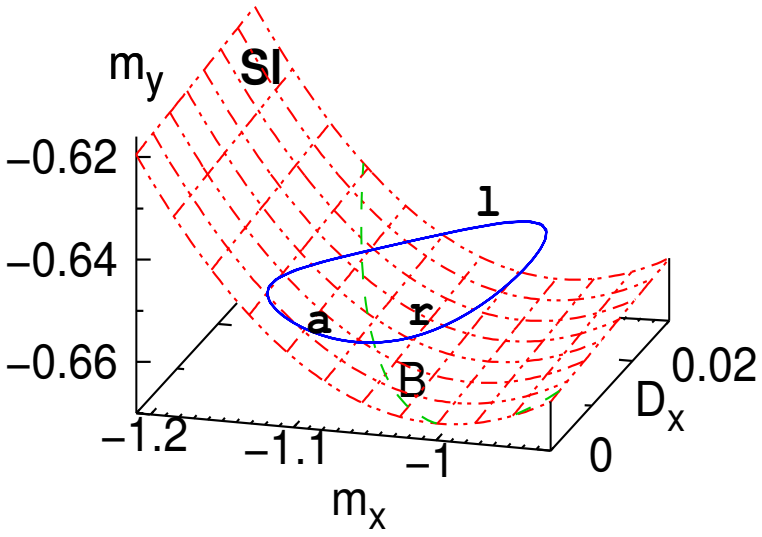


Figure 5.9: Small amplitude oscillations. The system moves along the slow surface $Sl$ (dotted grid) towards the fixed point (section "a" of the solidly plotted trajectory). This fixed point lies on the right hand side of the border $B$ which separates the attracting from the repelling part of the slow surface (left side is attracting). After entering the repelling region it moves along the slow surface for some time (section "r") then departs from it and reapproaches the slow surface at a different site of the attracting part (section "l"). Parameters: $\epsilon = 0.01$, $K = 0.1$, $T_{loc} = 0.00157$.

towards the fixed point until it hits the border of the repelling region. It then moves along the repelling part of the slow surface for some time (This effect is known as the "Canard phenomenon".), then departs from it and reapproaches it at a different site on the attracting part. From there it moves towards the fixed point again.

As can be seen from eq. 5.8 shape and location of the repelling region depend on only one parameter, namely the coupling strength $K$. Fig 5.10 depicts this region for several values of $K$. It is especially interesting to look at fig. 5.10 with the knowledge of the fixed point described by eq. 5.10. We see that the equilibrium value $\tilde{m}_x$ does not depend on the noise intensity $T_{loc}$ while $\tilde{D}_x$ is an unbounded, monotonically growing function of it. Therefore, for suitable parameter $a$ and coupling strength $K$, the fixed point moves along the vertical line $m_x = -a$ (upwards

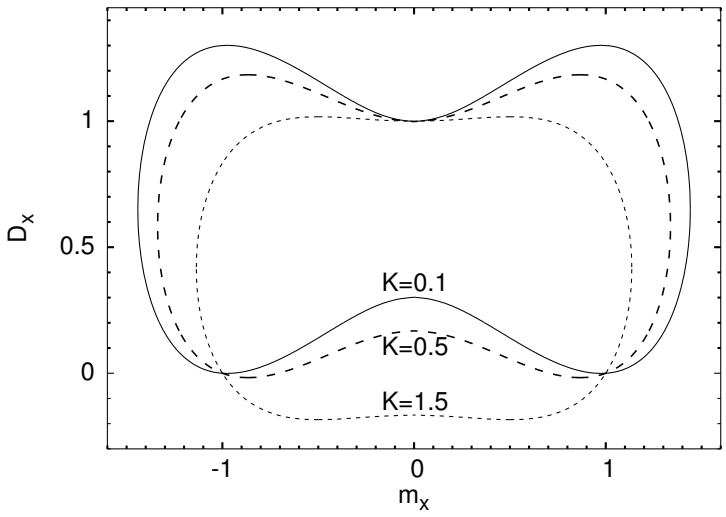


Figure 5.10: Projection of the repelling part of the slow surface onto the $m_x$–$D_x$ plane. Shape and position of this part depend on the coupling strength $K$, only. The border of the repelling region always includes the point $m_x = \pm 1$ and $D_x = 0$.

in fig. 5.10), enters the repelling region, moves further upwards and leaves the repelling region again.

At the parameter set at which the fixed point enters the repelling part of the slow surface the system exhibits an Andronov-Hopf bifurcation. In the limit $\epsilon \to 0$ this point can be evaluated analytically. It is given by the smaller one of the two roots of the equation

$$\begin{aligned} 9T_{loc}^2 + T_{loc}(16b^2 - 16 - 12b - 4K + 9bK + 2K^2) & \\ +2b(b+K)^2(2+2b+K) &= 0 \end{aligned} \tag{5.10}$$

Here we have defined: $b \equiv a^2 - 1$. For further increasing noise intensity the fixed point leaves the repelling region again and reenters the attracting one. This is again a Hopf bifurcation. The critical value is given by the larger root of eq. 5.10. Above the bifurcation it is stable again. This state is characterized by high second order moments compared to the state below the first Hopf bifurcation. This fits well to the results plotted in fig. 5.1 where we see that the individual members of the ensemble still exhibit spiking when the mean has already returned to the fixed point.

Eq. 5.10 can only be fulfilled if

$$K \leq K_0 = 2(3a^2 - 1 - 2a\sqrt{3a^2 - 3}\,) \tag{5.11}$$

Returning to the graphical interpretation we note that for $K$ smaller than $K_0$ the repelling region extends to the right hand side of the line $m_x = -1$ and the fixed point does not enter this region for whatever noise intensity.

$K_0$ is a monotonically decreasing function of $a$. Since we assume that coupling is always positive ($K > 0$) we can evaluate a critical parameter

$$a_0 = \sqrt{1 + \sqrt{\frac{4}{3}}} \approx 1.467 \tag{5.12}$$

$K_0$ is negative for $a > a_0$. Consequently there is no positive coupling strength that permits a Hopf bifurcation. In the language of fig. 5.10 this means that the left border of the repelling region as a function of $a$ is bounded to the left hand side. For $a > a_0$ the vertical line $m_x = a$ does not intersect with the repelling region for any coupling strength.

The bifurcation diagram for the Hopf bifurcation is plotted in fig. 5.11 in the

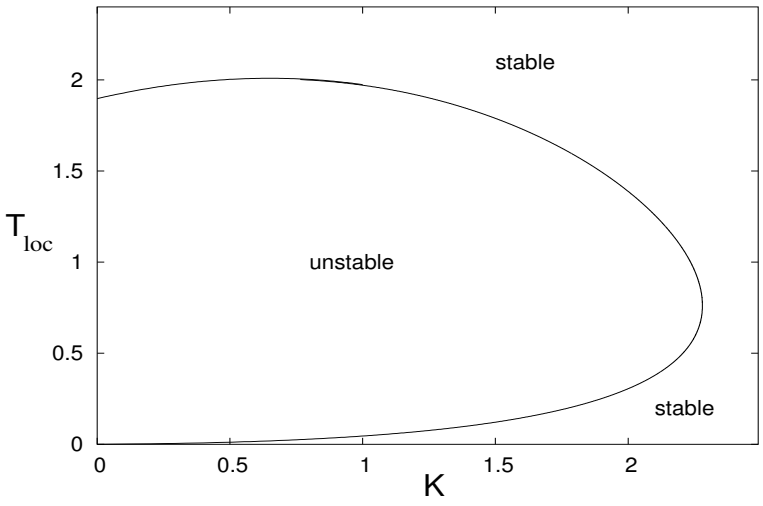


Figure 5.11: Hopf bifurcation as obtained from eq. 5.10. Comparison with fig. 5.5 shows good quantitative agreement for high coupling strength. Parameters: $a = 1.05$, $\epsilon = 0.01$.

parameter plane of noise intensity and coupling strength. If we compare this result to the results from the Langevin simulations that are shown in fig. 5.5 we see good quantitative matching for high coupling strength $K$. The highest $K$–value at which oscillations occur differs about ten percent for the two methods. For low $K$ the agreement is diminished. For $K = 0$ the moment dynamics predict oscillations of the mean $m_x$. This is a weakness of the approximation since the mean $\langle x \rangle$ of the uncoupled stochastic ensemble is clearly time-independent.

The sudden increase in the oscillation amplitude is associated with a qualitative change in the power spectrum of $m_x$ as demonstrated in Fig. 5.12. In the regime

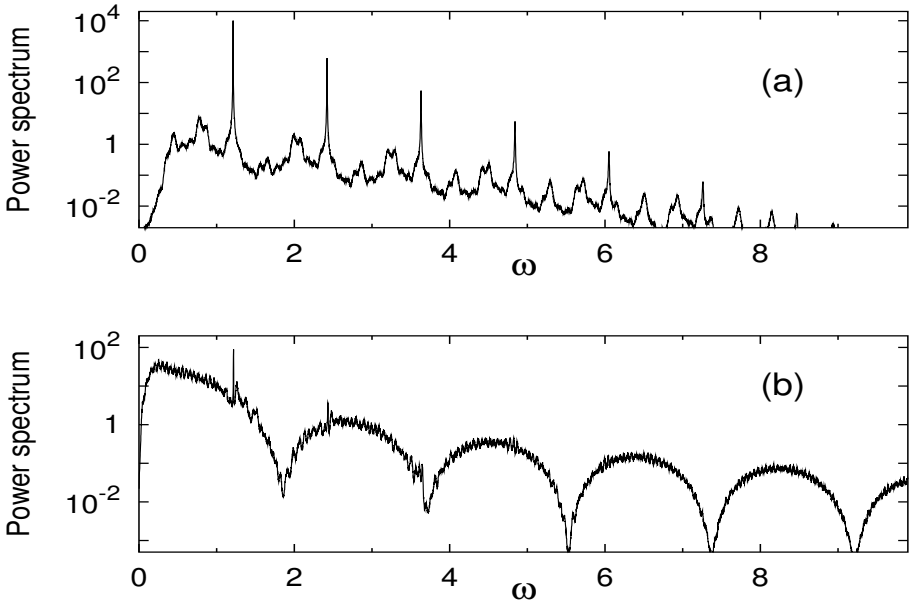


Figure 5.12: Power spectra of a time series from a system in the subthreshold oscillation regime (a) and from a system in the spiking regime (b). The spectra show the same qualitative change as obtained in the Langevin simulations. Parameters: $a = 1.05$, $K = 0.1$, $\epsilon = 0.01$. (a) $T_{loc}$=0.001585, (b) $T_{loc}$=0.001586.

below the Canard explosion, clear peaks are visible. Above broad bands with prominent dips can be seen. Note the agreement with the Langevin simulations (fig. 5.6).

In a very small parameter regime after the increase of the oscillation amplitudes the dynamics are still chaotic. A large outburst (spikes) is followed by several small amplitude oscillations. The number of these subthreshold oscillations is irregular. A further increase of the fluctuations leads to a regularization of the interspike intervals. At first the number of subthreshold oscillations is large, but it gradually decreases with increasing noise intensity until the system exhibits nonintermittent spiking. This is shown in fig. 5.13. It is a kind of an "inverse period adding" sequence: $n$ subthreshold oscillations between two subsequent spikes are replaced by $n-1$, which is replaced by $n-2$ and so on. An even closer look yields that there are even more complex series. We find, e.g., regions where there is one subthreshold oscillation every seven spikes (fig. 5.13 (f)).

As stated above the fixed point regains stability at high noise intensities. It is then the only stable attractor of the system. That means that the amplitude

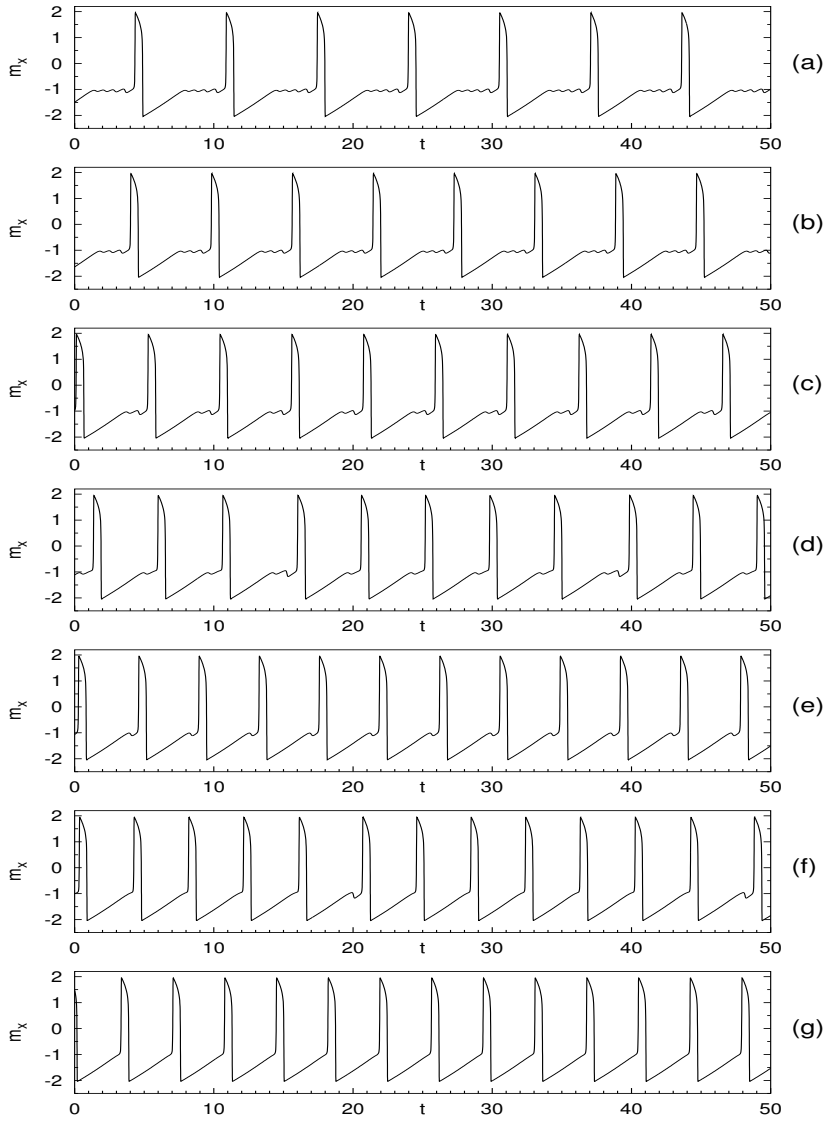


Figure 5.13: Timeseries of $m_x$. The interspike intervals gradually decrease until nonintermittent spiking occurs. Parameters: $K = 0.1$ $\epsilon = 0.01$, $a = 1.05$, from top to bottom: $T_{loc} = 0.00168$ (a), 0.00172 (b), 0.00185 (c), 0.0018569 (d), 0.00220 (e), 0.0023105 (f), 0.0024 (g).

of the oscillations decreases to zero again. In order to characterize this amplitude we define similarly to the previous section the magnitude of the oscillations $d = max(m_x) - min(m_x)$. $max(m_x)$ and $min(m_x)$ are the extrema of a timeseries much longer than a typical oscillation time. The dependence of $d$ on the noise

intensity $T_{loc}$ is demonstrated in fig. 5.14. We find a complex behavior. Shape

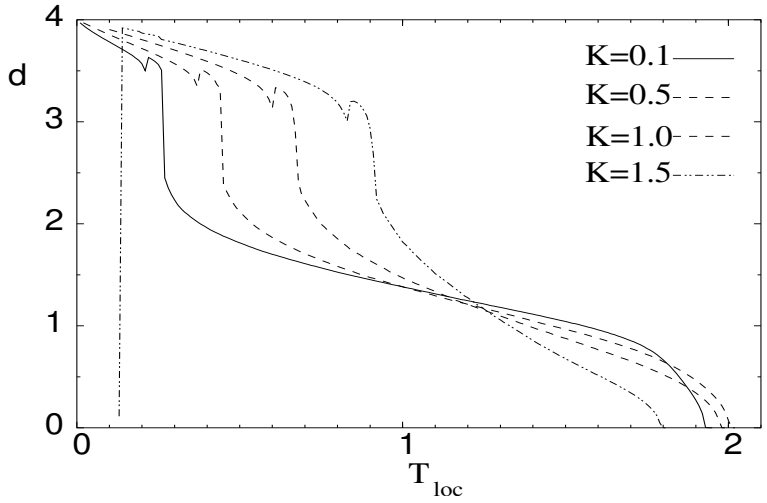


Figure 5.14: Diameter of oscillations $d$ versus noise intensity $T_{loc}$. We find a very complex, non-monotonous dependency. The location of the curve depends on the noise intensity. Parameters: $\epsilon = 0.01$, $a = 1.05$.

and location of the curve depend on the coupling strength $K$. All curves have in common that initially the amplitude of the oscillations quickly increases with increasing fluctuations, then slowly decreases, exhibits a bump, quickly decreases by a factor of approximately two, then slowly and almost linearly further decreases, and finally decays. The final decay is governed by a square root law. Here the system undergoes a second Hopf bifurcation.

The quick decrease of the amplitude with increasing noise intensity reminds us of the Canard explosion for small fluctuations. It is less dramatic, though. This decrease is preceeded by a bump (that is the narrow region after the first slow decay in which $d$ shows non-monotonous behavior) that we already know from the Langevin simulations.

Phase plots of system 5.4 at the corresponding parameter values reveal another period doubling bifurcation at the local minimum of $d$ as a function of $T_{loc}$. In fact this is the beginning of another period doubling cascade. We also find another region in which the dynamics turns chaotic again. In this case the timeseries of $m_x$ does not include small amplitude oscillations as it did in the scenario described above. The amplitudes of the oscillations differ only little.

In the course of the decrease of $d$ the oscillations turn regular again, and an inverse period doubling cascade occurs. It ends when the simple periodic orbit is restored.

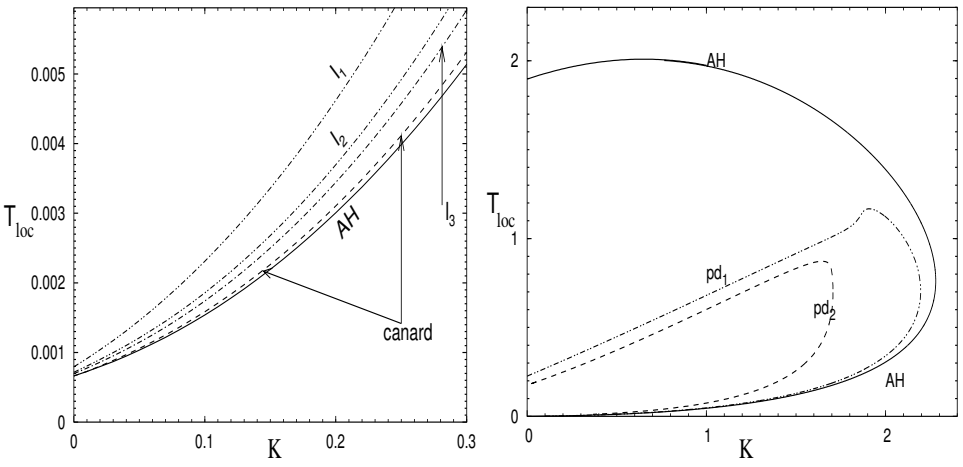


Figure 5.15: Period doubling and Hopf bifurcations. (a) enlarged part at low coupling strength $K$ and noise intensity $T_{loc}$. (b) global view of selected bifurcations. AH: Andronov-Hopf bifurcation; $l_n$: onset of regime with $n$ subthreshold oscillations between two spikes ($l_0$: onset of non-intermittent spiking). Parameters: $\epsilon = 0.01$, $a = 1.05$.

The location of these bifurcations is demonstrated in fig. 5.15. We see that the period doubling bifurcation we have just discussed is the upper branch of the bifurcation that was described in the previous section. We also note that there exist a parameter region with coupling strength $1.7 < K < 2.2$ in which the system undergoes for increasing noise only two period doubling cascades, one of them is "normal" and one inverse. Here the system does not exhibit simple (period one) spiking.

## 5.2 Introducing Correlations - Local and Global Noise

In the previous part of this chapter we have applied noise without spatial correlations. In this chapter we will investigate their influence [106]. We therefore no longer neglect the global noise term $\eta(t)$ in eq. 5.1. Instead we leave $T_{all} = T_{glob} + T_{loc}$ constant and vary the ratio between the local and the global noise intensity.

The introduction of correlations has implications on the cumulant dynamics. The system of equations 5.4 is non longer deterministic but becomes stochastic itself. This manifests itself in a change of the equation for the temporal evolution

of the variable $m_y$ (all other equations remain the same as before):

$$\dot{m}_y = m_x + a + \eta(t) \tag{5.13}$$

with the Gaussian white (in time) fluctuating term $\eta(t)$ with characteristics described by eq. 5.2. The fluctuations of the mean are thus only due to $T_{glob}$. A change in $T_{loc}$ changes the deterministic part of the cumulant dynamics.

We study the nullcline for $m_x$ and $m_y$ for vanishing global noise in fig. 5.16. It shows a projection onto the two-dimensional subspace of the five-dimensional

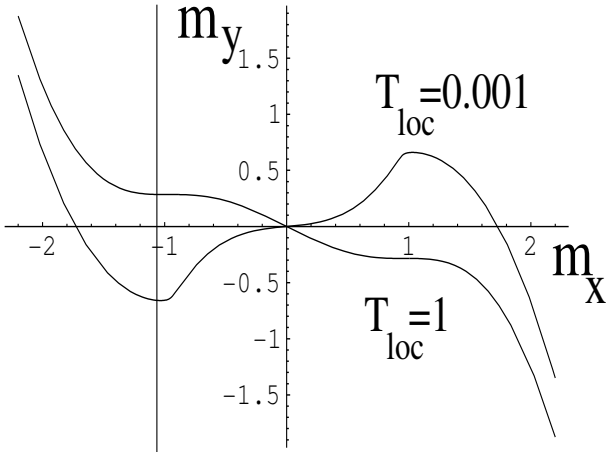


Figure 5.16: Left: Nullclines for the cumulant dynamics in the $m_x$ and $m_y$ subspace for different values of the local noise intensity $T_{loc}$. The linear nullcline ($\dot{m}_y = 0$; vertical line at $x = -1.05$) is not affected by the noise. The cubic nullcline ($\dot{m}_x = 0$) of the cumulant dynamics resembles that of the single FHN (cf. fig. 3.2) for low noise intensity but changes dramatically for higher noise. Parameters: $K = 0.1$, $a = 1.05$.

phase space of the system for steady second order cumulants $D_x$ and $D_y$.

For vanishing local noise the nullclines resemble those of the single deterministic FHN that we have shown in fig. 3.2. For increasing noise the situation changes dramatically: The curve loses its extrema and falls monotonically. We therefore guess that for low noise the stochastic moment equations behave similarly to a single FHN system. Indeed, the cumulant dynamics eq. 5.4 together with eq. 5.13 form a five-dimensional excitable system. The change in the dynamics that results from a decrease of $T_{loc}$ is small compared to that from an increase of $T_{loc}$. We will see below that this leads to an effect similar to the well known coherence resonance.

In fig. 5.17 we show timeseries of $m_x$. The intensity $T_{all}$ is chosen such that

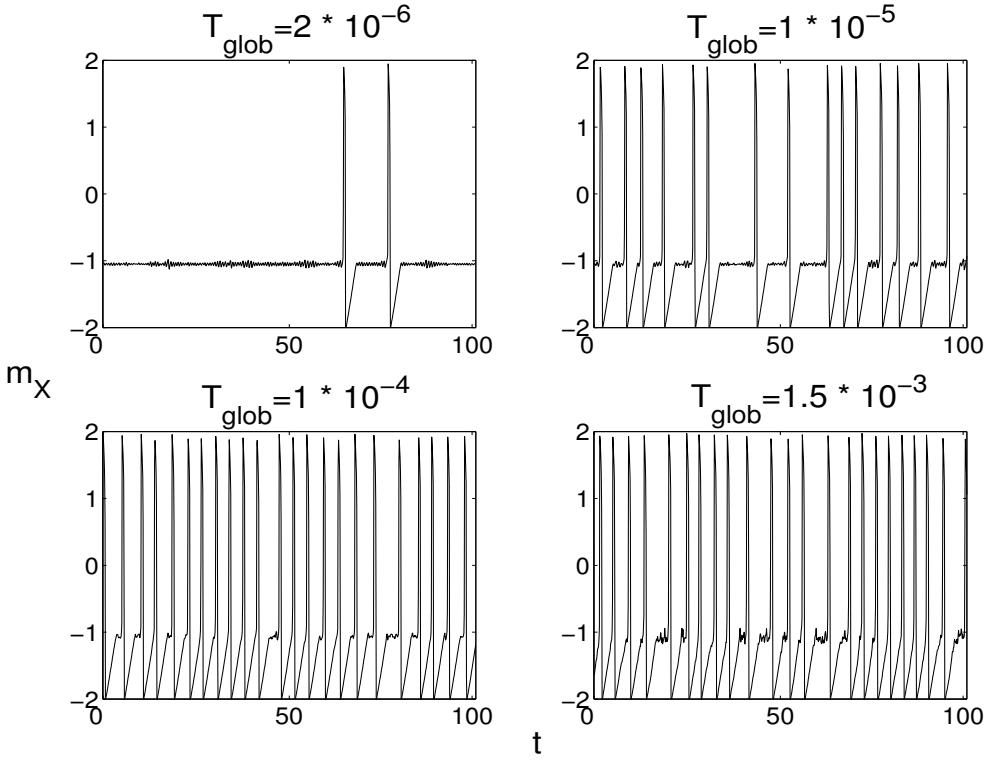


Figure 5.17: Timeseries for different values of local and global noise intensity. The sum of the intensities $T_{all} = T_{glob} + T_{loc}$ is kept constant. The ensemble starts spiking for increasing correlations. The coefficient of variation is plotted in fig. 5.18. Parameters: $K = 0.1$, $T_{all} = 0.0015$.

for purely local noise ($T_{glob} = 0$, $T_{loc} = T_{all}$) the system is close before the onset of small amplitude equations but the fixed point is still stable. For increasing correlations $m_x$ starts spiking. We see that for higher noise the intervals between two subsequent spikes decrease and at the same time the spiking becomes more regular.

As a measure for the regularity of oscillations we have introduced the coefficient of variation $R$ in eq. 3.12. We use it here as well. For the results presented in fig. 5.18 we used a sample timeseries of length $10^4$. We show $R$ plotted versus the global noise intensity $T_{glob}$. An increase of $T_{glob}$ means at the same time a decrease of $T_{loc}$ since again we left the sum of the noise intensities $T_{all}$ constant. This procedure is repeated for several values of the global noise intensity $T_{all}$.

For all runs we see a pronounced minimum of the coefficient of variation $R$. The lower the value of $T_{all}$ the deeper is the minimum. This behavior resembles coherence resonance. The difference to our case is that we do not find maximal

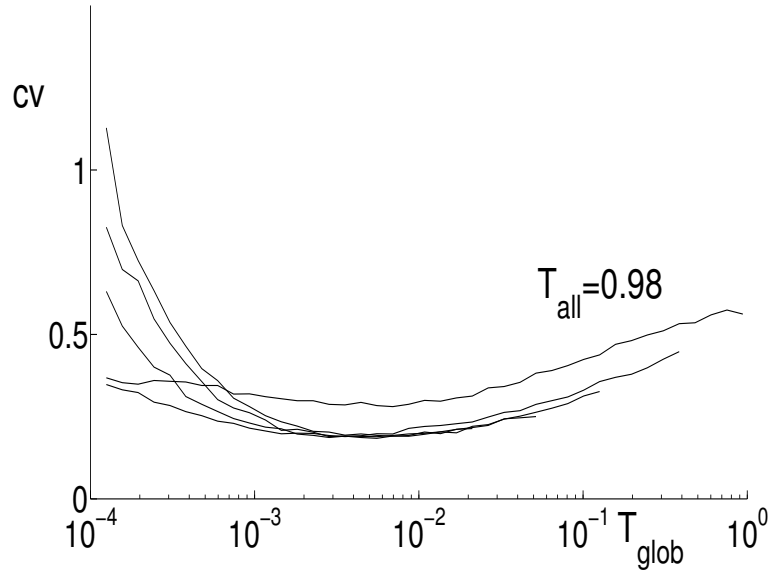


Figure 5.18: Coefficient of variation versus global noise intensity. The total intensity $T_{all} = T_{glob} + T_{loc}$ is left constant. Plots for different $T_{all}$, starting with $T_{all} = 0.98$ (upper curve) and decreasing by a factor of 2.5 per successive curve down to $T_{all} = 0.0625$, are shown. For purely local fluctuations spiking starts at $T_{loc} = 0.65$. Parameter: $\epsilon = 0.01$, $a = 1.05$, $K = 2.2$.

coherence for a certain finite nonzero noise intensity but for a finite nonzero ratio between local and global noise.

In the simulations we fixed the sum of global and local noise intensity $T_{all} = T_{glob} + T_{loc}$ for each element of the ensemble. Nevertheless the behavior of the system changes drastically when changing their ratio. Hence the system provides a feedback-less detector for global signals. The reason for this lies in the different scaling of the noise sources. The overall noise acting on the ensemble is given by

$$\frac{1}{N^2}\sum_{i,j=1}^{N}\langle\zeta_i(t_1)\zeta_j(t_2)\rangle = \left(\frac{2}{N}T_{loc} + 2T_{glob}\right)\delta(t_1 - t_2) \tag{5.14}$$

We see that $T_{loc}$ and $T_{glob}$ scale differently with $N$. Due to the correlation of the fluctuations an increase of the global component yields an effective growth of the noise in the ensemble despite the decrease of the local component.

## 5.3 Summary

We have investigated a globally coupled ensemble with FitzHugh-Nagumo kinetics under the influence of additive noise. The noise intensity serves as a new control parameter as compared to the deterministic equations. For purely uncorrelated noise we have found a diverse sequence of different dynamical regimes when varying this parameter. To distinguish these different states we used the mean of the ensemble as order parameter. A numerical simulation of the Langevin dynamics yielded stationary states for the mean in the limit of both, high and low noise intensities. In between we found hints of small amplitude oscillations and a chaotic regime before a Canard explosion leads to spiking.

We have supported the knowledge of the system that we obtained from the Langevin simulations by investigations of the cumulant dynamics of the system. We have studied them in Gaussian approximation. It showed that the extension of the chaotic attractor that the results from the Langevin simulations hinted at, increases abruptly resembling the well-known Canard explosion of limit cycles. It also revealed another period doubling sequence and another chaotic attractor with large amplitudes.

The quantitative agreement between the Langevin simulations and the Gaussian approximation is good for high coupling strength but significantly decreases for low coupling. For vanishing coupling the cumulant dynamics, in contradiction to the Langevin simulations, even predict oscillations of the mean in a wide range of noise intensities. Unfortunately the dynamics is in the strong coupling regime less interesting because it is less complex.

It is especially interesting to note that a large part of the dynamic sequence described above, namely the stable fixed point followed by small amplitude oscillations, period doubling, chaos, Canard explosion of the chaotic attractor, and regularization of intermittent oscillations appears in a very different dynamical ensemble, too (chapter 4). The systems have different highest powers in their nonlinearities. Moreover, one is subject to additive, one to multiplicative noise. There obviously exists a class of systems showing this behavior. It is still an open question which "ingredients" are necessary for a system to exhibit this dynamic sequence.

We have performed additional simulations where the noise term was not placed in the inhibitor but in the activator dynamics. The dynamical behavior was similar to the described case but we did not find the Canard explosion of the chaotic attractor.

We have also investigated the influence of correlation on the dynamics. The sum of two noise sources, one local and one global was kept constant but their ratio was varied. This leads to changed spiking behavior. We found a coherence resonance-like like phenomenon, namely a minimum in the coefficient of variation

for a certain finite nonzero ratio.

# Chapter 6

# Pattern Formation in Dichotomously Driven, Locally Coupled FitzHugh–Nagumo Elements

In this chapter we introduce a spatial structure into our system. We investigate 1- and 2-d systems with diffusive coupling. The local dynamics are again excitable and obey FitzHugh–Nagumo kinetics. We apply additive dichotomous fluctuations to the system which vary in space, in time, or in both. In a series of recent papers [19–21, 23] the possibility of the formation of diffusion-induced (also called Turing) patterns by dichotomous fluctuations has been demonstrated. In all cases the fluctuations lead to one of two dynamical states each of which does not support pattern formation but possesses a pattern-free steady state, only. It is the interplay between them that leads to the creation of structures. In the aforementioned works the authors use models with either multiplicative noise or they switched between two distinct dynamics each having its own state dependency.

We start off by giving the general ideas of the diffusion induced instability (sec. 6.1).

We will treat the case of dichotomous fluctuations varying only in time in section 6.3 and describe a new mechanism for the formation of standing Turing-like structures. We use a nonlinear map approach to investigate multi-stability of the extended system.

In section 6.4 we investigate the opposite limit namely we study frozen dichotomous disorder. We show that an increase of the spatial correlations can lead to pattern formation.

In the case of dichotomous fluctuations varying in both space and time we did not find qualitatively new effects. We discuss the quantitative influence of these fluctuation briefly in section 6.5 where we also draw conclusions.

## 6.1 The Turing Instability

The diffusion induced or Turing [120] instability arises in extended nonlinear systems when a homogeneous steady state is destabilized by diffusion. In other words for vanishing diffusion constants the steady state is stable but it is destabilized for proper (nonzero) values. Let us consider the following dynamical system:

$$\dot{\mathbf{x}} = \mathbf{F}(\mathbf{x}) + \mathbf{D}\Delta\mathbf{x} \tag{6.1}$$

where $x = x(r, t)$ depends on space and time.

The stability for vanishing diffusion is calculated by linearizing the corresponding dynamical system:

$$\dot{\delta}_{\mathbf{x}} = \mathbf{J}\delta\mathbf{x} \tag{6.2}$$

where $\mathbf{J}$ is the Jacobian of the individual (uncoupled) system . We use the ansatz

$$\delta\mathbf{x} = \mathbf{A}e^{\gamma t - i\mathbf{kr}} \tag{6.3}$$

for the modes with wave vector $k$ of small deviations from the steady state ($r$ is the space variable). For nonzero diffusion constants eq. 6.2 becomes

$$\dot{\delta}_{\mathbf{x}} = \left(\mathbf{J} - k^2\mathbf{D}\right)\delta\mathbf{x} \tag{6.4}$$

where $\mathbf{D}$ is the matrix of the diffusion constants. The eigenvalues of the linearized system $\gamma$ that determine the stability of the homogeneous solution now depend on the diffusion constants and the wave vector $k$. If the largest real part is larger than zero for a nonzero wave number $k$ we speak of a Turing instability.

In what follows we want to give the conditions for the instability for a two-variable system. We denote with $J_{i,j}$, $(i, j \in \{1, 2\})$, the elements of the Jacobian $\mathbf{J}$. Let us assume that $J_{1,1} > 0$ and $J_{2,2} < 0$, i.e. variable 1 acts as destabilizer and variable 2 as stabilizer (This holds for the FHN with the activator $x$ as variable 1 and the inhibitor $y$ as variable 2). The conditions for the Turing instability then are:

$$0 > J_{1,1} + J_{2,2} \tag{6.5a}$$

$$0 < J_{1,1}J2,2 - J1,2J_{2,1} \tag{6.5b}$$

$$D_1 J_{2,2} + D_2 J1,1 \geq 2\left[D_1 D_2 (J_{1,1}J_{2,2} - J_{1,2}J_{2,1})\right] \tag{6.5c}$$

The effect of the diffusion induced instability is visualized in fig. 6.1 for a 1-d two-variable activator-inhibitor system. Assume that the system initially is in a homogeneous state (denoted by the solid straight line). A small inhomogeneity of critical wavelength is depicted as solid line for the activator and as dashed line for the inhibitor. In the uncoupled case the growth of the activator is prevented by the

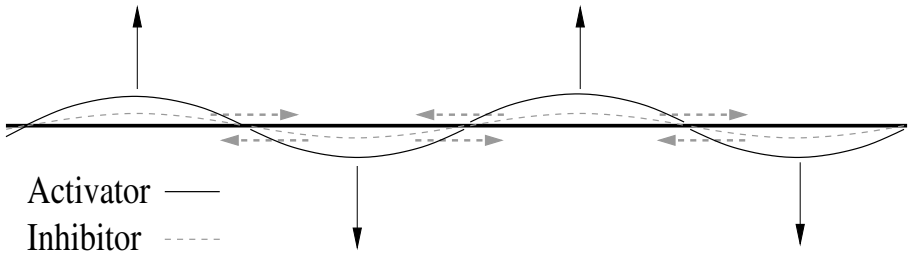


Figure 6.1: Diffusion induced instability. The strong diffusion of the inhibitor leads to suppressed inhibition.

inhibitor. The steady state is stable. For proper diffusion constants the inhibitor (dashed gray lines) diffuses so quickly (horizontal arrows) that it cannot suppress the activator which then grows (vertical arrows) to form an inhomogeneous structure. In the case of the FHN the nonlinearity prevents unlimited growth.

## 6.2 The Dichotomously Driven FHN System

We study an extended system with FHN kinetics with additive noise. It obeys the equations:

$$\begin{aligned} \dot{x_i} &= x_i - x_i^3 - y_i + D_x \Delta x_i \\ \dot{y_i} &= \epsilon \left( x_i - a y_i - I_i(t) \right) + D_y \Delta y_i \end{aligned} \tag{6.6}$$

Here $\Delta$ is the Laplace operator. We fix the value of $\epsilon$ to 0.05 and that of $a$ to 1.475. The latter is chosen from a small parameter range for which the phenomena that we describe in this chapter occur. The coupling (diffusion) constants were set to $D_x = 0.02$ and $D_y = 5.0$. If not explicitely mentioned otherwise these parameter values were used throughout the chapter. $I_i(t)$ constitutes a random telegraph process which takes one of the two values $d$ and $-d$ (We fix $d = 0.2$ throughout the chapter.). We call the rate of the switching between the two states $\gamma$. The correlation function of the process is given by:

$$\langle I_i(t_1) I_j(t_2) \rangle = d^2 e^{-2\gamma\tau} K(i,j) \tag{6.7}$$

where $K(i,j)$ is the spatial correlation function between the different sites in the array and $\tau = |t_2 - t_1|$.

Let us have a look at the parameter regime we are in. We are interested in the dynamics of an individual unit of our array and set $D_x = D_y = 0$. If we additionally fix the value of $I(t)$ to say $d$, the dynamics of the system become deterministic.

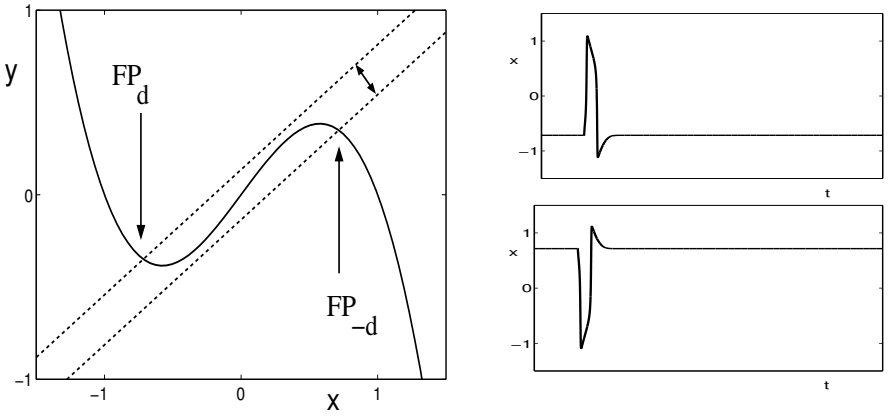


Figure 6.2: Nullclines of a single FHN-System. Solid line: cubic nullcline obtained by setting $\dot{x} = 0$, dashed lines: linear nullcline obtained by setting $\dot{y} = 0$ for the two different realizations of the dichotomic driving $I(t)$. The $FP_i$ label the different fixed points. The right hand side shows the dynamics of $x$ for $d = 0.2$ (upper plot) and $d = -0.2$ (lower plot) where a superthreshold perturbation has been added and a spike provoked. The dynamics are equivalent but have a symmetry around $x = 0$.

For the parameter values we have chosen the system is in the excitable regime. Due to the symmetry under the transformations $x \to -x$ and $y \to -y$ the system is in another excitable regime with equivalent dynamics for $I(t) = -d$. A graphical representation is given in fig. We see that the switching between the two states of the random telegraph process $I(t)$ entails transitions between two excitable dynamical regimes. They are associated with either the fixed point located on the left or on the right branch of the cubic nullcline.

## 6.3 Global Alterations

In this chapter we assume a spatially uniform signal, i.e. $K(i, j) = 1$. We thus apply global dichotomous switching ($I_i(t) = I(t)$). We denote by $\dot{\mathbf{x}}_{\pm d} = \binom{\dot{x}}{\dot{y}_{\pm d}}$ the dynamics of eq. 6.6 with $\dot{y}$ given by the second equation with $I(t) = \pm d$. The corresponding fixed points are called $\mathbf{x}_{0,+d}$ and $\mathbf{x}_{0,-d}$. $\dot{\mathbf{x}}_{det}$ stands for the deterministic dynamics arising without driving, i.e. for $I(t) = 0$. To gain insight into the impact of the dichotomous switching process on the behavior of the extended system we initialize it in the dynamical regime $\dot{\mathbf{x}}_{+d}$ with initial conditions determined by $\mathbf{x}_{0,+d}$. In real space this corresponds to a spatially homogeneous

state. In our numerical simulations we add Gaussian white noise of intensity $10^{-6}$ (remember that d is of order $10^{-1}$) to the $y$–variable in order to provide small inhomogeneities. In phase space this is expressed by a set of narrowly distributed points that is located near the fixed point $\mathbf{x}_{0,+d}$ (Hereafter we refer to this set of points with coordinates $(x(t), y(t))$ as the cloud.). Despite its extension in phase space the cloud still represents a virtually homogeneous state in real space.

### 6.3.1 Low Switching Rates

For very low switching rate $\gamma$ (compared to the inverse of the typical time for the dynamics on the nullclines) the whole cloud stays close to the fixed point for a very long time. The real space pattern is homogeneous.

Once a switching $I(t) = d \rightarrow I(t) = -d$ occurs the cloud leaves the fixed point for $\mathbf{x}_{0,-d}$ where it then remains captured until the next switching ($I(t) = -d \rightarrow I(t) = d$) occurs. In real space a homogeneous pattern, although with alternating values of $x$ and $y$ remains.

### 6.3.2 Intermediate Switching Rates

For higher switching rates we observe a different behavior: After some passage of the complete cloud back and forth between $\mathbf{x}_{0,-d}$ and $\mathbf{x}_{0,-d}$ spatial structures form. This is illustrated in Figs. 6.3 and 6.4.

The patterns are the product of a switching of the random telegraph process just at the moment when the cloud has begun to cross the excitation threshold. (Note that for the coupled dynamics there is no common excitation threshold valid for all units because whether a system is excited or not depends not only on its own state but also on that of its neighbors.) Some individual units that are already beyond the threshold get excited via a swift transition to the left outer branch of the cubic nullcline. The rest of the units returns to the nearby fixed point at the right outer branch. Due to the strong inhibitory coupling (vertical direction) the units on the left branch do not move along the trajectory of a single (uncoupled) system back to the right branch (c.f. sec. 3.1) but get trapped.

The individual systems that are trapped together are located close to each other in real space. This is a consequence of the local coupling. In real space a large-amplitude spatial inhomogeneity (hump) is formed. It is a well known solution in excitable systems [53, 88]. This hump is stable with respect to small perturbations [100]. The position on the lattice where the hump appears is arbitrary since it depends on that part of the randomly distributed units in the cloud that is beyond the excitation threshold at the moment of the switching.

We call such a spatial inhomogeneity a *nucleus*. We stress that a nucleus is extremely robust, that means neither its shape nor its position in real space

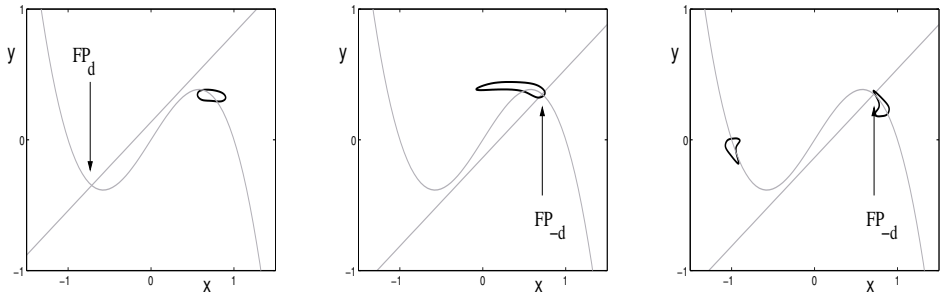


Figure 6.3: Development of stationary patterns for medium switching rates - phase space. The system with small inhomogeneities (indicated by a cloud) is initially distributed around one of the fixed point. Once switching occurs (left panel) the cloud starts to move to the second fixed point. If a second switching occurs just as the cloud is quickly passing from the left to the right (middle panel) it can be split into two. The second cloud then does not return to the fixed point of the deterministic system but moves to the other side where it stays. A spatial structure is formed (cf. fig. 6.4, $t = 58$).

is (in a good approximation) affected by further switchings. The homogeneous regions that are far from the nucleus at first feel little of it. At each further switching they behave as before, i.e. the individual systems move from one fixed point to the other and back. In the regions close to the inhomogeneous region something else happens: With each consecutive switching a new layer adjacent to the inhomogeneity is formed as is illustrated in fig. 6.4. In other words with each switching the inhomogeneous region grows at the expense of the homogeneous region. This formation process goes on and hump by hump is added until the inhomogeneous region covers the whole space. Notice the slight deviations in the width of the individual humps just after their creation. It takes diffusion a much longer time to render the pattern regular than it took the pattern to be generated (right lower panel in fig. 6.4).

Here we want to mention that this kind of growth of the inhomogeneous pattern at the boundary layer is due to our choice of parameters. We have performed simulations with different parameter sets and found that it is also possible to add not only one half of a hump at each switching but also three, five, and more halves (The parameter range for adding several layers simultaneously is very small). This can for example be achieved by a change of the intensity $d$ of the fluctuations. By varying the same parameter it is also possible to subtract half a hump with each switching (see fig. 6.5). Moreover, a change in the diffusion constants can double the number of humps in the system (fig. 6.6). This *multiplier* works only

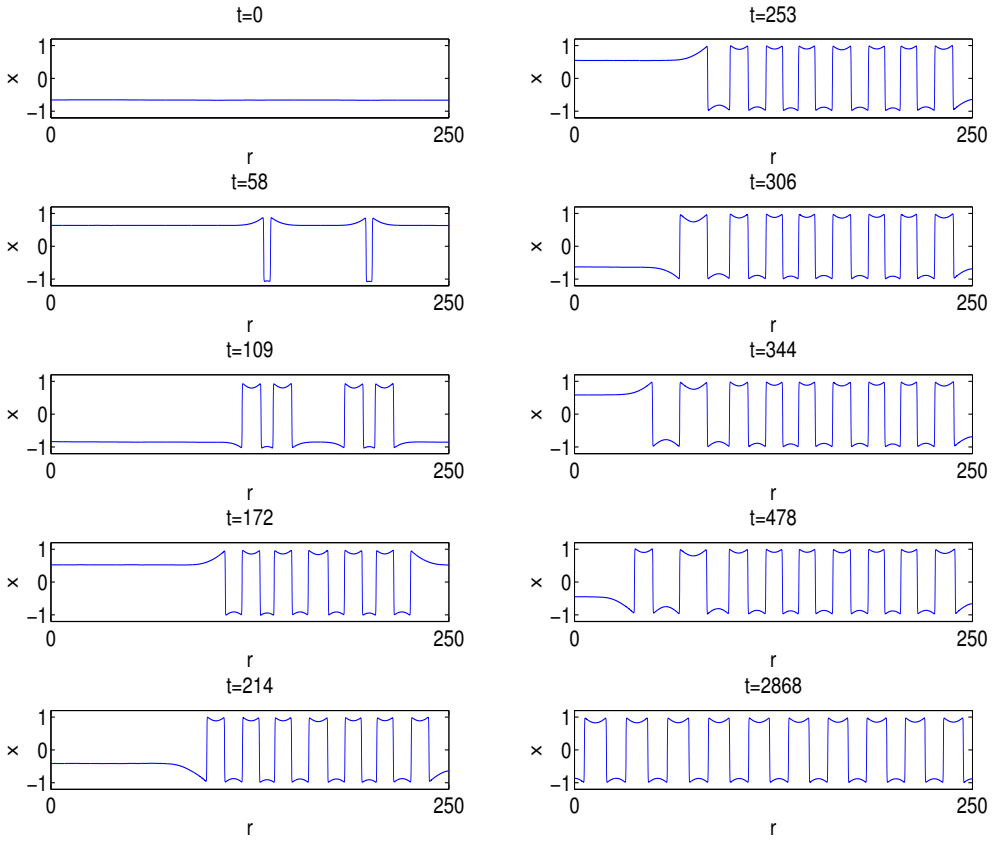


Figure 6.4: Development of stationary patterns for medium switching rates - real space. After the first nuclei are formed every movement of the homogeneous part of the cloud from one fixed point to the other adds a new layer at either side of the nucleus. After a long time a very regular structure is formed. The time is given above each picture. The $y$–variable (not shown) oscillates with equal period but small amplitude [62]. No-flux boundary conditions are used. The lattice constant is 0.05. Other parameter: $a = 1.475$, $\epsilon = 0.05$, $D_x = 0.02$, $D_y = 5.0$, $d = 0.2$.

for small $\gamma$ because immediately after the multiplication the distance between two consecutive humps is very small. No new humps fit in between. The time until diffusion has restored the stable distance between them is large. During this time the multiplier does not work. Notice that in contrast to the case treated in fig. 6.4 the pattern is not symmetric with respect to $x \to -x$. Let us call the width of a hump $l_h$ (We consider the thin parts as humps. In an infinitely extended regular pattern this choice is arbitrary.) and the distance between two neighboring humps $\Delta_h$. $\Delta_h$ must roughly increase to three times $l_h$ before a new multiplication can be performed.

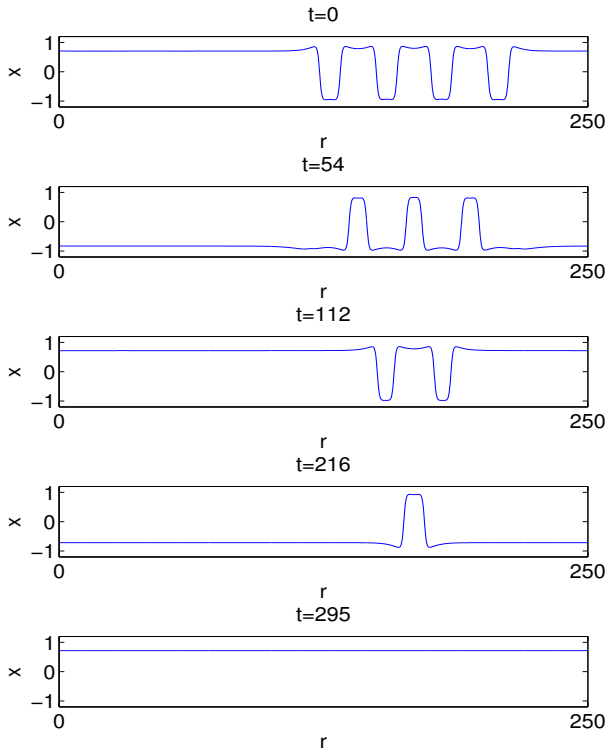


Figure 6.5: Depending on the parameter values the number of humps can also be decreased ($D_x = 0.9$). Other parameters as throughout the chapter. Snapshots shortly after each switching are shown.

The emergence of patterns from the homogeneous background can be understood by the features of the corresponding stationary system:

$$\begin{aligned} 0 &= x_i - x_i^3 - y_i + D_x \frac{x_{i-1} - 2x_i + x_{i+1}}{\Delta r^2} \\ 0 &= \epsilon(x_i - a y_i + d) + D_y \frac{y_{i-1} - 2y_i + y_{i+1}}{\Delta r^2} \end{aligned} \tag{6.8}$$

For the following investigations we set the lattice spacing $\Delta r$ equal to one.

Following [49, 50] eq. (6.8) can be cast into a four dimensional nonlinear map form:

$$\begin{aligned} s_{n+1} &= \frac{1}{D_x}\left(-s_n + s_n^3 + u_n\right) + 2s_n - t_n \\ t_{n+1} &= s_n \\ u_{n+1} &= \frac{\epsilon}{D_y}\left(s_n - a u_n + d\right) + 2u_n - v_n \\ v_{n+1} &= u_n \end{aligned} \tag{6.9}$$

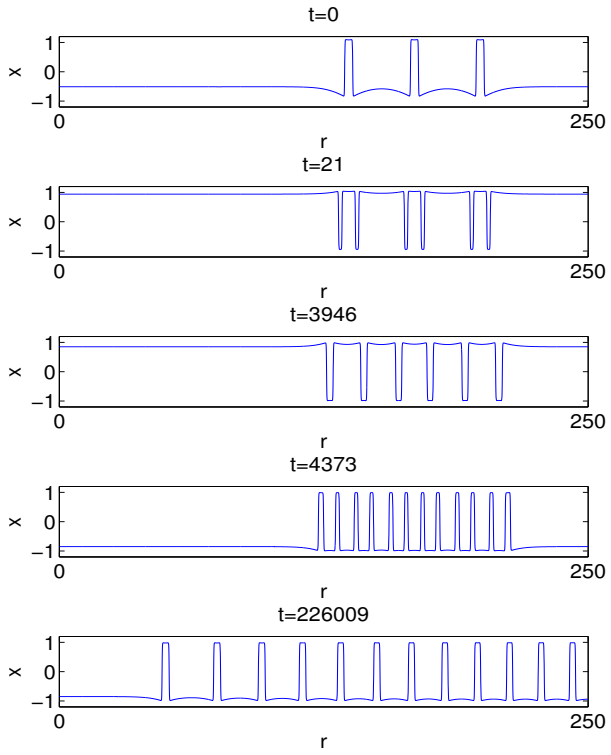


Figure 6.6: Depending on the parameter values the number of humps can also be multiplied ($d = 0.5$). Other parameters as throughout the chapter. In this case the time between two consecutive switchings must be large enough to restore the stable distance between two neighboring humps. Switchings occur only between line one and two and between line three and four.

Here we defined: $x_n = x_n$, $x_{n-1} = t_n$, $y_n = u_n$, and $y_{n-1} = v_n$. In [105] this method was used to obtain analytical results for the form of a hump.

Looking closely at the resulting patterns (lower right panel in fig. 6.4) we note that there exist small transition areas between large regions of almost constant amplitude. For an analytic approach we approximate the pattern as bivalued. In the following paragraphs we will show that there exists bistability of a period-one ($P_1$) solution (homogeneous solution) and a period-two ($P_2$) solution (Turing pattern) of the map 6.9.

We are looking for periodic solutions of this map. The period-one solution is quickly found: We set $s_n = s_{n+1}$, $t_n = t_{n+1}$, $u_n = u_{n+1}$, and $v_n = v_{n+1}$ and notice that the solutions of the map are equivalent to the stationary solutions of the zero-dimensional FHN model 3.1. With our parameters that means that there exists one real valued solution (the value can be found in tab. 6.11).

The procedure is more cumbersome in the period-two case: We now set $s_n = s_{n+2}$, $t_n = t_{n+2}$ and $u_n = u_{n+2}$ $v_n = v_{n+2}$. We arrive at the following equations

$$\begin{aligned} 0 &= -{s_n}^3 + \frac{s_n - {s_n}^3 - u_n}{2D_x} + \left( s_n - \frac{s_n - {s_n}^3 - u_n}{2D_x} \right)^3 - \frac{(s_n - au_n + d)\,\epsilon}{2D_y} \\ 0 &= au_n - 2s_n - 3d + \frac{s_n - {s_n}^3 - u_n}{2D_x} + a\left( u_n - \frac{\epsilon\,(s_n - au_n)}{2D_y} \right) \end{aligned} \tag{6.10}$$

The real valued solutions of which we can find numerically:

$$\begin{array}{lllll} P_1: & s_n = -0.715 & u_n = -0.349 & s_{n+1} = -0.715 & u_{n+1} = -0.349 \\ P_2: & s_n = -1.009 & u_n = \phantom{-}0.094 & s_{n+1} = \phantom{-}0.896 & u_{n+1} = \phantom{-}0.099 \\ P_2 & s_n = -0.842 & u_n = -0.218 & s_{n+1} = -0.198 & u_{n+1} = -0.216 \end{array} \tag{6.11}$$

Additional solutions exist with reversed sign as well as with exchanged values of $s_n$ and $s_{n+1}$ and exchanged values of $u_n$ and $u_{n+1}$. The first solution (upper row) is of period one. It is the same solution as in the zero-dimensional FHN as discussed above. The second and the third solution are of period two.

Next we want to test the stability of the solutions. We therefore linearize eqs. 6.9 around the fixed points. The corresponding eigenvalue (There are two eigenvalues for each fixed point. For a stability analysis we need to study only the eigenvalue with larger real part.) is given by:

$$\begin{aligned} \lambda &= \frac{1 - 3x_0^2 - \epsilon a + 2(D_x + D_y)(\cos(k) - 1)}{2} \\ &+ \sqrt{\frac{1 - 3x_0^2 - \epsilon a + 2(D_x + D_y)(\cos(k) - 1)}{4} - \epsilon} \end{aligned} \tag{6.12}$$

The real part of the eigenvalue is plotted versus the wavenumber $k$ in fig. 6.7. We see that the period-one solution is stable as well as the period-two solution with alternating sign. The other period-two solution is unstable. Interpreting a finite series of humps as a segment of the stable period-two solution and assuming that this segment is also stable we can understand the pattern formation in terms of the map orbits: Due to the combined action of the additive noise and the switching a finite part of the extended system is brought close to the basin of attraction of such a stable segment and is then attracted by it. With each further switching the elements at the border of the finite inhomogeneous segment are drawn towards the inhomogeneous solution.

The proper switching rate at which local inhomogeneities are created can be estimated as follows: Consider an individual system ($D_x = D_y = 0$) that initially sits at the stable fixed point $\mathbf{x}_{0,d}$ and that a switching occurs at time $t = 0$. Without further switching and in the limit of perfect timescale separation ($\epsilon \to 0$) it climbs

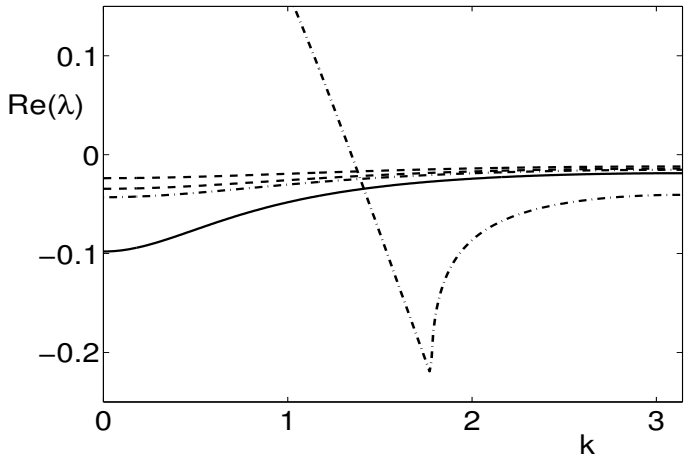


Figure 6.7: Real part of the eigenvalue of the linearized problem versus wave vector of the perturbation $k$. The plot is symmetric to $k = \pi$ and two $\pi$ periodic. For better visibility we show only a limited part of the abscissa. The solid line represents the period one solution with $s_n = -0.71526, \ldots$. We see that it is stable. The dashed lines represent the period-two solution with alternating sign ($s_n = -1.00925, \ldots$), one line for each fixed point. The dash-dotted lines represent the period-two solution with non-alternating sign ($-0.84286, \ldots$). Parameters: $a = 1.475$, $\epsilon = 0.05$, $d = 0.2$, $D_x = 0.02$, $D_y = 5.0$.

up the cubic nullcline to its maximum $x_{max}$ (From there it jumps infinitely fast to the left outer branch of the cubic nullcline.). The time T it takes for this motion is given by

$$T = \int_{\mathbf{x}_{0,-d}}^{x_{max}} dx \, \frac{1 - 3x^2}{\epsilon \left( (1-a)x + ax^3 - d \right)} \tag{6.13}$$

For our parameters we compute: $T = 0.1107/\epsilon$. If the inverse switching time $1/\gamma$ becomes comparable to $T$, the probability is high that the cloud of systems is close to the excitation threshold when a switching occurs. In this case the cloud can break up into those units that are already beyond the excitation threshold and those that lag behind as indicated in fig. 6.3.

We emphasize that the probability per unit time for the generation of humps approaches zero as the magnitude of the inhomogeneity (size of the cloud) which is determined by the intensity of the small additive Gaussian white noise vanishes. The presence of these inhomogeneities that are ubiquitous in real world systems is vital for the mechanism for pattern formation that we have described.

Apparently there exist two distinct steady states namely the homogeneous solution and the periodic (Turing) solution. We surmise that the dichotomous

switching constitutes a hard excitation causing the transition between the two states. In order to assure the existence of such a hard excitation we perform a perturbative analysis to derive the amplitude equations describing the evolution near a critical bifurcation point $d_c$ ( We consider the amplitude $d$ of $I(t)$ as control parameter.). Note, that we derive the amplitude equations solely for the purpose of showing that there exists a hard excitation in our model. We do not aim for further results that would require deeper investigations. The calculations necessary for proving the existence of a subcritical bifurcation are rather lengthy and we postpone them to the appendix B. Close to the bifurcation point the critical amplitudes $W_m$ satisfy the complex Ginzburg–Landau equation

$$F \frac{dW_m}{dt} = \alpha \, (W_{m+1} - 2W_m + W_{m-1}) + \beta \, W_m + \delta \, |W_m|^2 \, W_m \tag{6.14}$$

with parameters $F$, $\alpha$, $\beta$, and $\delta$ given by eqs. B.26.

The parameter $\delta$ determines the type of the bifurcation. For our standard parameter set the coefficient $\delta$ is positive and hence, the Turing-instability is subcritical confirming the presence of a hard excitation. Furthermore, we scanned the parameter space of the diffusion constants and found that $\delta$ is indeed always positive regardless of the values of $D_x$ and $D_y$, thus excluding a supercritical bifurcation. We remark that in order to gain information on the resulting patterns we would have to extend the analysis to higher orders of the Ginzburg–Landau equation. However, this is beyond the aim of this study.

Summarizing the results obtained so far we have learned that the dichotomous switching has two effects on the extended system. Firstly it induces a stable inhomogeneity in the form of isolated local activated regions, where isolated humps are built on the homogeneous background. Secondly it causes a transition between two coexisting stable states creating new humps with each switching. Our numerical simulations showed the stability of each of these multi-hump states. For our standard parameters the eventually resulting perfectly periodic inhomogeneous steady state (Turing pattern) turns out to be the most stable of all stationary states with respect to global switching. From an alternative point of view the global dichotomous switching entails the inhomogeneous steady state to grow at the cost of the homogeneous state. For different parameters this can be reversed.

We have demonstrated that global alteration between two different excitable dynamics yields pattern formation while each of them separately does not. The situation can hence be viewed as some kind of Parrondo's Game: switching between two loosing strategies constitutes a winning strategy [46].

### 6.3.3 High Switching Rates

We now discuss the limit of high switching rates $\gamma$, i.e. of fast fluctuations. Following Buceta et al. [19] we expect systems subject to such fluctuations to behave as if instead of the signal its average were applied. This means in our case that we have to set $I(t) \to \langle I(t) \rangle = 0$ in eq. (6.6). This changes the topology of the individual system's phase space. Now there exist three fixed points, two of which are stable and one unstable. This is illustrated in the left panel of fig. 6.8. The unstable

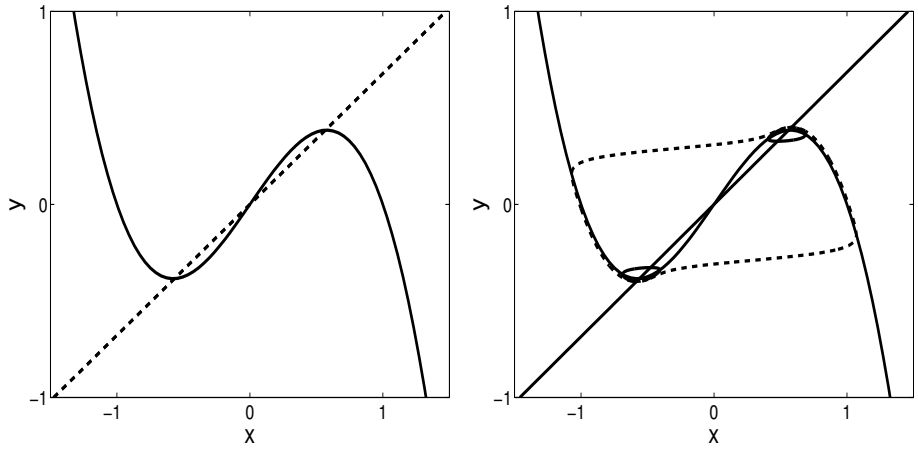


Figure 6.8: Left panel ($a = 1.475$): Three fixed points but no limit cycles exist. The fixed points are given by the intersections of the nullclines (solid lines). The outer points are stable, the inner is unstable. Right panel ($a = 1.46$): A slight change in the parameter leads to the development of three limit cycles. Around each stable fixed point there is an unstable one (solid). Around all fixed points and other limit cycles there is a stable one (dashed). In the different regimes we a find different stability of flat surfaces (see figs. 6.12 and 6.13).

fixed point is located at the origin of phase space. The two stable fixed points, denoted by $\pm\mathbf{x}_{0,det} = (\pm\tilde{x} \quad \pm\tilde{y})^t$, are symmetrically placed around it. Clearly, the extended system also possesses fixed points at these locations. Their stability however is influenced by the diffusion constants (cf. sec. 6.1).

For an analytical approach we first compute the fixed point of the individual

system ($D_x = D_y = 0$) for $I(t) = -d$ ($d$ positive). It is determined by:

$$\begin{aligned}\tilde{x} &= \frac{2^{\frac{1}{3}}\ (a-1)}{\left(27\,a^2\,d + \sqrt{108\,(1-a)^3\,a^3 + 729\,a^4\,d^2}\right)^{\frac{1}{3}}} \\ &+ \frac{\left(27\,a^2\,d + \sqrt{108\,(1-a)^3\,a^3 + 729\,a^4\,d^2}\right)^{\frac{1}{3}}}{3\,2^{\frac{1}{3}}\,a} \\ \tilde{y} &= \frac{x_0 - d}{a}\,, \end{aligned} \tag{6.15}$$

For a more convenient treatment we rewrite eqs. 6.6 in terms of coordinates relative to the fixed point ($x \to x + \tilde{x}$):

$$\begin{aligned}\dot{x} &= Ax + Bx^2 + Cx^3 - y + D_x\Delta x \\ \dot{y} &= \epsilon(x - ay) + D_y\Delta y \end{aligned} \tag{6.16}$$

with $A = 1 - \tilde{x}^2$, $B = -3\tilde{x}$, and $C = -1$.

With these conventions the eigenvalue $\rho$ with the larger real part is given by:

$$\begin{aligned}\rho &= \frac{1}{2}\left(A + \tilde{D}_x + \tilde{D}_y - a\epsilon\right) \\ &+ \frac{1}{2}\sqrt{\left(A + \tilde{D}_x + \tilde{D}_y - a\epsilon\right)^2 - 4(A + \tilde{D}_x)(\tilde{D}_y - a\epsilon) - 4\epsilon} \end{aligned} \tag{6.17}$$

with

$$\tilde{D}_{x,y} = 2(\cos(k) - 1)D_{x,y} \tag{6.18}$$

The critical wavenumber $k_c$, that is the one for which the maximum value of the real part of $\rho$ crosses zero is given by

$$k_c = \arccos\left(1 - \frac{1}{4}\left[\frac{A}{D_x} - \frac{a\epsilon}{D_y}\right]\right) \tag{6.19}$$

In fig. 6.9 we show regions of Turing instability in the $k$–$D_y$–plane. For properly chosen diffusion constants perturbations of finite nonzero wavelength are favored to grow. In the same figure we also show the region of Turing instability in the $D_x$–$D_y$–plane for different values of the timescale separation $\epsilon$. For enhanced $\epsilon$ the region is enlarged.

We verify the instability numerically by initializing a homogeneous system at the fixed point of the deterministic system $\pm\mathbf{x}_{0,det}$ and apply global dichotomous switching with rate $\gamma = 2000$. As expected we find the behavior as known from

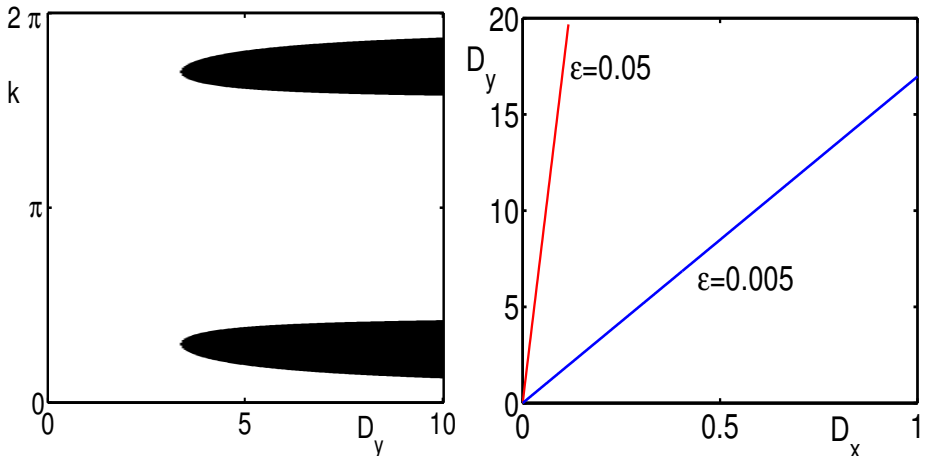


Figure 6.9: Left: Regions of positive real part (black) of the eigenvalue of the linearized problem in the inhibitor coupling strength–wave vector plane. Other parameters the same as throughout the paper. Right: Region of Turing instability for different values of the timescale separation $\epsilon$. The homogeneous state is unstable above the lines.

the Turing instability. Small fluctuations grow all over the medium and a regular periodic pattern evolves. The typical wavelength of this periodic pattern coincides with that of the deterministic system. To verify that pattern formation is indeed due to the Turing mechanism we reduced the inhibitor diffusion constant $D_y$ from our standard value $D_y = 5.0$ to $D_y = 0.5$. In this case the homogeneous pattern persists. Hence, destabilization of the homogeneous state is due to the influence of diffusion.

We visualize the effect of different switching rate $\gamma$ in fig. 6.10. For low and intermediate rates we have started with inhomogeneous, for high rates with homogeneous initial conditions. Remember that inhomogeneities grow due to the combined action of global switching and small additive noise as demonstrated in fig. 6.3. In all situations we applied Gaussian white noise of intensity $10^{-6}$ to each individual element. The growth of the patterns is due to three different mechanisms: For $\gamma = 0$ (upper row) the instable border grows slowly into the homogeneous region. In the case of intermediate $\gamma$ switchings generate additional layers at the boundary. If we denote with $L$ the period length of the final pattern in fig. 6.4 we can estimate the average speed of the growth of the pattern's radius as follows: After the time $T$ the process $I(t)$ has on average switched $\gamma T$ times. With each switching an additional layer (half a hump) is appended to the inhomogeneity. The average speed of the propagation of the boundary $\hat{v}$ is then given by $\hat{v} = \frac{1}{2}\gamma L$. This constitutes an upper limit for the average speed because switchings have

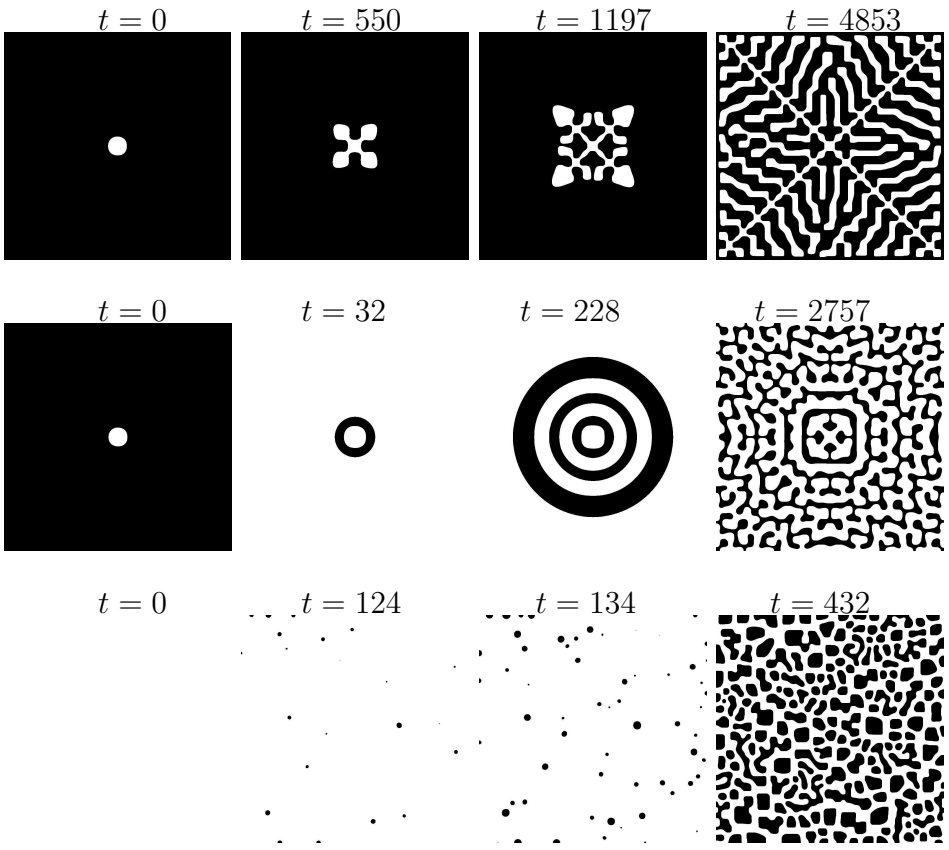


Figure 6.10: Timeseries with different switching rates. The time is given above each plot. Parameters: $\gamma = 0$ (upper row), 5.0 (middle row), 0.01 (lower row); $\epsilon = 0.05$, $a = 1.475$, $D_x = 0.02$, $D_y = 5.0$, $d = 0.2$.

no effect on the growth of the pattern if they occur too early, i.e. before the homogeneous part is in the vicinity of a fixed point. Simulations with different parameter values showed that it is also possible to add instead of one half a layer three, five, or more halves at each side of the inhomogeneity. Also, it is possible to decrease the size of the inhomogeneity. The average speed of propagation is therefore more generally given by:

$$\bar{v} = \left(\frac{1}{2} + Z\right)\gamma L \tag{6.20}$$

where $Z$ is an integer number that depends on the parameters of the system ($L$ also depends on the parameters.).

For high $\gamma$ inhomogeneities grow all over the array. The speed with which the patterns grow is therefore different for the three cases: the faster the switching the

faster the growth.

## 6.4 Frozen Noise

In this section we investigate the limit of vanishing switching rates of the random telegraph signal. Instead, we apply static dichotomous disorder. The spatial correlation of the disorder is governed by the lattice spacing used in our simulations. An example of a realization of such dichotomous disorder in a 2–d system is depicted in the left panel of fig. 6.11. The right panel shows the results of

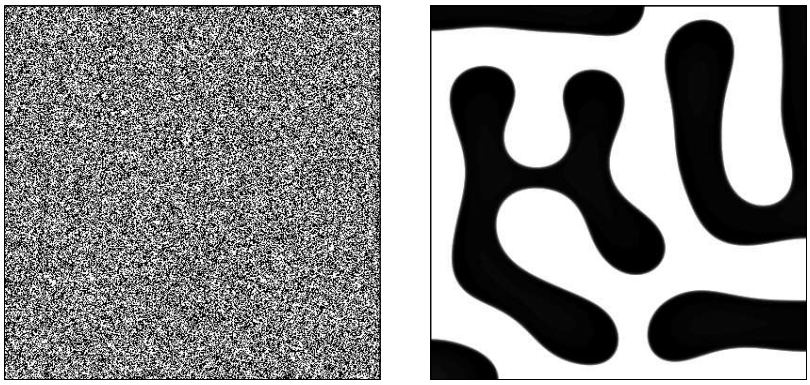

Figure 6.11: Turing pattern (right) obtained by applying frozen dichotomic disorder (left) to a homogeneous system at the fixed point. $K(i,j) = \delta_{i,j}$; Size: $400 \times 400$; $\Delta r = 0.1$; $d = 0.2$;

a numerical simulation with that noise realization. As in the case of fast global switching we see a Turing pattern emerge. The pattern is not a mere reflection of the underlying disorder but has a structure of it's own. It's typical wavelength is much larger than that of the disorder. As initial conditions we chose $x_i = 0.56748$ and $y_i = 0.384732$ for all $i = 1, ..., N$. This is the location of the stable fixed point of a single system without dichotomous driving ($I_i = 0$). The dynamical process of pattern formation is again driven by a Turing instability. Perturbations of a certain critical wavelength grow until they form the pattern shown in Fig 6.11. The pattern formation takes place in 2-d as well as in 1-d. Typically, Turing patterns in 2-d come in two different shapes ( [60]): In labyrinth- and in hexagonal shape. In our study we found that for our parameters eqs. 6.6 support only the labyrinth type.

Now we address the influence of different correlation length on the pattern formation. We have investigated numerically different samples with the same lattice constant but with frozen dichotomous signals of different typical wavelength.

The implementation in our numerical computations proceeds as follows: For every run of our simulation we choose a different integer $l$. We randomly select a value for the realization of $I$ for the first element of the lattice system and apply this value to $l-1$ consecutive elements. We then pick a new $I-$value independently of the first, apply it to the next $l$ units, and so on. When the boundary of the grid is reached we apply the same realization of $I$ to the $l-1$ consecutive lines. This procedure is repeated until the whole space is filled with squares of side length $l$ that share a realization of $I$.

Until now we have dealt with the situation where the typical wavelength $l\Delta r$ of the disorder is much smaller than that of the pattern. Now we explore the opposite case: The typical wavelength is much larger than that of the pattern we have observed above. An example is given in fig. 6.12.

Figure 6.12: Instability of the boundary. We show successive snapshots of a $2000 \times 2000$ array with $\Delta r = 0.02$ at $t = 0$, $t = 170$, and $t = 705$. The pattern slowly evolves throughout the whole space. $a = 1.475$.

As initial conditions we used $\mathbf{x}_{0,det}$. With coarse disorder (compared to the lattice spacing as well as to the pattern wave length) there arise sharp borders separating the extended regions associated with the two different values of the static disorder. Units far from these borders feel little of the disorder and hence get, as in a deterministic system, attracted by the fixed point connected with the local realization of $I$. The interface between the two regions at a corner is not stable, though. As the central and right panels in fig. 6.12 reveal, fluctuations in the border region grow and expand into the homogeneous part of the pattern. This behavior goes on until the complete plane displays a patterned structure. As stated above this effect is not observable in the 1-d system.

It is illustrative to examine cases with slightly different values of the parameter $a$. While for our standard parameter $a = 1.475$ a flat border is stable and we need a certain curvature for inhomogeneities to grow a slight change to $a = 1.46$ destabilizes flat surfaces. This is shown in fig. 6.13. As is demonstrated in fig. 6.8

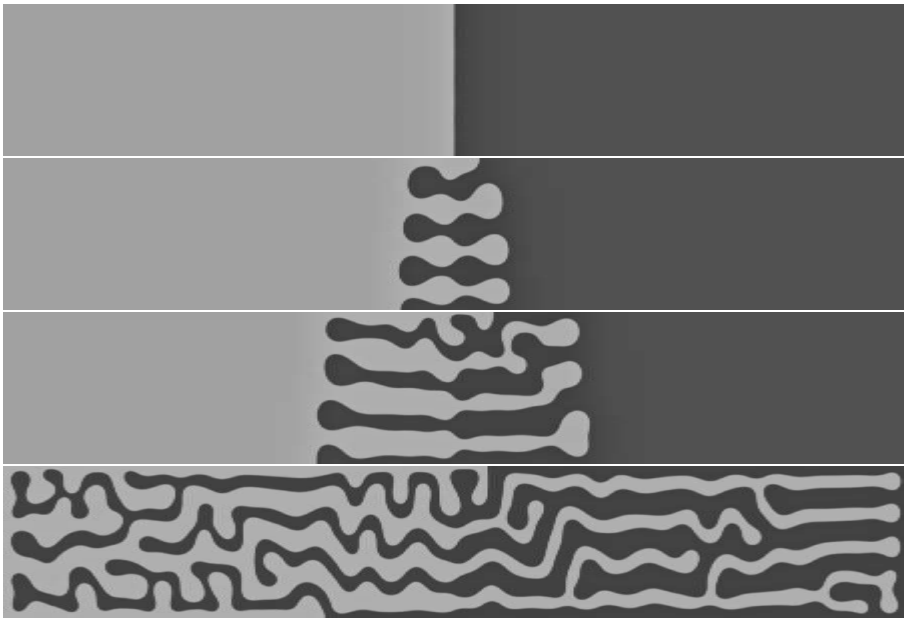

Figure 6.13: Instability of a straight boundary. We show successive snapshots of a $500 \times 3000$ array with $\Delta r = 0.2$ at $t = 250$, $t = 1357$, $t = 2370$, and $t = 4163$. The pattern slowly evolves throughout the whole space. $a = 1.46$, $D_x = 0.1$, $D_y = 10$.

this change of parameters goes along with a qualitative change of the topology of the system's phase space: Three limit cycles are born. Two of them are unstable and are centered around the stable fixed points. One is stable and envelops all fixed points and other limit cycles.

Particularly illuminating are simulations using different correlation lengths in parameter regions where the homogeneous deterministic system ($I_i(t) = 0$) does not support Turing pattern formation. We therefore reduce the inhibitor coupling coefficient to $D_y = 0.5$. In the deterministic system the homogeneous solution at the fixed points $x_{0,det}$ is stable ($-x_{0,det}$ as well). If we apply a very fine dichotomic noise realization, i.e. one with a small typical length $l\Delta r$ we find, as expected, a behavior equivalent to that of the deterministic system: a homogeneous distribution at the fixed point (upper row in fig. 6.14). If we apply a coarser dichotomic perturbation we observe a behavior differing from that of the deterministic system: Stationary patterns form (lower line in fig. 6.14). We can thus increase the parameter range in which Turing patterns emerge. We want to emphasize that the ratio between activator and inhibitor diffusion constant can be significantly decreased.

To gain some insight into the role of large correlation length of the disorder we

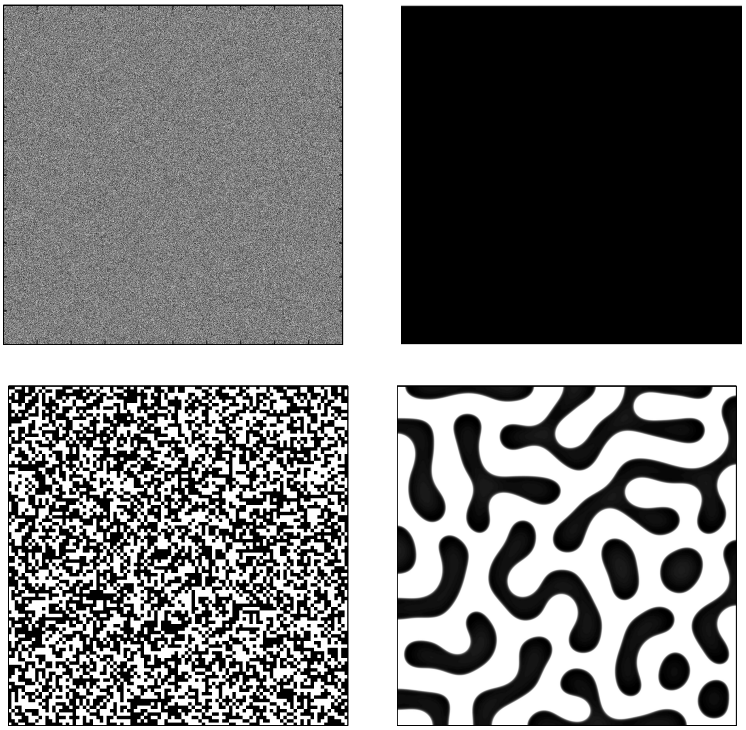

Figure 6.14: Coarse fluctuations support pattern formation, fine ones do not. In this parameter regime the system with $I_i(t) = 0$ does not support Turing pattern formation. $D_y = 0.5$, $\Delta r = 0.02$, $l = 1$ (upper row) and $l = 20$ (lower row). $2000 \times 2000$ points are shown.

computed its structure factor $S(k)$ in 1-d. It is given by the Fourier transform of the spatial correlation function. The latter is computed as follows:

$$\langle I_i\, I_j \rangle = \sum_{I_i, I_j = +d, -d} I_i I_j\, p(I_i, I_j) \tag{6.21}$$

where $p(I_i, I_j)$ is the joint probability that $I$ takes the value $\pm d$ at site $i$ and $\pm d$ at site $j$. There are four different combinations for that but due to symmetry reasons it reduces to only two different values for $p$, one for equal realizations, and one for realizations with opposite signs.

These probabilities can be expressed in terms of conditional probabilities:

$$\begin{aligned} p(I_i = +d, I_j = +d) &= p(i, j \in l_k) p(I_i = +d, I_j = +d; i, j \in l_k) \\ &+ p(i, j \notin l_k) p(I_i = +d, I_j = +d; i, j \notin l_k) \end{aligned} \tag{6.22}$$

Here $p(i, j \in l_k)$ is the probability that site $i$ and site $j$ are in the same interval (with index $k$; $k = 1 \ldots N/l$) of length $l$ in which we fixed the value of $I$. $p(I_i =$

$+d, I_j = +d; i, j \in l_k$) denotes the conditional probability that $I_i$ takes the value $+d$ and $I_j$ takes the value $+d$ if the corresponding sites are in the same aforementioned interval. With our algorithm for constructing the frozen disorder of box length $l$ the latter probability is equal to one half (one half for either sign of $I$). $p(I_i = +d, I_j = +d; i, j \notin l_k)$ is equal to one forth (one forth for each combination of $I_i$ and $I_j$). $p(i, j \in l_k)$ can be calculated as follows: The probability that randomly chosen elements that are further apart than the length of an interval belong to the same interval is zero. If they are closer than that, the probability that the border between two intervals lies between the two elements, is given by

$$p(i, j \notin l_k) = \frac{|i-j|}{l} \qquad |i-j| < l. \tag{6.23}$$

The elements with sites $i$ and $j$ are then not in the same interval. $p(i, j \in l_k) = 1 - p(i, j \notin l_k)$ is the complementary probability.

With this we are able to compute:

$$\langle I_i \, I_j \rangle = d^2 \left( 1 - \frac{|i-j|}{l} \right) \tag{6.24}$$

and we finally arrive at:

$$S(k) = \frac{2d^2}{lk^2} \left( 1 - \cos(kl) \right). \tag{6.25}$$

We show a plot of the 2-d autocorrelation function in fig. 6.16 and the averaged 1-d power spectrum in fig. 6.15 (simulation results).

Note that the power at the critical wavenumber $k_c$ is much higher in the case of large correlation length of the disorder than for small correlation length. This is a possible reason for the formation of the patterns. The high power at $k_c$ may lead to a larger amplitude of the deviations from the steady state of wavelength $k_c$ and drive the system further into the nonlinear regime.

## 6.5 Summary

We have investigated the influence of dichotomous fluctuations on pattern formation in a diffusively coupled extended FHN system. Locally, one of two excitable dynamics is realized at a certain time. In both cases there exists one stable homogeneous steady state. With appropriate switching between the two dynamical regimes either of the two steady states can be destabilized. For very fast global switching (compared to the activation time of the FHN) as well as for frozen disorder with small correlation length (compared to the correlation length of the

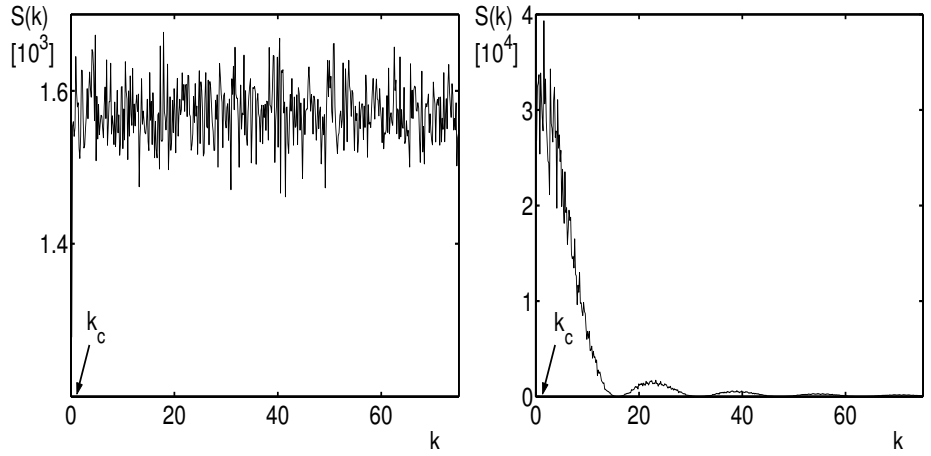


Figure 6.15: Structure factor $S(k)$ of the underlying noise for the patterns in fig. 6.14. The left panel corresponds to the fine disorder in fig. 6.14 (upper row), the right to the coarse disorder (lower row).

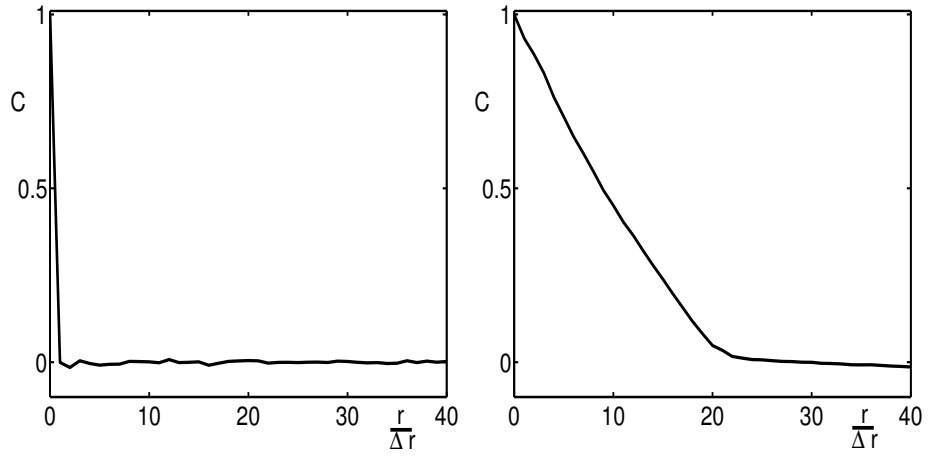


Figure 6.16: Autocorrelation of the noise $C = \langle I_i I_j \rangle$ (where the sites $i$ and $j$ are $r$ apart) over the distance $r$. The left panel corresponds to the upper noise realization in fig. 6.14, the right panel to the lower one.

resulting pattern) the parameter regime at which the destabilization takes place coincides with those values for which Turing instability occurs in the system with applied mean value of the fluctuations ($I = \langle I \rangle = 0$).

In the case of global alterations of intermediate switching rate $\gamma$ (comparable to the inverse activation time) we found a new mechanism to create spatial structures.

If one switching event occurs at the correct time stable local inhomogeneities are formed. Further switchings lead to a growth of the inhomogeneous regions at the boundary to the homogeneous regions. The pattern is in that sense more stable with respect to slow global alterations of the dynamics than the homogeneous state. Investigation of the stationary solutions of the system with the help of a nonlinear map approach yields bistability of a period-one and a period-two orbit corresponding in real space to the homogeneous and the Turing pattern state, respectively. After a stable spatial inhomogeneity is formed both of these states coexist in the extended system. The regions are coupled via diffusion terms. The effect of further switching is then to enlarge the region of inhomogeneity on the expense of the homogeneous region. We remark that a change of the parameters reverses the process back to the overall homogeneous state.

Applying frozen dichotomous disorder of finite nonzero correlation length causes destabilization of the homogeneous steady states leading again to Turing patterns. This holds even for parameter values for which the dynamics obtained by spatiotemporal averaging of $I$ as performed in [22] does not sustain Turing instability. In particular in our case no strong deviation between the diffusion constants of the activator and inhibitor is needed.

We also performed investigations with fluctuations varying in both space and time.

If the spatial disorder initiates pattern creation and the inverse switching frequency is higher than the evolution time a pattern will typically be created before the next switching occurs. The next realization of the disorder will have hardly any impact on the once established pattern. Since the labyrinth pattern is stable against any realization of the disorder (at least for our noise strength) such a pattern persists once established. There will therefore be no systematic influence of the temporal fluctuations.

On the other hand if we look at large spatial correlation lengths and fast switching times we note that the time it takes for the pattern to evolve from the boundaries of a pattern with very coarse spatial disorder (cf. fig. 6.12) into the homogeneous regions is also much larger than the typical evolution time of a labyrinth pattern caused by fast switching. The former phenomenon will therefore have only little effect on the resulting pattern.

In the case of very fast switching and very small typical wavelength of the disorder the dynamics of the system average out the fluctuations just as it is the case with high spatial or temporal switching rates, only.

It is only in the case of intermediate spatial and temporal switching rates that both effects have an influence on the system. We find that the spatial and temporal disorder usually provides the right conditions for inhomogeneities to grow at an earlier time and at more sites in the system and thereby speeds up the pattern

formation.

Adding a spatial or temporal component to the fluctuations assists the system to average them out. Therefore the effect of enhancing Turing pattern formation by a certain typical nonzero wavelength (cf. fig. 6.14) is disabled by high switching rates.

# Chapter 7

# Conclusions

We have contributed to the growing field of constructive effects of fluctuations. The subject of our investigations was the interaction of noise and excitable media. We have studied prototypical models instead of focusing closely onto explicit real world systems. General principles were favored over quick applicability.

Investigations of stochastic nonlinear dynamical systems is a challenging task. Not only are analytical results hard to obtain but also are numerical studies subject to restrictions such as finiteness and limited stability. Langevin equations as well as the Fokker–Planck equation are among the prominent scientific tools that are used in this field. While the time-dependent Fokker–Planck equation for nonlinear systems is solvable for special cases, only, its stationary solution can usually be obtained more easily. This holds for analytical as well as for numerical solutions. This stationary solution shows reminiscences of the of the dynamics of the described system (cf. chap. 3). For our prototypical excitable model we found that coherence resonance is expressed by qualitative changes in the corresponding stationary probability distribution.

In case the Fokker–Planck equation is not effective, other methods have to be applied. The method of the moment dynamics received comparatively little attention. It is applicable in many cases where techniques that base on the Fokker–Planck equation fail (cf. chap. 4). For an effective use approximations have to be applied to the resulting set of equations. These approximations can be categorized into two different classes, one consisting of neglecting cumulants and one of neglecting moments above a certain order. They perform differently well under the influence of varying noise strength and strength of nonlinearities. Overall the approximations based on neglecting cumulants above certain order performed better in our study. Especially interesting is the surprisingly good qualitative agreement of the Gaussian approximation with results from Langevin simulations (cf. chap. 5). A comprehensive study of this feature would be valuable.

As a basic step towards the investigation of the interplay between noise and

excitability we have demonstrated that it is noise in the first place that induces excitability into systems that otherwise exhibit non-excitable, monostable dynamics, only (cf. chap. 4). It is not only excitability that can be created but also much more complicated dynamics. We have found oscillatory dynamics, chaos, a Canard explosion of the chaotic attractor, and many other dynamical regimes.

We have demonstrated the influence of noise on already existing excitable dynamics by investigating a globally coupled ensemble of FitzHugh–Nagumo systems. Here, too, noise greatly enriches the dynamics of the ensemble. A complicated transition from a stable fixed point through a variety of different dynamical states to a oscillation or spiking regime. This transition to oscillations with all its complicated sequence of dynamical regimes marks a special class of systems. The globally coupled FitzHugh–Nagumo system as well as the model for pure noise-induced phase transitions that we studied in chap. 4) belong to its representatives. Notably, the two models exhibit clear dynamical differences, e.g. they posses different nonlinearities. The necessary ingredients for this complex transition would be an interesting subject of further studies.

The introduction of spatial dimensions demonstrates further examples of the ordering effect of fluctuations. The possibility of spatial pattern formation emerges. We have presented an example that proves beneficial influence of fluctuations on spatial ordering. Dichotomous switching between two dynamics that by themselves do not support pattern formation can lead to patterns known from the Turing instability. The role of different spatial and temporal correlations in such systems is manifold. For one thing they determine the type of resulting pattern. For another they select the mechanism which leads to patterns formation.

The influence of fluctuations on excitable media is multifaceted. A great variety of different nontrivial effects with contributions from various fields of science exist. This study can therefore by no means be called comprehensive. Still, we hope to have given some impulses to other scientists be it theoreticians or experimentalists to find and explain new such phenomena and applications thereof.

# Bibliography


[1] Aliev, R. R. ; Panfilov, A. V.: A simple two-variable model of cardiac Excitation. In: *Chaos, Solitons and Fractals* 7 (1995), Nr. 3, S. 293–301

[2] Argentina, M. ; Coullet, P. ; Krinsky, V.: Head-on collisions of waves in an excitable FitzHugh-Nagumo system: a transition from wave annihilation to classical wave behavior. In: *Journal of theoretical Biology* 205 (2000)

[3] Bak, P. ; Chen, K. ; Tang, C.: A forest-fire model and some thoughts on turbulence. In: *Physics Letters A* 147 (1990)

[4] Bär, M. ; Eiswirth, M. ; Rotermund, H. H. ; Ertl, G.: Solitary Wave Phenomena in an Excitable Surface Reaction. In: *Physical Review Letters* 69 (1992), S. 945–948

[5] Barkley, D.: Euclidean symmetry and the dynamics of rotating spiral waves. In: *Physical Review Letters* 72 (1994)

[6] Beato, V.: 2005. – PhD thesis at Technische Universität Berlin

[7] Beato, V. ; Sendiña-Nadal, I. ; Gerdes, I. ; Engel, H.: Noise-induced wave nucleations in an excitable chemical reaction. In: *Physical Review E* 71 (2005), S. 035204(R)

[8] Benzi, R. ; Parisi, G. ; Sutera, A. ; Vulpiani, A.: The mechanism of Stochastic Resonance. In: *Tellus* 34 (1982), S. 10

[9] Blasdel, G. G. ; Salama, G.: Voltage-sensitive dyes reveal a modular organization in monkey striate cortex. In: *Nature* 321 (1986), S. 579

[10] Bonilla, L. L. ; Casado, J. M. ; Morillo, M.: Self-synchronization of populations of nonlinear oscillators in the thermodynamic limit. In: *Journal of Statistical Physics* 48 (1987), Nr. 3/4, S. 571

[11] Bonilla, L. L. ; Casado, J. M. ; Morillo, M.: Corrigendum to self-synchronization of populations of nonlinear oscillators in the thermodynamic limit. In: *Journal of Statistical Physics* 50 (1988)

[12] Bordiougov, G. ; Engel, H.: Oscillatory dispersion and coexisting stable pulse trains in an excitable medium. In: *Physical Review Letters* 90 (2003)

[13] Braune, M. ; Engel, H.: Compound rotation of spiral waves in active media with periodically modulated excitability. In: *Chemical Physics Letters* 211 (1993), S. 534

[14] Braune, M. ; Engel, H.: Kinematical description of meandering spiral waves in active media. In: *Zeitschrift für Physikalische Chemie* 216 (2002), S. 675

[15] Bressloff, P. C. ; Coombes, S.: Physics of the extended neuron. In: *International Journal of Modern Physics B* 11 (1997)

[16] Broeck, C. V. ; Parrondo, J. M. R. ; Toral, R.: Noise-Induced Nonequilibrium Phase Transition. In: *Physical Review Letters* 73 (1994), S. 3395

[17] Broeck, C. V. ; Parrondo, J. M. R. ; Toral, R. ; Kawai, R.: Nonequilibrium phase transitions induced by multiplicative noise. In: *Physical Review E* 55 (1997), S. 4084

[18] Broeck, C. V. ; Parrondo, J. M. R. ; Toral, R. ; Kawai, R.: Nonequilibrium phase transitions induced by multiplicative noise. In: *Physical Review E* 55 (1997), S. 4084

[19] Buceta, J. ; Ibañez, M. ; Sancho, J. M. ; Lindenberg, K.: Noise-driven mechanism for pattern formation. In: *Physical Review E* 67 (2003), S. 021113

[20] Buceta, J. ; Lindenberg, K. ; ; Parrondo, J. M. R.: Stationary and Oscillatory Spatial Patterns Induced by Global Periodic Switching. In: *Physical Review Letters* 88 (2002), S. 024103

[21] Buceta, J. ; Lindenberg, K.: Switching-induced Turing instability. In: *Physical Review E* 66 (2002), S. 046202

[22] Buceta, J. ; Lindenberg, K.: Spatial patterns induced purely by dichotomous disorder. In: *Physical Review E* 68 (2003), S. 011103

[23] Buceta, J. ; Lindenberg, K. ; Parrondo, J. M. R.: Pattern formation induced by nonequilibrium global alternation of dynamics. In: *Physical Review E* 66 (2002), S. 036216

[24] Buxhoeveden, D. P. ; Switala, A. E. ; Roy, E. ; F.Casanova, M.: Quantitative analysis of cell columns in the cerebral cortex. In: *Journal of Neuroscience Methods* 97 (2000), S. 7

[25] Collins, J. J. ; Chow, C. C. ; Imhoff, T. T.: Aperiodic stochastic resonance in excitable systems. In: *Physical Review E Rapid Communications* 52 (1995), Nr. 4, S. R3321

[26] Collins, J. J. ; T. T. Imhoff, P. G.: Noise-enhanced tactile sensation. In: *Nature* 383 (1996)

[27] Dawson, D. A.: Critical dynamics and fluctuations for a mean-field model of cooperative behavior. In: *Journal of Statistical Physics* 31 (1983), Nr. 1, S. 29

[28] Desai, R. C. ; Zwanzig, R.: Statistical mechanics of a nonlinear stochastic model. In: *Journal of Statistical Physics* 19 (1978), Nr. 1, S. 1

[29] DeVille, R. E. ; Vanden-Eijnden, E. ; Muratov, C. B. ; E, W.: Two distinct mechanisms of coherence in randomly perturbed dynamical systems. In: *submitted to Physical Review E* (2005)

[30] (eds.), P. L. N.: *Neocortical Dynamics and Human EEG Rhythms*. Oxford University Press, 1995

[31] Einstein, A.: Über die von der molekularkinetischen Theorie der Wärme geforterte Bewegung von in ruhenden Flüssigkeiten suspendierten Teilchen. In: *Annalen der Physik* 4 (1905), S. 549

[32] Elphick, C. ; Hagberg, A. ; Meron, E.: Dynamic front transitions and spiral-vortex nucleation. In: *Physical review E* 51 (1995), Nr. 4, S. 3052

[33] Farkas, I. ; Helbing, D. ; Vicsek, T.: Mexican waves in an excitable medium. In: *Nature* 419 (2002), S. 131

[34] FitzHugh, R.: Impulses and physiological states in theoretical models of nerve membrane. In: *Biophysical Journal* 1 (1961)

[35] Freeman, W.: Tutorial on neurobiology: From single neurons to brain chaos. In: *International Journal of Bifurcation and Chaos* 2 (1992)

[36] Freund, J. A. ; Schimansky-Geier, L. ; Beisner, B. ; Neiman, A. ; Russell, D. ; Yakusheva, T. ; Moss, F.: Behavioral Stochastic Resonance: How the Noise from a Daphnia Swarm Enhances Individual Prey Capture by Juvenile Paddlefish. In: *Journal of Theoretical Biology* 214 (2002)

[37] Gang, H. ; Ditzinger, T. ; Ning, C. Z. ; Haken, H.: Stochastic resonance without external periodic force. In: *Physical Review Letters* 71 (1993), Nr. 6, S. 807

[38] García-Ojalvo, J. ; Sancho, J. M.: *Noise in Spatially Extended Systems*. Springer, 1999

[39] Gardiner, C. W.: *Handbook of Stochastic Methods*. Springer Verlag, 1994

[40] Gerstner, W. ; Kistler, W.: *Spiking Neuron Models*. Cambridge University Press, 2002

[41] Giudici, M. ; Green, C. ; Giacomelli, G. ; Nespolo, U. ; Tredicce, J. R.: Andronov bifurcation and excitability in semiconductor lasers with optical feedback. In: *Physical Review E* 55 (1997), S. 6414

[42] Glendinning, P.: *Stability, instability and chaos: an introduction to the theory of nonlinear differential equations*. Cambridge University Press, 1994

[43] Graham, R.: *Statistical theory of instabilities in stationary non-equilibrium systems with applications to lasers and nonlinear optics*. Springer Verlag, 1984

[44] Gutkin, B. S. ; Ermentrout, G. B. ; O'Sullivan, J.: Layer 3 patchy recurrent excitatory connections may determine the spatial organization of sustained activity in the primate prefrontal cortex. In: *Neurocomputing* 32 (2000)

[45] Hänggi, P. ; Talkner, P.: A remark on truncation schemes of cumulant hierarchies. In: *Journal of statistical physics* 22 (1980), S. 65

[46] Harmer, G. P. ; Abott, D.: Losing strategies can win by Parrondo's paradox. In: *Nature* 199 (1999), S. 402

[47] Hasegawa, H.: Dynamical mean-field theory of noisy spiking neuron ensembles: Application to the Hodgkin-Huxley model. In: *Physical Review E* 68 (2003), S. 041909

[48] Hasegawa, H.: Dynamical mean-field approximation to small-world networks of spiking neurons: From local to global and/or from regular to random couplings. In: *Physical Review E* 70 (2004), S. 066107

[49] Hennig, D. ; ; Rasmussen, K. ¦ Gabriel, H. ; Bülow, A.: Solitonlike solutions of the generalized discrete nonlinear Schrödinger equation. In: *Physical Review E* 54 (1996), S. 5788

[50] Hennig, D. ; Tsironis, G.P.: Wave Transmission in Nonlinear Lattices. In: *Physics Reports* 307 (1999), S. 333

[51] Hindmarsh, J. L. ; Rose, R. M.: A model of the nerve impulse using two first-order differential equations. In: *Nature* 296 (1982), S. 126

[52] Hodgkin, A. F. ; Huxley, A. L.: A quantitative description of membrane currents and its application to conduction and excitation in nerve. In: *Journal of Physiology* 117 (1952), S. 500

[53] Ito, T. O. A. ; Tetsuka, A.: Self-organization in an excitable reaction-diffusion system: Synchronization of oscillatory domains in one dimension. In: *Physical Review A* 42 (1990)

[54] Izos, G. G. ; Deza, R. R. ; Wio, H. S.: Exact nonequilibrium potential for the FitzHugh–Nagumo model in the excitable and bistable parameter regimes. In: *Physical Review E* 58 (1998)

[55] Kadar, S. ; Wang, J. ; Showalter, K.: Noise-supported traveling waves in sub-excitable media. In: *Nature* 391 (1998), S. 770

[56] Kampen, N. G. V.: *Stochastic Processes in Physics and Chemistry*. North Holland, 1997

[57] Kawai, R. ; Sailer, X. ; Schimansky-Geier, L.: Macroscopic limit cycle via noise-induced phase transition. In: *SPIE Proceedings* 5514 (2003), S. 173

[58] Kawai, R. ; Sailer, X. ; Schimansky-Geier, L. ; Broeck, C. V.: Macroscopic limit cycle via pure noise-induced phase transition. In: *Physical Review E* 69 (2004), S. 051104

[59] Kim, S. ; Park, S. H. ; Ryu, C. S.: Colored-noise-induced multistability in nonequilibrium phase transitions. In: *Physical Review E* 58 (1998), S. 7994

[60] Koch, A. J. ; Meinhardt, H.: Biological pattern formation: from basic mechanisms to complex structures. In: *Reviews of Modern Physics* 66 (1994), S. 1481

[61] Koch, C.: *Biophysics of Computation: Information Processing in Single Neurons*. Oxford University Press, New York, 1999

[62] Koga, S. ; Kuramoto, Y.: Localized Patterns in Reaction-Diffusion Systems. In: *Progress of Theoretical Physics* 63 (1980), S. 106

[63] Kostova, T. ; Ravindran, R. ; Schonbek, M.: FitzHugh–Nagumo revisited: Types of bifurcations, periodical forcing and stability regions by a Lyapunov functional. In: *International Journal of Bifurcation and Chaos* 14 (2004), Nr. 3, S. 913–925

[64] Kostur, M. ; Sailer, X. ; Schimansky-Geier, L.: Stationary probability distributions for FitzHugh-Nagumo systems. In: *Fluctuation and Noise Letters* 3 (2003), S. 155

[65] Kostur, M. ; Schimansky-Geier, L.: Numerical study of diffusion induced transport in 2D systems. In: *Physics Letters A* 265 (2000)

[66] Kuramoto, Y.: *Chemical oscillations, waves, and turbulence*. Springer Verlag, 1984

[67] L. Gammaitoni, P. J. ; Marchesoni, F.: Stochastic Resonance. In: *Review of Modern Physics* 70 (1998)

[68] Langevin, P.: Sur la théorie du mouvement brownien. In: *Comptes Rendu* 146 (1908), S. 530

[69] Levitt, J. B. ; Lewis, D. A. ; Yoshioka, T. ; Lund, J. S.: Topography of pyramidal neuron intrinsic connections in Macaque monkey prefrontal cortex (areas 9 and 46). In: *The Journal of Comparative Neurology* 338 (1993), S. 260

[70] Lindner, B.: 2002. – Coherence and Stochastic Resonance in Nonlinear Dynamical Systems; PhD thesis

[71] Lindner, B. ; Garcia-Ojalvo, J. ; Neiman, A. ; Schimansky-Geier, L.: Effects of noise in excitable systems. In: *Physical Report* 392 (2004)

[72] Lindner, B. ; Schimansky-Geier, L.: Coherence and stochastic resonance in a two-state system. In: *Physical Review E* 61 (2000), S. 6103

[73] Loecher, M.: *Noise sustained patterns.* World Scientific Publishing Co. Pte. Ltd., 2003

[74] Makarov, V. A. ; Nekorkin, V. I. ; Velarde, M. G.: Spiking behavior in a noise-driven system combining oscillatory and excitable properties. In: *Physical Review Letters* 86 (2001), Nr. 15, S. 3431

[75] Malakhov, A. N.: Kinetic equation for bitemporal cumulant functions of a Markovian process. In: *Radiofizika* 19 (1976), S. 214–223

[76] Malakhov, A. N.: Kinetic equations for the cumulants of an arbitrary Markovian process. In: *Radiofizika* (1976)

[77] Mangioni, S. ; Deza, R. ; Toral, R. ; Wio, H. S.: Nonequilibrium phase transitions induced by multiplicative noise: Effect of self-correlation. In: *Phys. Rev. E* 61 (2000), S. 223

[78] Mangioni, S. ; Deza, R. ; Wio, H. S. ; Toral, R.: Disordering Effects of Color in Nonequilibrium Phase Transitions Induced by Multiplicative Noise. In: *Phys. Rev. Lett.* 79 (1997), S. 2389

[79] Marino, F. ; Catalan, G. ; Sanchez, R. ; Balle, S. ; Piro, O.: Thermo-optical "Canard Orbits" and excitable limit cycles. In: *Physical Review Letters* 92 (2004), Nr. 7, S. 073901

[80] Martinez, K. ; Lin, A. L. ; Kharrazian, R. ; Sailer, X. ; Swinney, H. L.: Resonance in Periodically Inhibited Reaction-Diffusion Systems. In: *Physica D* 168 (2002)

[81] McNamara, B. ; Wiesenfeld, K.: Therory of stochastic resonance. In: *Physical Review A* 39 (1989), 5, Nr. 9, S. 4854–4869

[82] Mikhailov, A. S. ; Calenbuhr, V.: *From Cells to Societies,Models of Complex Coherent Action.* Springer Verlag, Berlin–Heidelberg–New York, 1990 (Springer Series in Synergetics)

[83] Moss, F. ; McClintock, P. V. E.: *Noise in nonlinear systems Vol.* 1*: Theory of Continuous Fokker-Plank Systems; vol* 2*: Theory of Noise-Induced Processes in Special Applications; vol* 3*: Experiments and Simulations.* Cambridge University Press, 1989

[84] Müller, R. ; Lippert, K. ; Kühnel, A. ; Behn, U.: First-order nonequilibrium phase transition in a spatially extended system. In: *Physical Review E* 56 (1997), S. 2658

[85] Nagumo, J. ; Arimoto, S. ; Yoshizawa, S.: An active pulse transmission line simulating nerve axon. In: *Proc. IRE* 50 (1962)

[86] Neiman, A. ; Saparin, P. I. ; Stone, L.: Coherence resonance at noisy precursors of bifurcations in nonlinear dynamical systems. In: *Physical Review E* 56 (1997), Nr. 1, S. 270

[87] Neiman, A. ; Schimansky-Geier, L. ; Cornell-Bell, A. ; Moss, F.: Noise-enhanced phase synchronization in excitable media. In: *Physical Review Letters* 83 (1999)

[88] Ohta, T. ; Mimura, M. ; Kobayashi, R.: Higher-Dimensional Localized Patterns in Excitable Media. In: *Physica D* 34 (1989)

[89] Ojalvo, J. G. ; Sagues, F. ; Sancho, J. M. ; Schimansky-Geier, L.: Noise-enhanced excitability in bistable activator-inhibitor media. In: *Physical Review E* 65 (2001), S. 011105

[90] Panfilov, A. V. ; Müller, S. C. ; Zykov, V. S. ; Keener, J. P.: Elimination of spiral waves in cardiac tissue by multiple electrical shocks. In: *Physical Review E* 61 (2000), S. 4644

[91] Papoulis, A.: *Probability, random variables, and stochastic processes.* McGraw-Hill, 1991

[92] Parrondo, J. M. R. ; Broeck, C. V. ; Buceta, J. ; Rubia, F. J. l.: Noise-Induced spatial patterns. In: *Physica A* 224 (1996), S. 153

[93] Pawula, R. F.: Approximation of the Linear Boltzmann Equation by the Fokker-Planck Equation. In: *Physical Review* 162 (1967), S. 186

[94] Perc, M.: Spatial coherence resonance in excitable media. In: *Physical Review E* 72 (2005), S. 016207

[95] Pikovsky, A. ; Kurths, J.: Coherence resonance in noise-driven excitable systems. In: *Physical Review Letters* 78 (1997)

[96] Prager, T. ; Naundorf, B. ; Schimansky-Geier, L.: Coupled three-state oscillators. In: *Physica A* 325 (2003), S. 176

[97] Press, W. H. ; Teukolsky, S. A. ; Vetterling, W. T. ; Flannery, B. P.: *Numerical recipes in C, 2–nd edition.* Cambridge University press, 1992

[98] Reimann, P. ; Kawai, R. ; Broeck, C. V. ; Hänggi, P.: Coupled Brownian motors: Anomalous hysteresis and zero-bias negative conductance. In: *Europhysics Letters* 45 (1999), S. 545

[99] Rieke, F. ; Warland, D. ; Stevenick, R. de R. v. ; Bialek, W.: *Spikes: Exploring the neural code.* Cambridge University press, 1996

[100] Rinzel, J. ; Keller, J. B.: Traveling wave solutions of nerve conduction equation. In: *Biophysical Journal* 54 (1973), S. 1313

[101] Risken, H.: *The Fokker-Planck Equation.* Springer Verlag, 1989

[102] Rocsoreanu, C. ; Giurgiteanu, N. ; Georgescu, A.: *The FitzHugh-Nagumo Model: Bifurcation and Dynamics (Mathematical Modeling: Theory and Applications).* Kluwer Academic Publishers, 2000

[103] Rodriguez, R. ; Tuckwell, H. C.: Statistical properties of stochastic nonlinear dynamical models of single spiking neurons and neural networks. In: *Physical Review E* 54 (1996)

[104] Sailer, X.: 2001. – Simulation of resonant pattern formation with the FitzHugh–Nagumo system; masters thesis

[105] Sailer, X. ; Hennig, D. ; Beato, V. ; Engel, H. ; Schimansky-Geier, L.: Regular Patterns in Dichotomically Driven Activator-Inhibitor Dynamics. In: *submitted to Physical Review E* (2005)

[106] Sailer, X. ; Zaks, M. ; Schimansky-Geier, L.: Collective Dynamics in an Ensemble of Globally Coupled FHN Systems. In: *Fluctuation and Noise Letters* 5 (2005)

[107] Sakurai, T. ; Mihaliuk, E. ; Chirila, F. ; Showalter, K.: Design and Control of Wave Propagation Patterns in Excitable Media. In: *Science* 14 (2002), S. 296

[108] Shiino, M.: Dynamical behavior of stochastic systems of infinitely many coupled nonlinear oscillators exhibiting phase transitions of mean-field type: H theorem on asymptotic approach to equilibrium and critical slowing down of order parameter fluctuations. In: *Physical Review A* 36 (1987), Nr. 5, S. 2393

[109] Shinohara, Y. ; Kanamaru, T. ; Suzuki, H. ; Horita, T. ; Aihara, K.: Array-enhanced coherence resonance and forced dynamics in coupled FitzHugh–Nagumo neurons with noise. In: *Physical Review E* 65 (2002)

[110] Shishkin, A. ; Postnov, D.: Stochastic dynamics of FitzHugh–Nagumo Model near the Canard Explosion. In: *Physics and Control,2003. Proceedings* 2 (2003)

[111] Shnol, E. S. L. E. ; Ataullakhanov, F. I.: Complex dynamics of the formation of spatially localized standing structures in the vicinity of saddle-node bifurcations of waves in the reaction-diffusion model of blood clotting. In: *Physical Review E* 70 (2004), S. 032903

[112] Skupin, A.: 2004. – Synchronisationseffekte in neuronalen Netzen; diploma thesis

[113] Smoluchowski, M.: Zur kinetischen Theorie der Brownschen Molekularbewegung und der Suspensionen. In: *Annalen der Physik* 21 (1906), S. 756–780

[114] Softky, W. R. ; Koch, C.: The highly irregular firing of cortical cells is inconsistent with temporal integration of random EPSPs. In: *The Journal of Neuroscience* 13 (1993)

[115] Starmer, C. F. ; Biktashev, V. N. ; Romashko, D. N. ; Stepanov, M. R. ; Makarova, O. N. ; Krinsky, V. I.: Vulnerability in an Excitable Medium: Analytical and Numerical Studies of Initiating Unidirectional Propagation. In: *Biophysical Journal* 65 (1993)

[116] Tass, P. A.: Desynchronizing double-pulse phase resetting and application to deep brain stimulation. In: *Biological Cybernetics* 85 (2001), S. 343–354

[117] Timmermann, L ; Gross, J. ; Dirks, M ; Volkmann, J. ; Freund, H.-J. ; Schnitzler, A.: The cerebral oscillatory network of Parkinsonian resting tremor. In: *Brain* 126 (2002), Nr. 1, S. 199–212

[118] Treutlein, H. ; Schulten, K.: Noise induced limit cycles of the Bonhoeffer-Van der Pol model of neural pulses. In: *Berichte der Bunsengesellschaft* 89 (1986)

[119] Tuckwell, H. C.: *Introduction to theoretical neurobiology Volume 2*. Cambridge University Press, 1988

[120] Turing, A.: The chemical basis of morphogenesis. In: *Philosophical Transactions of the Royal Society of London* 641 (1952)

[121] V. Anishchenko, A. Astakhov T. V. ; Schimansky-Geier, L.: *Chaotic and Stochastic Processes in Dynamic Systems*. New York : Springer Verlag, 2002 (Springer-Series on Synergetics)

[122] Vanag, V. K. ; Epstein, I. R.: Pattern Formation in a Tunable Medium: The Belousov-Zhabotinsky Reaction in an Aerosol OT Microemulsion. In: *Physical Review Letters* 87 (2001)

[123] Vannucchi, F. S. ; Boccaletti, S.: Chaotic spreading of epidemics in complex networks of excitable units. In: *Mathematical Biosciences and engineering* 1 (2004), S. 49

[124] Volkov, E. I. ; Ullner, E. ; Zaikin, A. A. ; Kurths, J.: Oscillatory amplification of stochastic resonance in excitable systems. In: *Physical Review E* 68 (2003)

[125] Watanabe, A. ; Bullock, T. H.: Modulation of Activity of One Neuron by Subthreshold Slow Potentials in Another in Lobster Cardiac Ganglion. In: *The Journal of General Physiology* 432 (1960), S. 1031–1045

[126] Welsh, J. P. ; Ahn, E. S. ; Placantonakis, D. G.: Is autism due to brain desynchronization? In: *International Journal of Developmental Neuroscience* 23 (2005), S. 253–263

[127] Wünsche, H. J. ; Brox, O. ; Radziunas, M. ; Henneberger, F.: Excitability of a semiconductor laser by a two-mode homoclinic bifurcation. In: *Physical Review Letters* 88 (2001), S. 023901

[128] Zaikin, A. A. ; Kurths, J. ; Schimansky-Geier, L.: Doubly Stochastic Resonance. In: *Physical Review Letters* 85 (2000), S. 227

[129] Zaikin, A. A. ; Schimansky-Geier, L.: Spatial patterns induced by additive noise. In: *Physical Review E* 58 (1998), S. 4355

[130] Zaks, M. ; Neimann, A. B. ; Feistel, S. ; Schimansky-Geier, L.: Noise controlled oscillations and their bifurcations in coupled phase oscillators. In: *Physical Review E* 68 (2003)

[131] Zaks, M. ; Sailer, X. ; Schimansky-Geier, L. ; Neiman, A.: Noise induced complexity: From subthreshold oscillations to spiking in coupled excitable systems. In: *CHAOS* 15 (2005), S. 026117

[132] Zheng, Q.: 2004. – MomCumConvert: A Package for Conversion Between Moments and Cumulants, see: *http://library.wolfram.com/infocenter/MathSource/807/*

[133] Zhou, C. ; Kurths, J. ; Neufeld, Z. ; Kiss, I. Z.: Noise-Sustained Coherent Oscillation of Excitable Media in a Chaotic Flow. In: *Physical Review Letters* 91 (2003), S. 0150601

# Appendix A

# Derivation of the Moment Dynamics

In this chapter we show the details of the calculations for the dynamics of the central moments mentioned in chapter 2 in some generality. We will start with a very easy example in section A.1 and then give the results for more complicated dynamics in section A.2.

## A.1 Systems With One Variable Per Site

Let us start with considering the following system stochastic differential equations:

$$\dot{x}_i = f(x_i, \langle x \rangle) + g(x_i)\xi_i(t) \qquad i = 1..N \tag{A.1}$$

Here $\langle x \rangle = \lim_{N\to\infty} \sum_{i=1}^{N} x_i$ is the average x value of the $N$ systems in the limit of large $N$.

For ease of reading we drop the argument $\langle x \rangle$ of the functions $f$ and $g$ as well as the indices of $x$. In order to derive the equations of motion for the central moments we assume that the variable $x$ at time $t = 0$ has the value $x_0$. We now look at the following quantity:

$$\begin{aligned} x^n - x_0^n &= \Big[x_0 + \int_0^t f(x,t')dt' + \int_0^t g(x,t')dW\Big] - x_0^n \\ &= \Big[x_0 + \int_0^t \Big\{f(x_0,t') + f'(x_0,t)(x-x_0) + \frac{1}{2}f''(x_0,t)(x-x_0)^2 \\ &+ \ldots\Big\}dt' + \int_0^t \Big\{g(x_0,t') + g'(x_0,t')(x-x_0) \\ &+ \frac{1}{2}g''(x_0,t')(x-x_0)^2 + \ldots\Big\}dW\Big]^n - x_0^n \end{aligned} \tag{A.2}$$

Here we have performed a Taylor's expansion of the functions $f$ and $g$ around the initial value $x_0$. The prime behind the functions $f$ and $g$ denotes a derivation with respect to the argument $x$ and $W$ is a Wiener process. We now iteratively insert the expression A.3 with $n = 1$:

$$\begin{aligned}
x^n - x_0^n &= \Big[x_0 + \int_0^t dt' f(x_0,t') + \int_0^t dt' f'(x_0,t') \int_0^{t'} dt'' f(x_0,t'') \\
&+ \int_0^t dt' f'(x_0,t') \int_0^{t'} dt'' f'(x_0,t'')(x - x_0) + \dots \\
&+ \int_0^t dt' f'(x_0,t') \int_0^{t'} dW g(x_0,t) + \dots \\
&+ \int_0^t dt' f''(x_0,t') \Big\{ \int_0^t dt' f(x_0,t') + \dots \Big\}^2 + \dots \\
&+ \int_0^t dW g(x_0,t') + \int_0^t dW g'(x_0,t') \int_0^{t'} dt'' f(x_0,t'') \dots \\
&+ \int_0^t dW g'(x_0,t') \int_0^{t'} dW' g(x_0,t'') \\
&+ \int_0^t dW g'(x_0,t') \int_0^{t'} dW' g'(x_0,t'')(x - x_0) + \dots \Big]^n \\
&- x_0^n
\end{aligned} \tag{A.3}$$

By further iterative insertion of eq. A.3 only the known functions $f(x_o, t)$ and $g(x_0, t)$ (and their derivatives) as well as the Langevin forces remain in the equation.

Assuming molecular chaos (see chapter 2 for discussion) we now take a look at the average of the $N$ individual systems:

$$\begin{aligned}
\langle x^n - x_0^n \rangle &= \Big\langle \Big[x_0 + \int_0^t dt' f(x_0,t) + \int_0^t dW \int_0^{t'} dW' g(x_0,t') g'(x_0,t) \\
&+ \int_0^t dW g(x_0,t) + \dots \Big]^n - x_0^n \Big\rangle \\
&= \Big\langle \Big[x_0 + \int_0^t dt' \sum_{m=0}^{\infty} \frac{x_0^m}{m!} f^{(m)}(0) \\
&+ \int_0^t dW W \sum_{m=0}^{\infty} \frac{x_0^m}{m!} \big(gg'\big)^{(m)}(0) \\
&+ \int_0^t dW 2W \sum_{m=0}^{\infty} \frac{x_0^m}{m!} \big(g^2\big)^{(m)}(0) + \dots \Big]^n - x_0^n \Big\rangle
\end{aligned} \tag{A.4}$$

where the number 2 in the last line stems from the fact that:

$$\int_0^t g(x_0,t')dt' \int_0^t g(x_0,t'')dt'' = 2\int_0^t \int_0^{t'} g(x_0,t')g(x_0,t'')dt'dt'' \tag{A.5}$$

It is now that the question of how to interpret eq. A.1 arises. We decide here to use the Stratonovich interpretation.

For calculating the temporal derivative of the moments $M$ it is necessary to look at eq. A.4 in the limit $t \to 0$. Only the terms explicitely given are of order $dt$. All others vanish during the process of averaging or are of higher order (cf. eq. A.3). This can be seen by looking at an example of such a term with Langevin forces:

$$\left\langle \int_0^t \dots dW \int_0^{t'} \dots dW' \int_0^{t''} \dots dW'' \int_0^{t'''} \dots dW''' \right\rangle \tag{A.6}$$

which contributes proportional to $t^2$. Terms in A.4 without Langevin forces scale with $dt^n$ where $n$ is the number of integrals.

Terms of order higher than $dt$ vanish when calculating the temporal derivative. We therefore arrive at the following expression for the dynamics of the moments:

$$\begin{aligned}
\dot{M}_n &= \frac{\partial M_n}{\partial t} = \lim_{t\to 0} \frac{\langle x^n - x_0^n \rangle}{t} \\
&= \sum_{m=0}^{\infty} n \frac{M_{n-1+m}}{m!} \left[ f^{(m)}|_{x=\langle x\rangle} + T(gg')^{(m)}|_{x=\langle x\rangle} \right] \\
&+ \sum_{m=0}^{\infty} n(n-1) \frac{M_{n-2+m}}{m!} T(g^2)^{(m)}|_{x=\langle x\rangle} \\
&= n(n-1) M_{n-2} T g^2|_{x=\langle x\rangle} \\
&+ \sum_{m=0}^{\infty} \frac{n}{m!} M_{n-1+m} \left( f^{(m)}|_{x=\langle x\rangle} + \left(1 + 2\frac{n-1}{m+1}\right) T(gg')^{(m)}|_{x=\langle x\rangle} \right)
\end{aligned} \tag{A.7}$$

This is what we were heading for. Together with the formula for the dynamics of the mean given in chapter 2 this formula provides a complete though often infinite system to describe the behavior of $N$ identical systems which each can be described by the dynamics A.1.

Approximation techniques that make the system finite are discussed in chapter 2.

## A.2 Systems With Many Variables Per Site

It is cumbersome but straightforward to repeat the calculations for systems in which each individual unit is described by more than one variable and each such

variable has a noise source of its own. Also it is possible to assume additional dependencies of the functions corresponding to $g$ in A.1 on the mean values. Last but not least the calculations can be done for the central moments $\mu$ instead of the moments $M$. The corresponding system of Langevin equations reads:

$$\begin{aligned} x_{1,i} &= f_1(x_{1,i}..y_{J,i}, \langle x_1\rangle..\langle x_N\rangle) + g_1(x_{1,i}..y_{J,i}, \langle x_1\rangle..\langle x_N\rangle)\xi_{1,i}(t) \\ x_{2,i} &= f_2(x_{1,i}..y_{J,i}, \langle x_1\rangle..\langle x_N\rangle) + g_2(x_{1,i}..y_{J,i}, \langle x_1\rangle..\langle x_N\rangle)\xi_{2,i}(t) \\ &\vdots \\ x_{J,i} &= f_J(x_{1,i}..y_{J,i}, \langle x_1\rangle..\langle x_N\rangle) + g_J(x_{1,i}..y_{J,i}, \langle x_1\rangle..\langle x_N\rangle)\xi_{N,i}(t) \\ & \qquad\qquad\qquad\qquad\qquad\qquad\qquad\qquad i = 1..N \end{aligned} \tag{A.8}$$

With this system of equations we describe an ensemble of $N$ identical particles. The dynamics of each such particle is given by a $J$ dimensional system of equations.

The dynamics of the mean of the variables is given by:

$$\begin{aligned} \dot{\langle x_j\rangle} &= \sum_{k1..k_J=0}^{\infty} \frac{\mu_{k_1,...,k_J}}{k_1!,\ldots,k_J!}\Big[f_j + \\ &+ \sum_{l=1}^{J} \delta_{\xi_j,\xi_l}\sqrt{T_jT_l}g_jg_l^{(\overbrace{0,...0}^{l-1},1,0,...,0)}\Big]^{(k_1,...,k_J)}\Big|_{x_1=\langle x\rangle_!,...,x_J=\langle x\rangle_J} \end{aligned} \tag{A.9}$$

Here $\delta_{\xi_j,\xi_l}$ is one if there are identical noise realizations in the $l$-th and the $m$-th part of eq. A.9 and zero otherwise. That means that the last part of the sum is different from the usual Stratonovich shift only if there are added equal noise realizations to at least two different variables of the individual units.

The moment dynamics for this system is given by:

$$\begin{aligned}
\mu_{n_1\ldots n_J} &= \sum_{i=1}^{J} n_i \sum_{k_1\ldots k_J}^{\infty} \frac{\mu_{n_1+k_1,n_2+k_2,\ldots n_i-1+k_i\ldots n_J+k_J}}{k_1!k_2!\ldots k_J!} \\
&\quad \left(f_i + \sum_{j=1}^{J} \sqrt{T_iT_j}\delta_{\xi_i,\xi_j} g_i g_j^{(\overbrace{0,\ldots 0}^{j-1},1,0,\ldots,0)}\right)^{(k_1,\ldots,k_J)}_{x_1=\langle x_1\rangle\ldots x_J=\langle x_J\rangle} \\
&+ \sum_{i=1}^{J} n_i(n_i-1)T_i \sum_{k1\ldots k_J}^{\infty} \frac{\mu_{n_1+k_1,n_2+k_2,\ldots n_i-2+k_i\ldots n_J+k_J}}{k_1!k_2!\ldots k_J!} \left(g_i^2\right)^{(k_1,\ldots,k_J)}_{x_1=\langle x_1\rangle\ldots x_J=\langle x_J\rangle} \\
&+ \sum_{l,m=1|l<m}^{J} \delta_{\xi_l,\xi_m} n_l, n_m \sqrt{T_lT_m} \sum_{k1\ldots k_J}^{\infty} \frac{\mu_{n_1+k_1,n_2+k_2,\ldots n_l-2+k_l\ldots n_m-1+k_m\ldots n_J+k_J}}{k_1!k_2!\ldots k_J!} \\
&\quad \left(2T_l g_l g_m\right)^{k_1,\ldots k_J}_{x_1=\langle x_1\rangle\ldots x_J=\langle x_J\rangle}
\end{aligned} \tag{A.10}$$

where the last two lines vanish if the noise realizations in the different variables are different. When applying this equation and eq. A.9 to concrete problems note that due to the normalization $\mu_{0,\ldots,0} = 1$ and due to the definition of the central moments $\mu_{0,\ldots,i,\ldots,0} = 0$.

## A.3 The Relation Between Moments, Central Moments, and Cumulants

When applying the approximations mentioned in section 2.2 to real problems we often encounter the problem of how to express the cumulants of a distribution by its moments (also by its central moments) and vice versa. No simple formula exits for solving this problem but we give here a method of how to do that that is related to a method introduced by van Kampen (see [39] and references therein). There also exits free software for these conversions [132]. We will also give some explicit relations that are applied in the course of this work.

Let us assume that we are looking for the description of the cumulant $\kappa_{n_1,..n_N}$ of a distribution $p(x_1,\ldots,x_N)$ in terms of its moments. It is given by the following expression:

$$\kappa_{n_1,..n_N} = \sum_{q=0}^{N-1}(-1)^q q! C_q \tag{A.11}$$

The $C_q$ are obtained as follows:

- For each $n_i > 1$ in $\kappa_{n_1,..n_N}$ introduce a new variable $x_{N+1}$, e.g. $\kappa_{2,1} \rightarrow \kappa_{1,1,1}$, and evaluate $\kappa_{n_1,...n_i-1,...n_N,n_{N+1}}$ instead. In the final expression reverse this ($M_{1,1,1} \rightarrow M_{2,1}$).
- Write down a product of $q$ terms $M_{0...0,1,0,...0}M_{0...0,1,0,...0}\ldots M_{0...0,1,0,...0}$ where the number of "1"s is equal to the sum over the $N_j$ ($j = 1\ldots N$).
- Call the sum of all possible combinations $C_q(x_1,\ldots,x_N)$.

This procedure is cumbersome for high order cumulants. We give here some selected examples for the conversions.

$$\begin{aligned} M_1 &= \kappa_1 \\ M_2 &= \kappa_1^2 + \kappa_2 \\ M_3 &= \kappa_1^3 + \kappa_1\kappa_2 + \kappa_3 \\ M_4 &= \kappa_1^4 + 6\kappa_1^2\kappa_2 + 3\kappa_2^2 + 4\kappa_1\kappa_3 + \kappa_4 \end{aligned} \tag{A.12}$$

And for the central moments:

$$\begin{aligned} \mu_1 &= 0 \\ \mu_2 &= \kappa_2 \\ \mu_3 &= \kappa_3 \\ \mu_4 &= \kappa_4 + 3\kappa_2^2 \end{aligned} \tag{A.13}$$

We also want to give some relations between central and non-central moments:

$$\begin{aligned}
\mu_1 &= 0 \\
\mu_2 &= M_2 - M_1^2 \\
\mu_3 &= M_3 + 3M_1^3 - 3M_1M_2 - M_1^3 \\
\mu_4 &= M_4 - 3M_1^4 + 6M_1^2M_2 - 4M_1M_3
\end{aligned} \tag{A.14}$$

For two-variable systems:

$$\begin{aligned}
M_{1,0} &= \kappa_{1,0} \\
M_{0,1} &= \kappa_{0,1} \\
M_{2,0} &= \kappa_{1,0}^2 + \kappa_{2,0} \\
M_{1,1} &= \kappa_{1,1} + \kappa_{0,1}\kappa_{1,0} \\
M_{2,0} &= \kappa_{1,0}^2 + \kappa_{2,0} \\
M_{3,0} &= \kappa_{1,0}^3 + 3\kappa_{1,0}\kappa_{2,0} + \kappa_{3,0} \\
M_{2,1} &= \kappa_{0,1}\kappa_{1,0}^2 + 2\kappa_{1,0}\kappa_{1,1} + \kappa_{0,1}\kappa_{2,0} + \kappa_{2,1} \\
M_{1,2} &= \kappa_{1,0}\kappa_{0,1}^2 + 2\kappa_{0,1}\kappa_{1,1} + \kappa_{1,0}\kappa_{0,2} + \kappa_{1,2} \\
M_{0,3} &= \kappa_{0,1}^3 + 3\kappa_{0,1}\kappa_{0,2} + \kappa_{0,3}4\kappa_{1,0}\kappa_{3,0} + \kappa_{4,0} \\
M_{4,0} &= \kappa_{1,0}^4 + 6\kappa_{1,0}^2\kappa_{2,0} + 3\kappa_{2,0}^2 \\
M_{3,1} &= \kappa_{0,1}\kappa_{1,0}^3 + 3\kappa_{1,0}^2\kappa_{1,1} + 3\kappa_{1,0}\kappa_{0,1}\kappa_{2,0} + 3\kappa_{2,0}\kappa_{1,1} + 3\kappa_{1,0}\kappa_{2,1} + \kappa_{3,0}\kappa_{0,1} + \kappa_{3,1} \\
M_{2,2} &= \kappa_{1,0}^2\kappa_{0,1}^2 + \kappa_{0,2}\kappa_{1,0}^2 + 4\kappa_{1,0}\kappa_{0,1}\kappa_{1,1} + 2\kappa_{1,1}^2 + 2\kappa_{1,0}\kappa_{1,2} + \kappa_{0,1}\kappa_{2,0} \\
&+ \kappa_{0,2}\kappa_{2,0} + 2\kappa_{0,1}\kappa_{2,1} + \kappa_{2,2} \\
M_{1,3} &= \kappa_{1,0}\kappa_{0,1}^3 + 3\kappa_{0,1}^2\kappa_{1,1} + 3\kappa_{0,1}\kappa_{1,0}\kappa_{0,2} + 3\kappa_{0,2}\kappa_{1,1} + 3\kappa_{0,1}\kappa_{1,2} + \kappa_{0,3}\kappa_{1,0} + \kappa_{1,3} \\
M_{0,4} &= \kappa_{0,1}^4 + 6\kappa_{0,1}^2\kappa_{0,2} + 3\kappa_{0,2}^2
\end{aligned} \tag{A.15}$$

The conversions become much easier for the central moments:

$$\begin{aligned}
M_{1,0} &= 0 & M_{1,2} &= \kappa_{1,2} \\
M_{0,1} &= 0 & M_{0,3} &= \kappa_{0,3} \\
M_{2,0} &= \kappa_{2,0} & M_{4,0} &= 3\kappa_{2,0}^2 + \kappa_{4,0} \\
M_{1,1} &= \kappa_{1,1} & M_{3,1} &= 3\kappa_{1,1}\kappa_{2,0} + \kappa_{3,1} \\
M_{2,0} &= \kappa_{2,0} & M_{2,2} &= 2\kappa_{1,1}^2 + \kappa_{2,0}\kappa_{0,2} + \kappa 2, 2 \\
M_{3,0} &= \kappa_{3,0} & M_{1,3} &= 3\kappa_{1,1}\kappa_{0,2} + \kappa_{1,3} \\
M_{2,1} &= \kappa_{2,1} & M_{0,4} &= 3\kappa_{0,2}^2 + \kappa_{0,4}
\end{aligned} \tag{A.16}$$

## A.4 The Relation Between the Central Moments of the Gaussian Distribution

The Gaussian distribution in $N$ dimensions reads:

$$P(x_1,\ldots,x_N) = \frac{1}{(2\pi)^{N/2}\sqrt{2T_{i,j}}} e^{\sum_{i,j=0}^{N}\frac{1}{2T_{i,j}}(x_i-a_i)(x_j-a_j)} \tag{A.17}$$

Its characteristic function is given as the Fourier transform of the probability density:

$$C(u_1,\ldots,u_N) = e^{\sum_{m,n=0}^{N} ia_ju_j - \sum_{m,n=0}^{N} T_{n,m}u_nu_m} \tag{A.18}$$

With the characteristic function we can compute the moments using the relation (cf. 2.4)

$$M_{n_1,\ldots,n_N} = \left(\frac{\partial}{\partial iu_1}\right)^{n_1} \ldots \left(\frac{\partial}{\partial iu_N}\right)^{n_1} C(u_1,\ldots,u_N)|_{u_1=\cdots=u_N=0} \tag{A.19}$$

The odd order central moments of the Gaussian distribution are all zero. The even order moments can be expressed by the second one. We give here some examples:

$$\begin{aligned} \mu_4 &= 3\mu_2^2 \\ \mu_6 &= 15\mu_2^3 \end{aligned} \tag{A.20}$$

For the two-variable Gaussian distribution the following examples are used in the present work:

$$\begin{aligned} \mu_{3,1} &= 3\mu_{2,0}\mu_{1,1} & \mu_{4,0} &= 3\mu_{2,0}^2 \\ \mu_{5,1} &= 15\mu_{2,0}^2\mu_{1,1} & \mu_{6,0} &= 15\mu_{2,0}^3 \end{aligned} \tag{A.21}$$

# Appendix B

# The Complex Ginzburg–Landau Equation for the FitzHugh–Nagumo Model

**Continuum Case**

We rewrite the spatially extended version of the FHN eq. 6.6 in terms of deviations from the steady state $(x_0\ y_0)$.

$$\begin{aligned} \tilde{x} &= x - x_0 \\ \tilde{y} &= y - y_0 \end{aligned} \tag{B.1}$$

In the excitable case the FHN has exactly one fixed point and that is stable. Its explicit form is given in eq. 3.3. The FHN now reads (for ease of reading we drop the tildes above $x$ and $y$:

$$\begin{aligned} \frac{\partial x}{\partial t} &= Ax + Bx^2 + Cx^3 - y + D_x \frac{\partial^2 x}{\partial r^2} \\ \frac{\partial y}{\partial t} &= \epsilon(x - ay) + D_y \frac{\partial^2 y}{\partial r^2} \end{aligned} \tag{B.2}$$

with the coefficients $A$, $B$, $C$ given by:

$$\begin{aligned} A &= 1 - 3x_0^2 \\ B &= -3x_0 \\ C &= -1 \end{aligned} \tag{B.3}$$

We assume that our stable homogeneous solution becomes unstable at the critical parameter value $d_c$. In chapter 6 the parameter $d$ is the intensity of the dichotomous switching. Recall that $x_0 = x_0(d)$. In the deterministic case this is the offset

of the linear nullcline and it was labeled $b$. We introduce a new variable $\mu$ that measures the distance to the critical value:

$$d = d_c(1 + \mu) \tag{B.4}$$

We want to investigate the system in the vicinity of the critical value and therefore assume $\mu \ll 1$.

We now rewrite eq. B.2 in matrix notation:

$$\left(\frac{\partial}{\partial t} - \mathbf{D}\frac{\partial^2}{\partial r^2} - \mathbf{L}\right)\mathbf{u} = \mathbf{Muu} + \mathbf{Nuuu} \tag{B.5}$$

with the the vector $\mathbf{u} = \begin{pmatrix} x & y \end{pmatrix}^T$ and the matrices

$$\begin{aligned} \mathbf{L} &= \begin{pmatrix} A & -1 \\ \epsilon & -\epsilon a \end{pmatrix} & \mathbf{D} &= \begin{pmatrix} D_x & 0 \\ 0 & D_y \end{pmatrix} \\ \mathbf{M} &= \begin{pmatrix} B & 0 \\ 0 & 0 \end{pmatrix} & \mathbf{N} &= \begin{pmatrix} C & 0 \\ 0 & 0 \end{pmatrix} \end{aligned} \tag{B.6}$$

Next we expand the matrix operators as well as the vector $\mathbf{u}$ in terms of the small parameter $\mu$ which measures the distance to the critical parameter $d_c$:

$$\begin{aligned} \mathbf{u} &= \mu\mathbf{u}_1 + \mu^2\mathbf{u}_2 + \dots \\ \mathbf{L} &= \mathbf{L}_0 + \mu\mathbf{L}_1 + \mu^2\mathbf{L}_2 \dots & \mathbf{D} &= \mathbf{D}_0 + \mu\mathbf{D}_1 + \mu^2\mathbf{D}_2 + \dots \\ \mathbf{M} &= \mathbf{M}_0 + \mu\mathbf{M}_1 + \mu^2\mathbf{M}_2 \dots & \mathbf{N} &= \mathbf{N}_0 + \mu\mathbf{N}_1 + \mu^2\mathbf{N}_2 + \dots \end{aligned} \tag{B.7}$$

We are looking for deviations in $d$ from the bifurcation point. The operators $\mathbf{D}$ and $\mathbf{N}$ do not change with a change in $d$. Only $\mathbf{L}$ via the influence of $A = 1 - 3\tilde{x}_0^2(d)$ and $\mathbf{M}$ via $B = -3x_0(d)$ depend on it. Therefore, only for the operators $\mathbf{L}$ and $\mathbf{M}$ the higher order terms are of importance.

We introduce new scaled time and space variables:

$$\begin{aligned} \tau_1 &= \mu t & s_1 &= \mu r \\ \tau_2 &= \mu^2 t & s_2 &= \mu^2 r \end{aligned} \tag{B.8}$$

Directly at the bifurcation we can treat them a mutually independent. This has implications for the following operators:

$$\begin{aligned} \frac{\partial}{\partial t} &\rightarrow \frac{\partial}{\partial t} + \mu\frac{\partial}{\partial \tau_1} + \mu^2\frac{\partial}{\partial \tau_2} + O(\mu^3) \\ \frac{\partial^2}{\partial r^2} &\rightarrow \frac{\partial^2}{\partial r^2} + 2\mu\frac{\partial^2}{\partial r \partial s_1} + \mu^2\frac{\partial^2}{\partial s_1^2} + 2\mu^2\frac{\partial^2}{\partial r \partial s_2} + O(\mu^3) \end{aligned} \tag{B.9}$$

Plugging eqs. B.7, B.8, and B.9 into eq. B.5

$$\left(\frac{\partial}{\partial t}+\mu\frac{\partial}{\partial \tau_1}+\dots-\frac{\partial}{\partial r}-2\mu\frac{\partial}{\partial s_1\partial r}-\dots-\mathbf{L}_0-\mu\mathbf{L}_1-\dots\right)(\mu\mathbf{u}_1+\mu^2\mathbf{u}_2+\dots)$$
$$=\mu^2\mathbf{M}_0\mathbf{u}_1\mathbf{u}_1+\mu^3(2\mathbf{M}_0\mathbf{u}_1\mathbf{u}_2+\mathbf{N}_0\mathbf{u}_1\mathbf{u}_1\mathbf{u}_1)+O(\mu^4) \tag{B.10}$$

and sorting by the different power of $\mu$ yields the set of equations

$$\left(\frac{\partial}{\partial t}-\frac{\partial^2}{\partial r^2}-\mathbf{L}_0\right)\mathbf{u}_\nu=\mathbf{P}_\nu \qquad \nu=1,2,\dots \tag{B.11}$$

where the first few $\mathbf{P}_\nu$ are given by:

$$\begin{aligned}
(\mu): \quad \mathbf{P}_1 &= \mathbf{0}\\
(\mu^2): \quad \mathbf{P}_2 &= \left(2\mathbf{D}_0\frac{\partial^2}{\partial s_1\partial r}+\mathbf{L}_1-\frac{\partial}{\partial\tau_1}\right)\mathbf{u}_1+\mathbf{M}_0\mathbf{u}_1\mathbf{u}_1\\
(\mu^3): \quad \mathbf{P}_3 &= \left(2\mathbf{D}_0\frac{\partial^2}{\partial s_1\partial r}+\mathbf{L}_1-\frac{\partial}{\partial\tau_1}\right)\mathbf{u}_2\\
&+ \left(2\mathbf{D}_1\frac{\partial^2}{\partial r\partial s_1}+2\mathbf{D}_0\frac{\partial^2}{\partial r\partial s_2}+\mathbf{D}_0\frac{\partial^2}{\partial s_1^2}+\mathbf{L}_2-\frac{\partial}{\partial\tau_2}\right)\mathbf{u}_1\\
&+ 2\mathbf{M}_0\mathbf{u}_1\mathbf{u}_2+\mathbf{N}_0\mathbf{u}_1\mathbf{u}_1\mathbf{u}_1
\end{aligned} \tag{B.12}$$

We stop after the third power of $\mu$ as we will see later that this is sufficient for our analysis. From here on we will apply the following procedure: We solve eq. B.11 successively for increasing $\nu$. With the solution for $\nu=1$ we can explicitely write down $P_2$ and so on. According to Fredholm's theorem eq. B.11 has a unique solution iff the scalar product

$$\langle VP_\nu\rangle=\int_{-\infty}^{\infty}(V_xP_x+V_yP_y)\,dr=0 \tag{B.13}$$

where $V=(V_x\ V_y)^t)$ is the left eigenvector to the right hand side of eq. B.11 and $P_x$ and $P_y$ are the components of $\mathbf{P}_\nu$. This condition is called the solvability condition. We will see that the solvability condition for $\nu=3$ yields the Ginzburg-Landau equation we are after.

Before we start we want to give two values that we will need later on.

$$\begin{aligned}
k_c^2 &= \frac{AD_y-a\epsilon D_x}{2D_xD_y}\\
A_c &= -a\epsilon\frac{D_x}{D_y}\pm 2\sqrt{\epsilon\frac{D_x}{D_y}}
\end{aligned} \tag{B.14}$$

$k_c^2$ which can be obtained by standard Turing bifurcation theory is the critical wavelength of the perturbations and $A_c$ is the value of $A$ at the bifurcation.

We are interested in the slowly varying part of $\mathbf{u}$ and therefore set $\frac{\partial}{\partial t} = 0$. Eq. B.11 for the first power of $\mu$ now becomes:

$$\mathbf{L}_0\mathbf{u}_1 + \mathbf{D}_0\frac{\partial^2}{\partial r^2}\mathbf{u}_1 = 0 \tag{B.15}$$

The solution for this equation is well known:

$$\mathbf{u}_1 = \mathbf{U}\left(We^{ik_c r} + c.c.\right) \tag{B.16}$$

Where c.c. stands for the complex conjugate. $k_c$ is the critical wavelength for the Turing bifurcation which is given in eq. 6.19. All other wavelengths quickly decay at the onset of the bifurcation. The function $W$ may well depend on the remaining variables:

$$W = W(\tau_1, \tau_2, s_1, s_2) \tag{B.17}$$

Insertion of eq. B.16 into eq. B.15 yields

$$\mathbf{u}_1 = \begin{pmatrix} 1 \\ A_c - D_x k_c^2 \end{pmatrix}\left(We^{ik_c r} + c.c.\right) \tag{B.18}$$

which we insert into eq. B.11 for $\nu = 2$. It now becomes an equation for $\mathbf{u}_2$, only. Now it is time to look for the eigenvector to the adjoint operator on the left hand side of eq. B.11. It can easily be determined:

$$V = \begin{pmatrix} 1 \\ \frac{1}{\epsilon a + D_y k_c^2} \end{pmatrix} e^{ik_c r} \tag{B.19}$$

We are now ready to apply the solvability condition for $\nu = 2$. We apply the expressions for $k_c$ and $A_c$ (eqs. B.14) and after some algebra the solvability condition boils down to

$$A_1 W + C W_{\tau_1} = 0 \tag{B.20}$$

where $W_{\tau_1}$ denotes the derivative of $W$ with respect to $\tau_1$ (We will later use the same notation for $\tau_2$, $s_1$, and $s_2$.) and $A_1$ is the upper left matrix component of $\mathbf{L}$. The explicit form of the real constant $C$ is here, as we will see soon, of no importance.

The solution of equation B.20 is well known. Neglecting the trivial as well as divergent solutions we set

$$W = W_0 e^{ik_c r + i\omega_1 \tau_1} \tag{B.21}$$

This leads to

$$A_1 + i\omega_1 C = 0 \tag{B.22}$$

Solving this equation separately for the real and the imaginary part yields $A_1 = 0$. Also, we conclude that there is no dependency of $W$ on $\tau_1$.

The solvability condition did not yield the amplitude equation we are looking for. We thus have go on to $\nu = 3$. Therefore we first have to calculate $\mathbf{u}_2$. We use the ansatz

$$\begin{aligned} \mathbf{u}_2 &= \begin{pmatrix} x_2 \\ y_2 \end{pmatrix} = \begin{pmatrix} a_0 \\ b_0 \end{pmatrix} + \begin{pmatrix} a_1 \\ b_1 \end{pmatrix} e^{ik_c r} + \begin{pmatrix} a_1^* \\ b_1^* \end{pmatrix} e^{-ik_c r} \\ &+ \begin{pmatrix} a_2 \\ b_2 \end{pmatrix} e^{2ik_c r} + \begin{pmatrix} a_2^* \\ b_2^* \end{pmatrix} e^{-2ik_c r} \end{aligned} \tag{B.23}$$

where the star denotes the complex conjugate and plug it together with eq. B.18 into eq. B.11 for $\nu = 2$. We find by comparison of coefficients that the ansatz solves the equation for the following coefficients:

$$\begin{aligned} a_0 &= a\tfrac{2B|W|^2}{1-aA} \qquad & b_0 &= \tfrac{2B|W|^2}{1-aA} \\ a_1 &= 0 & b_1 &= 2D_x i k_c W_s \\ a_2 &= \frac{BW^2(\epsilon a + 4D_y k_c^2)}{\epsilon - (\epsilon a + 4D_y k_c^2)(A - 4D_x k_c^2)} \\ b_2 &= (A - 4D_x k_c^2) a_2 + BW^2 \end{aligned} \tag{B.24}$$

We can now proceed to eq. B.11 with $\nu = 3$. The solvability condition $\langle \mathbf{VP}_3 \rangle$ yields the sought-after Complex Ginzburg–Landau Equation:

$$F W_{\tau_1} = \alpha W_{s_1 s_1} + \beta W + \gamma |W|^2 W \tag{B.25}$$

with the coefficients

$$\begin{aligned} F &= 1 + \frac{A_c + 2\tilde{D}_x}{2\tilde{D}_y - \epsilon\, a}\,, \\ \alpha &= D_x + 2(cos(k_c) - 1) \left\{ \frac{(A_c + 2\tilde{D}_x) D_y}{2\tilde{D}_y - \epsilon\, a} \left[1 + 4D_x\right] \right. \\ &- \left. 4 \left[ D_x + (A_c + 2\tilde{D}_x)^2 D_y \right] \frac{(A_c + 2\tilde{D}_x) D_y + 2\tilde{D}_y - \epsilon\, a}{\epsilon\, a + (2\tilde{D}_y - \epsilon\, a)(A_c + 2\tilde{D}_x)^2 D_y} \right\}, \\ \beta &= A - A_c\,, \\ \delta &= 2B \left[ \frac{2aB}{1 - aA} + \frac{(\epsilon\, a - 2\tilde{\tilde{D}}_y) B}{\epsilon - (\epsilon\, a - 2\tilde{\tilde{D}}_y)(A_c + 2\tilde{\tilde{D}}_x)} \right], \end{aligned} \tag{B.26}$$

and the abbreviations

$$\tilde{D}_{x,y} = 2(\cos(k_c) - 1) D_{x,y}\,, \qquad \tilde{\tilde{D}}_{x,y} = 2(\cos(2k_c) - 1) D_{x,y} \tag{B.27}$$

The terms depending on $s_2$ have dropped out.

### Discrete Case

The discrete case can be treated similar to the continuum case. We now investigate the set of equations:

$$\begin{aligned} \dot{x}_n &= Ax_n + Bx_n^2 + Cx_n^3 - y_n + D_x[x_{n+1} - 2x_n + x_{n-1}] \\ \dot{y}_n &= \epsilon(x_n + ay_n) + D_y[y_{n+1} - 2y_n + y_{n-1}] \end{aligned} \tag{B.28}$$

Analogous to the continuum case we introduce new, scaled time and space variables:

$$\tau = \mu^2 t \qquad s = \mu r \tag{B.29}$$

In eq. B.8 we have given more new variables. They will not play a role in the discrete case, too, and we neglect them already at this stage. $\mathbf{u}_n = \mu\mathbf{u}_{n,1} + \mu\mathbf{u}_{n,2} + \ldots$ is now a discrete vector. We index it by the site $n$ in the grid.

The analogon to eq. B.11 (with grid size equal to one) now reads:

$$\left(\frac{\partial}{\partial t} - \mathbf{D}[\mathbf{u}_{n+1,\nu} + \mathbf{u}_{n-1,\nu} - 2\mathbf{u}_{n,\nu}] - \mathbf{L}_0\right)\mathbf{u}_{n,\nu} = \mathbf{P}_\nu \qquad \nu = 1, 2, \ldots \tag{B.30}$$

With the ansatz $\mathbf{u}_{n,1} = \mathbf{U}_d(W_s e^{ik_c r} + c.c.)$ we can easily determine

$$\mathbf{u}_{n,1} = \begin{pmatrix} 1 \\ A + 2D_x(cos(k_c) - 1) \end{pmatrix}\left(W_s e^{ik_c n} + c.c.\right) \tag{B.31}$$

For the solvability condition we need the left eigenvector

$$V_d = \begin{pmatrix} 1 \\ -\epsilon a + 2D_y(cos(k_c) - 1) \end{pmatrix}\left(W_s e^{ik_c n} + c.c.\right) \tag{B.32}$$

Again, we have to go to order $\nu = 3$ for obtaining the Complex Ginzburg–Landau Equation. The solution for $\mathbf{u}_{n,2}$ is given by

$$\begin{aligned} \mathbf{u}_{n,2} &= \begin{pmatrix} x_{n,2} \\ y_{n,2} \end{pmatrix} = \begin{pmatrix} \tilde{a}_0 \\ \tilde{b}_0 \end{pmatrix} + \begin{pmatrix} \tilde{a}_1 \\ \tilde{b}_1 \end{pmatrix} e^{ik_c n} + \begin{pmatrix} \tilde{a}_1^* \\ \tilde{b}_1^* \end{pmatrix} e^{-ik_c n} \\ &+ \begin{pmatrix} \tilde{a}_2 \\ \tilde{b}_2 \end{pmatrix} e^{2ik_c n} + \begin{pmatrix} \tilde{a}_2^* \\ \tilde{b}_2^* \end{pmatrix} e^{-2ik_c n} \end{aligned} \tag{B.33}$$

with

$$\begin{aligned}
\tilde{a}_0 &= \frac{2aB|W_s|^2}{1-aA} \\
\tilde{b}_0 &= \frac{2B|W_s|^2}{1-aA} \\
\tilde{a}_1 &= \frac{2\left(W_{s+1}-W_s\right)\left(e^{ik}-1\right)\left[D_y\left(A+2\tilde{D}_x\right)-D_x\left(\epsilon a-2\tilde{D}_y\right)\right]}{\left(\epsilon a-2\tilde{D}_y\right)\left(A+2\tilde{D}_x\right)-\epsilon} \\
\tilde{b}_1 &= 2D_x\left(W_{s+1}-W_s\right)\left(e^{ik}-1\right)+A\tilde{a}_1+D_x\tilde{a}_1\left(cos(k_c)-1\right) \\
\tilde{a}_2 &= \frac{\left(\epsilon a-2D\tilde{\tilde{D}}_y\right)BW_s^2}{\epsilon-\left(\epsilon a-2\tilde{\tilde{D}}_y\right)\left(A+2\tilde{\tilde{D}}_x\right)} \\
\tilde{b}_2 &= \left(A+2\tilde{\tilde{D}}_x\right)\tilde{a}_2+BW_s^2
\end{aligned} \tag{B.34}$$

and

$$\tilde{D}_{x,y}=2(\cos(k_c)-1)D_{x,y}\,, \qquad \tilde{\tilde{D}}_{x,y}=2(\cos(2k_c)-1)D_{x,y} \tag{B.35}$$

With the solvability condition for $\nu=3$ we finally arrive at

$$F\frac{\partial}{\partial\tau}W_s=\alpha\left(W_{s+1}+W_{s-1}-2W_s\right)+\beta W_s+\delta|W_s|^2W_s \tag{B.36}$$

with the coefficients

$$\begin{aligned}
F &= 1+\frac{A_c+2\tilde{D}_x}{2\tilde{D}_y-\epsilon\,a}\,, \\
\alpha &= D_x+2\left(cos(k_c)-1\right)\Big[\frac{D_y\left(A+2\tilde{D}_x\right)}{2\tilde{D}_y-\epsilon a}\left(1+4D_x\right) \\
&+ 4\left(D_x+D_y\left(A+2\tilde{D}_x\right)^2\right)\frac{D_y\left(A+2\tilde{D}_x\right)-D_x\left(\epsilon a-2\tilde{D}_y\right)}{\left(\epsilon a-2\tilde{D}_y\right)\left(A+2\tilde{D}_x\right)-\epsilon}\Big] \\
\beta &= A_c \\
\delta &= D_x+2\left(\cos(k_c)\right)\left[\frac{2aB}{1-aA}+\frac{\epsilon a-2B\tilde{\tilde{D}}_y}{\epsilon-\left(\epsilon a-2\tilde{\tilde{D}}_y\right)\left(A+2\tilde{\tilde{D}}_x\right)}\right]+3C
\end{aligned} \tag{B.37}$$

Note that in the limit of small lattice spacing $\Delta r$ (which we have set to one) the solution goes, by expanding $cos(k_c\Delta r)=1-0.5(k_c\Delta r)^2$, over into that of the continuum case.

# Acknowledgment

The present work would not have been possible if it were not for the help of many people who I want to thank. It has been a pleasure to have had the opportunity to study this interesting subject. I therefore want to thank Prof. Dr. Lutz Schimansky-Geier who by supervising this work, giving many valuable scientific impulses, and providing a pleasant environment has had a great influence on this dissertation.

I am greatly indebted to all the scientific collaborators I had the enjoyment to work with. Among them I would like to point out Prof. Dr. Harald Engel, Prof. Ryoichi Kawai, PhD, Priv.-Doz. Dr. Dirk Hennig and Priv.-Doz. Dr. Michail Zaks. Their hints and discussions have contributed greatly to the results presented in this work.

I appreciate the help of and nice time I spend with all the members of the research groups "Theorie Stochastischer Prozesse" and "Statistische Physik und Nichtlineare Dynamik". Their work has certainly influenced mine. Special thanks go to Tobias Prager with whom I shared many little ups and downs in the course of my time in this group.

I am grateful to the Sonderforschungsbereich 555 "Komplexe Nichtlineare Prozesse". It's members have have continuously provided inspiring impulses. I enjoyed working on the same project with Valentina Beato.

Apart from the scientific supporters of this work there are also those that have privately provided continuous encouragement. Special thanks go to my family Franz-Xaver, Heidi, Katharina and Johannes Sailer. Most important for the nice time I spend here in Berlin is certainly Anna Melchers. Thanks a lot for that.

# Selbständigkeitserklärung

Hiermit erkläre ich, die Dissertation selbständig und nur unter Verwendung der angegebenen Hilfen und Hilfsmittel angefertigt zu haben.